



# Co(II) single-ion magnets: synthesis, structure, and magnetic properties

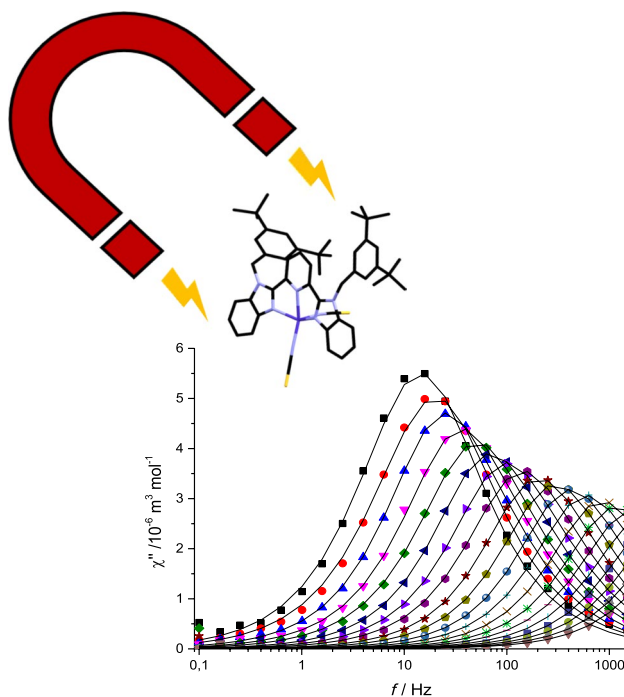
Jana Juráková<sup>1</sup> · Ivan Šalitroš<sup>1,2,3</sup>

Received: 31 December 2021 / Accepted: 25 April 2022 / Published online: 21 May 2022  
© Springer-Verlag GmbH Austria, part of Springer Nature 2022

## Abstract

Magnetoactive coordination compounds exhibiting bi- or multistability between two or more magnetic stable states present an attractive example of molecular switches. Currently, the research is focused on molecular nanomagnets, especially single molecule magnets (SMMs), which are molecules, where the slow relaxation of the magnetization based on the purely molecular origin is observed. Contrary to ferromagnets, the magnetic bistability of SMMs does not require intermolecular interactions, which makes them particularly interesting in terms of application potential, especially in the high-density storage of data. This paper aims to introduce the readers into a basic understanding of SMM behaviour, and furthermore, it provides an overview of the attractive Co(II) SMMs with emphasis on the relation between structural features, magnetic anisotropy, and slow relaxation of magnetization in tetra-, penta-, and hexacoordinate complexes.

## Graphical abstract



**Keywords** Coordination chemistry · Molecular magnets · Magnetic properties · Coordination geometry

✉ Jana Juráková  
jana.jurakova@ceitec.vutbr.cz

Extended author information available on the last page of the article

## Introduction

Since their discovery in 1993 [1], the single molecule magnets (SMMs) have attracted considerable interest due to the possibility to store the magnetization within a single molecule, which means that new materials based on these compounds have high potential in modern applications and technologies. Especially data storage devices with extraordinary high capacity, optical imaging devices, or qubits for quantum computing are the examples worth mentioning [2]. When molecules of SMMs contain only one metal centre with significant magnetic anisotropy, they are called single-ion-magnets (SIMs).

One of the conditions required for storing information in a particle is the existence of magnetic hysteresis. The SMMs display field-induced hysteresis loop in  $M$  vs. field sweeps below the blocking temperature  $T_B$ . The remnant magnetization exists for a limited period called relaxation time  $\tau$ . The blocking temperature of most molecule-based magnets is below 10 K, although cases up to 80 K can be found rarely [3–5]. To be considered decent SMMs, the compounds should show a large effective energy barrier against magnetization switch  $U_{\text{eff}}$ , the significant value of  $\tau$  and high  $T_B$ . Therefore, the goal of current research in this field is to increase  $U_{\text{eff}}$  and  $T_B$  as much as possible [6, 7]. In other words, it is a great challenge for scientists to prepare nanomagnets that exhibit slow relaxation of the magnetization (SRM) at room temperature. The value of  $U_{\text{eff}}$  is connected to the values of magnetic anisotropy parameter  $D$  and total spin number  $S$  [vide infra, see Eqs. (7) and (8)]. If the value of the energy barrier of SMMs raises, both values  $D$  and  $S$  are increased, too. Hence, the first studies were focused on lifting the value of the total spin of the molecule and the synthesis efforts were concentrated on using a large amount of connected magnetic centres, where the  $3d$  block elements were used heavily. However, recent investigations found that since  $D$  and  $S$  correlate to each other, it may be better to focus on boosting  $D$  value instead of the size of the  $S$ . This alternative approach considers Co(II) and lanthanide complexes as attractive candidates for further research [8]. In recent years, lanthanide based SMMs (Ln-SMMs) have become the most eye-catching and high-performance SMMs, although most of them are facing problems with air and moisture instability and their practical magnetic characterization becomes increasingly challenging [9].

## Single molecule magnetism—a theoretical background

There are two characteristic indications that a molecule of SMM complex exhibits the SRM:

1. detection of maxima in the  $\chi''$  vs.  $f$  dependency ( $\chi''$  is out-of-phase AC (alternating current) magnetic susceptibility);
2. presence of a hysteresis loop in the magnetization vs. applied magnetic field response [10].

Unlike the case of the compounds with long-range magnetic ordering (ferromagnets, ferrimagnets), the maximum of out-of-phase AC susceptibility  $\chi''$  shifts to higher frequencies upon the temperature increase. This behaviour shows a typical feature of SMMs, where the maxima of  $\chi''$  are both frequency and temperature dependent and the relaxation time  $\tau$  is shorter at higher temperatures. Furthermore, the hysteresis loop of SMMs is not smooth, and it rather exhibits steps characteristic of quantum tunnelling of magnetization (QTM), which correspond to positions of increased magnetization relaxation rates.

The alternating magnetic field is described by the following equation:

$$H(t) = H_{\text{DC}} + H_{\text{AC}} \cdot \cos(\omega t), \quad (1)$$

where  $H_{\text{DC}}$  is a constant of DC (direct current) magnetic field, which is parallel to oscillating field  $H_{\text{AC}}$  and it can adopt zero as well as non-zero values.  $H_{\text{AC}}$  is defined as amplitude of AC magnetic field and  $\omega$  goes for an angular frequency. The AC susceptibility measurements are used to analyse the dynamic susceptibility of sample by applying an oscillating magnetic field. For next calculations, the value of  $H_{\text{DC}}$  is set to zero. Because the alignment of magnetic moments of substance takes some time, the magnetization of the sample is not able to follow the applied external AC field. Therefore, the magnetization of the sample is delayed in comparison to magnetic field and the phase shifts by an angle  $\varphi$  [11] and Eq. (2) is valid.

$$M(t) = M_{\text{AC}} \cdot \cos(\omega t - \varphi). \quad (2)$$

Equation (2) can be rewritten using the cosine addition formula into Eq. (3).

$$M(t) = M_{\text{AC}} [\cos(\varphi) \cdot \cos(\omega t) + \sin(\varphi) \cdot \sin(\omega t)]. \quad (3)$$

The dynamic susceptibility is a complex quantity, hence it is expressed by the real  $\chi'$  (dispersion) and imaginary  $\chi''$  (absorption) components, which are dependent on the angular frequency of the AC field  $\omega$  [11, 12]:

$$\chi = \chi' + i\chi'' = \frac{M_{\text{AC}}}{H_{\text{AC}}} \cos(\varphi) + i \frac{M_{\text{AC}}}{H_{\text{AC}}} \sin(\varphi). \quad (4)$$

Therefore, the time-dependent magnetization can be rewritten as follows:

$$M(t) = H_{\text{AC}} [\chi' \cos(\omega t) + \chi'' \sin(\omega t)]. \quad (5)$$

In the case of SMMs, the AC susceptibility contains the in-phase ( $\chi'$ ) as well as the out-of-phase ( $\chi''$ ) components. They are measured as a function of the AC frequency and as a function of temperature, leading to  $\chi'$  and  $\chi''$  vs.  $f$  and  $\chi'$  and  $\chi''$  vs.  $T$  plots, respectively (Fig. 1).

The relaxation time can be determined by Eq. (6), which is valid at the peak maxima (out-of-phase component) or the inflexion point (in-phase component) in the frequency dependence of the AC susceptibility [2]:

$$\omega = \tau^{-1}. \quad (6)$$

In the presence of a large applied magnetic field, the  $m_s = -S$  state is stabilized more in comparison to  $m_s = +S$  state, which means that the spins of every molecule are aligned with the applied field and all of the molecules are in the  $m_s = -S$  state and the magnetization is saturated. After the field is switched off, the magnetization  $M$  is fixed because of the existence of the barrier and the return to the equilibrium value is happening very slowly. Therefore, a remanent magnetization is present. When the field reaches negative values, it causes the reduction of the barrier; hence it allows spins to “unfreeze” and the reversal of the magnetization is fast. Thus, a hysteresis loop is detected. The width of the hysteresis loop depends on the sweeping rate of the magnetic field as well as on the temperature. The value of magnetization projection can be positive as well as negative at zero field, which depends on the sample history and it is the principle of information storage in one single molecule [14].

Magnetic anisotropy means the preferential alignment of the magnetic axis along a specific direction. The phenomenon called zero-field splitting (ZFS) causes a single-ion anisotropy; therefore, it is essential for SMMs. It can occur in a system with  $S \geq 1$  ground state. Although it is known that the degeneracy of the  $m_s$  levels can be removed by the external magnetic field, ZFS means that the degeneracy in axial crystal field is removed even before the application of the magnetic field, the  $m_s = \pm 3/2$  levels by  $2D$  (where  $D$  is the axial ZFS parameter). Therefore, ZFS means that levels are separated in the absence of an applied magnetic field. Both the central atom and its coordination environment determine the size of the  $D$  parameter [14, 15]. In the systems with negative  $D$  (Fig. 2a), the  $m_s = \pm S$  levels have the lowest energy (double well case). They are characterised by magnetic anisotropy along the easy axis, which means that flipping the molecule's spin along the  $z$ -axis takes some energy to reorient the spin via perpendicular  $m_s = 0$  state [14]. The case of positive  $D$  (Fig. 2b) is called easy plane anisotropy and the relaxation of a system occurs fast from the  $m_s = -S$  state to the minimum value of spin projection. There are several methods to determine  $D$  and  $S$ , from which the most used ones are magnetic investigations at static

( $B_{DC}$ ) magnetic field, EPR and far-infrared magnetic spectroscopy (FIRMS).

In an applied external field parallel to the  $z$ -axis, the projection of magnetization, which is antiparallel to the field correlates with the levels of positive  $M_s$  and vice versa. The potential energy barrier value is proportional to axial ZFS parameter  $D$  and to the square of the ground state spin number according to Eqs. (7) and (8) for Kramers (non-integer spin number) and non-Kramers systems (even number of unpaired electrons), respectively:

$$U_{\text{eff}} = |D| \cdot S^2, \quad (7)$$

$$U_{\text{eff}} = |D| \cdot (S^2 - 1/4). \quad (8)$$

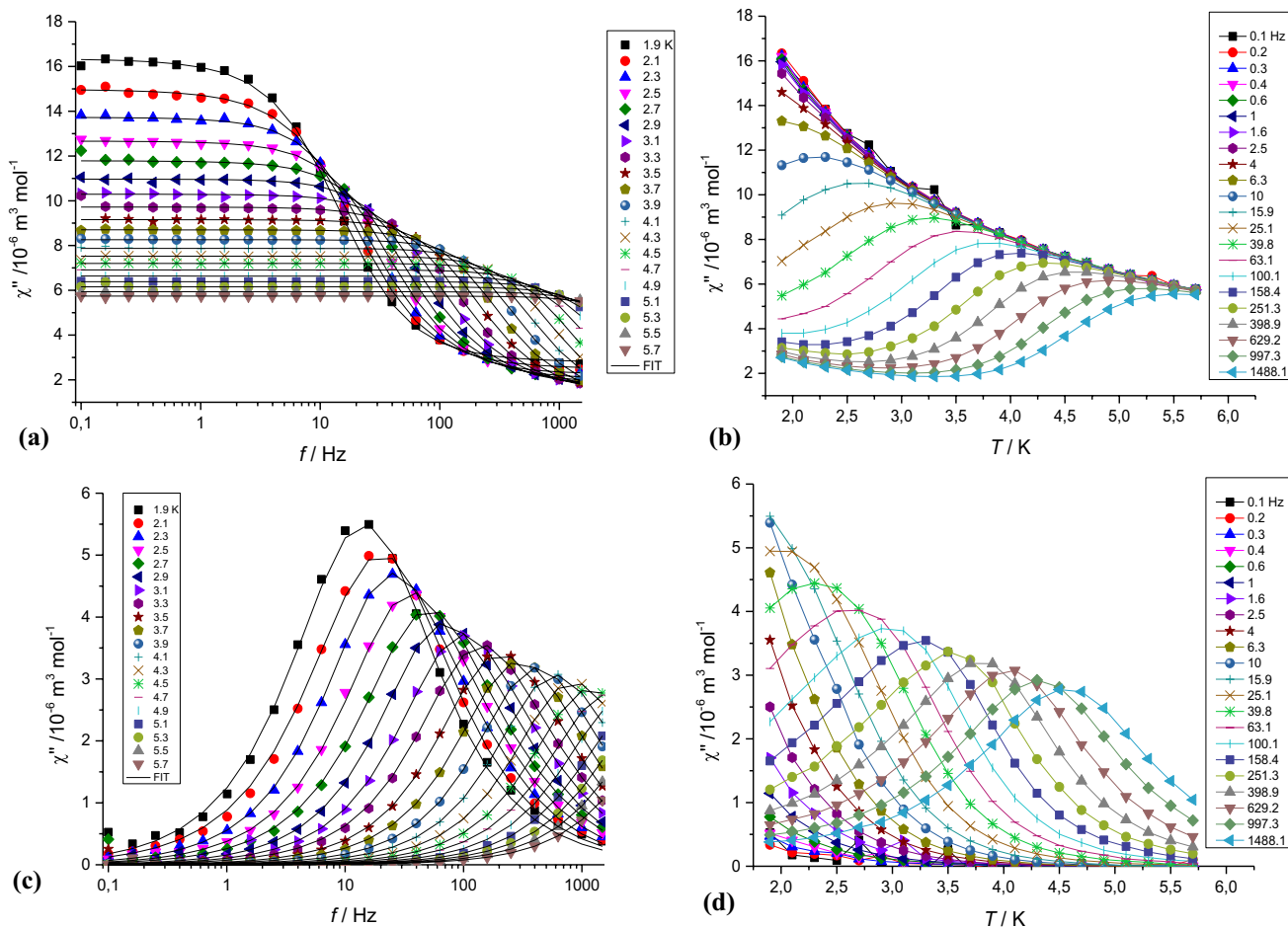
Apart from the  $U_{\text{eff}}$ , another parameter, magnetic blocking temperature  $T_B$ , characterises the SMM complex.  $T_B$  is a specific temperature, below that the magnetic moments are frozen and above it, the spin reversal can go via thermally activated processes. Although three ways can define the  $T_B$  (vide infra), the second definition is often used, but it must be taken into consideration that the value of  $T_B$  highly depends on the sweep rate of the magnetic field [12]. The possible definitions of  $T_B$  are:

- temperature, at which a peak is identified in the out-of-phase susceptibility at a given frequency;
- the highest temperature, at which hysteresis curve is detected in a field vs. magnetization dependence;
- the highest temperature, at which a maximum in the zero-field cooled magnetization is recognized [12].

Although more processes of relaxation have been proposed, there are several most studied ones via which the system can return from the state of saturation of magnetization to equilibrium state, each of them has a characteristic temperature and DC field ( $H$ ) dependence:

- Quantum Tunnelling of Magnetization (QTM);
- Thermally assisted QTM;
- Orbach process;
- Raman process;
- Direct process.

The QTM causes that the hysteresis loop of typical SMM is not smooth and some steps are noticed, while increasing the relaxation rate is observed. The origin of QTM has been investigated thoroughly to gain the ability to suppress it or use it to improve the quality of the SMMs. The quantum tunnelling can be observed between two levels of the same energy [14]. The presence of a small DC external magnetic field can remove the degeneracy of levels with opposite polarization of the magnetization, and hence, it can suppress

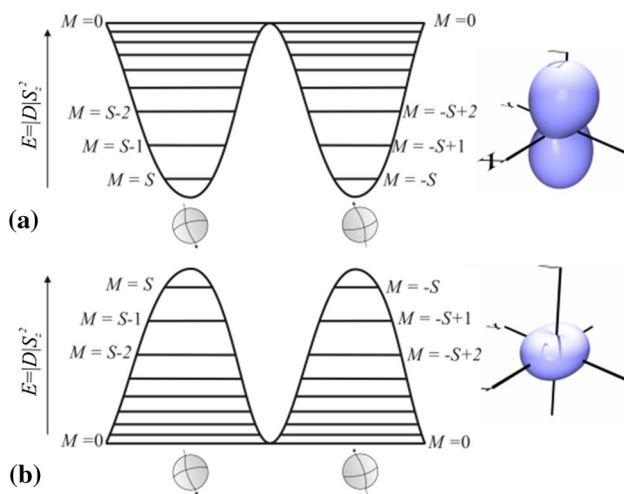


**Fig. 1**  $\chi'$  and  $\chi''$  vs.  $f$  (**a** and **c**, respectively) and  $\chi'$  and  $\chi''$  vs.  $T$  (**b** and **d**, respectively) plots for Co(II) SMM [13]

the quantum tunnelling. This is the reason why the dynamic magnetic properties are very often studied at the applied static magnetic field. Figure 3a displays that at zero field, the  $m$  levels on the left and right are in resonance. Application of a magnetic field lifts this degeneracy and at certain field levels on the left and right come into resonance again [6]. For molecules with non-integer ground state, the situation is more interesting because of the existence of Kramers doublets in the absence of an applied magnetic field. Therefore, the molecule is not able to tunnel from  $m_s = -S$  to  $m_s = +S$ . The rate of QTM is related to ligand field distortion, hyperfine interaction, transverse fields [14] and it is temperature independent—see Eq. (9):

$$\tau^{-1} = c_0 = \left( \frac{b_1}{1 + b_2 H^2} \right). \tag{9}$$

Tunnelling is possible to observe between the lowest energy states  $M_s = \pm S$  as well as between pairs of degenerate excited states, which is called thermally assisted QTM. After



**Fig. 2** Difference between easy axis (**a**) and easy plane (**b**) anisotropy [16]

the higher  $m_s$  states are populated via phonon absorption, the QTM may occur (Fig. 3b) [17].

Relaxation via Orbach process is described as follows: first, the molecule is able to change its state from  $m_s = -S$  to  $m_s = -S + 1$  by absorption of one quantum, correlating to the difference in energy between those states. The action can be repeated until  $m_s = 0$  is achieved. From this state the energy of spin can be lost due to phonon emission and state  $m_s = +S$  can be reached, although the system can return to  $m_s = -S$  state. The longitudinal relaxation rate for Orbach process describes Eq. (10):

$$\tau^{-1} = \tau_0^{-1} \exp(-U_{\text{eff}}/k_B T). \quad (10)$$

Raman process is process similar to Orbach in terms of understanding but unlike the Orbach process, this process consists of absorption of a phonon, which excites the molecule to a so-called virtual state. Often it is dominant over direct process for not too low temperatures and it is described by the Eq. (11). The Raman process is ion dependent, which means that the exponent  $n$  usually adopts value of 7 and 9 for non-Kramers and Kramers systems, respectively. It is worth to note, that because it depends also on the energy of the ground state, all values of 4 and larger are considered as reasonable ones [12]:

$$\tau^{-1} = CT^n = d \left( \frac{1 + eH^2}{1 + fH^2} \right) T^n. \quad (11)$$

Direct process of relaxation involves absorption of one phonon, which triggers a spin-flip (and the emission of the phonon) [18]. The frequency of the emitted or absorbed phonon is very short and limited by the phonon density of states [14]. The relaxation rate is proportional to temperature—see Eq. (12) and like Raman process, this mechanism is related to a nature of involved ions; therefore, the value of exponent  $m$  usually equals 2 and 4 for non-Kramers and Kramers system, respectively. The direct process is important mainly at very low temperatures, while the importance of Raman and Orbach processes becomes more significant at higher temperatures [18]:

$$\tau^{-1} = AH^m T. \quad (12)$$

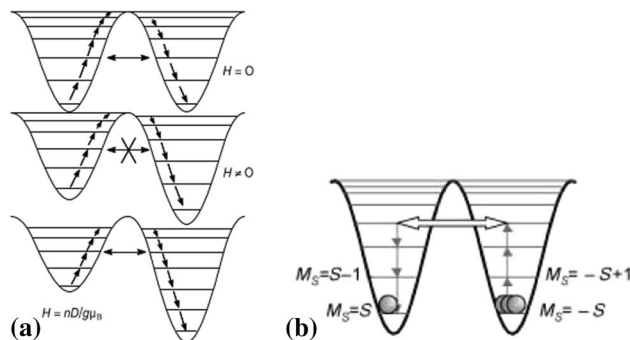
Particular knowledge of the various mechanisms is crucial for the understanding the dynamics of magnetization relaxation. Since there is usually more than one process present for one SMM, the global relaxation rate is frequently described by the Eq. (13), where a combination of these mechanisms is taken into the consideration [19]:

$$\begin{aligned} \tau^{-1} &= \tau_0^{-1} \exp\left(-\frac{U_{\text{eff}}}{k_B T}\right) + CT^n + AH^m T + c_0 \\ &= \tau_0^{-1} \exp\left(-\frac{U_{\text{eff}}}{k_B T}\right) + d \left( \frac{1 + eH^2}{1 + fH^2} \right) T^n \\ &\quad + AH^m T + \left( \frac{b_1}{1 + b_2 H^2} \right). \end{aligned} \quad (13)$$

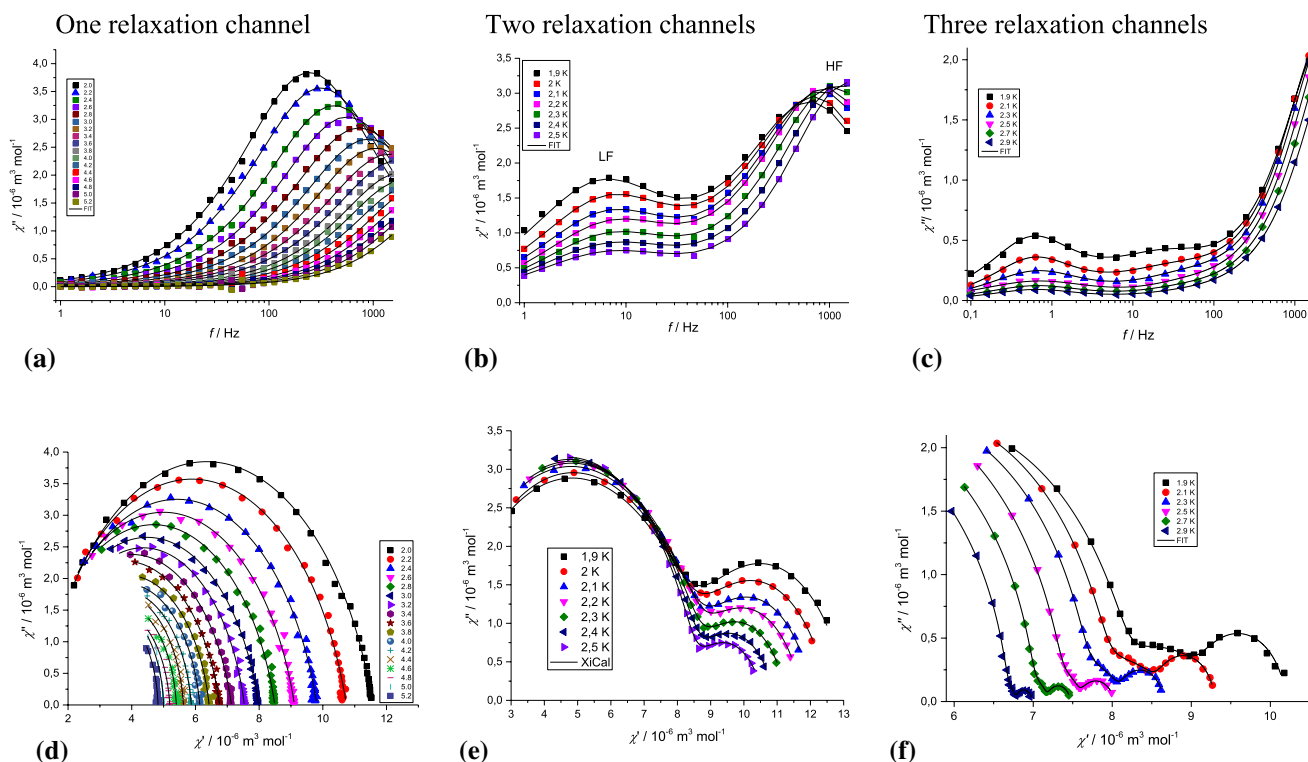
The  $a$ ,  $b_1$ ,  $b_2$ ,  $d$ ,  $e$ ,  $f$ , and  $n$  stand for reduced parameters, which are connected to the different relaxation pathways [20] and the together with the relaxation parameters  $A$ ,  $\tau_0$ ,  $U_{\text{eff}}$ ,  $C$  (vide supra) have the essential effect on the overall relaxation time  $\tau$  at the given temperature, hence the understanding of their connection with the structural characteristics of SMMs are one of the crucial challenges in the area of molecular magnetism.

When comes to the AC susceptibility measurements, from experimental point of view, the sample is installed between two coils, where the current circulates at various frequencies. The sample response after application of a tiny oscillating magnetic field, which includes a small magnetization in a substance, is detected by secondary coils. The frequency of external oscillating magnetic field varies yielding in the in-phase ( $\chi'$ ) and out-of-phase ( $\chi''$ ) AC susceptibility signals. An out-of-phase ( $\chi''$ ) peak is detected when the rate the working frequency of the AC field is nearby the flipping rate of the magnetic moment of the molecule [1]. The energy barrier  $U_{\text{eff}}$  is acquired through fitting the in-phase ( $\chi'$ ) and out-of-phase ( $\chi''$ ) AC susceptibility data using Debye model [12]. For a single relaxation process characterised by one relaxation time, the Eqs. (14) and (15), where  $\chi_S$  and  $\chi_T$  act as the adiabatic ( $\omega \rightarrow \infty$ ) and isothermal ( $\omega \rightarrow 0$ ) susceptibility, respectively [14], are valid:

$$\chi'(\omega) = \chi_s + \frac{(\chi_T - \chi_s)}{1 - \omega^2 \tau^2}, \quad (14)$$



**Fig. 3** Potential-energy diagram of an SMM and its changes as the magnetic field is swept from  $H=0$  to  $H=nD/g\mu_B$  (a). Taken with permission from Ref. [14]. Thermally assisted QTM (b). Taken with permission from Ref. [17]



**Fig. 4** Out-of-phase peaks (a–c) and the Cole–Cole plots (d–f) for one, two, and three relaxation channels at various temperatures. Solid lines present the fits [13, 21]

$$\chi''(\omega) = \frac{(\chi_T - \chi_S)\omega\tau}{1 + \omega^2\tau^2}. \quad (15)$$

Nevertheless, due to some differences across the SMM molecules, the relaxation process is usually characterised by a distribution of relaxation times. Thus, a distribution parameter  $\alpha$ , which is a measure of the distribution of relaxation processes and its value ranges from 0 to 1, is introduced. A narrow distribution of relaxation times results in a small  $\alpha$  value [12]. If there is only one peak in the  $\chi''$  vs.  $f$  plot (Fig. 4), one relaxation channel occurs and one-set Debye model (Eqs. (16) and (17)) are used to obtain fitting parameters:

$$\chi'(\omega) = \chi_s + (\chi_T - \chi_s) \frac{1 + (\omega\tau)^{(1-\alpha)} \sin\left(\frac{\pi\alpha}{2}\right)}{1 + 2(\omega\tau)^{(1-\alpha)} \sin\left(\frac{\pi\alpha}{2}\right) + (\omega\tau)^{(2-2\alpha)}}, \quad (16)$$

$$\chi''(\omega) = (\chi_T - \chi_s) \frac{(\omega\tau)^{(1-\alpha)} \cos\left(\frac{\pi\alpha}{2}\right)}{1 + 2(\omega\tau)^{(1-\alpha)} \sin\left(\frac{\pi\alpha}{2}\right) + (\omega\tau)^{(2-2\alpha)}}. \quad (17)$$

On the other hand, if two peaks of upper mentioned dependence are detected, two relaxation channels (Fig. 4) are involved and the fit of the  $\chi'$  and  $\chi''$  using two-set Debye

model leads to Eqs. (18) and (19). The in-phase ( $\chi'$ ) and out-of-phase ( $\chi''$ ) components of AC susceptibility are fitted simultaneously and  $\chi_S$ ,  $\chi_T$ ,  $\alpha_i$  and relaxation times  $\tau_i$  are obtained [12]:

$$\chi'(\omega) = \chi_S + (\chi_{T1} - \chi_S) \frac{1 + (\omega\tau_1)^{(1-\alpha_1)} \sin(\pi\alpha_1/2)}{1 + 2(\omega\tau_1)^{(1-\alpha_1)} \sin(\pi\alpha_1/2) + (\omega\tau_1)^{(2-2\alpha_1)}} + (\chi_{T2} - \chi_{T1}) \frac{1 + (\omega\tau_2)^{(1-\alpha_2)} \sin(\pi\alpha_2/2)}{1 + 2(\omega\tau_2)^{(1-\alpha_2)} \sin(\pi\alpha_2/2) + (\omega\tau_2)^{(2-2\alpha_2)}}, \quad (18)$$

$$\chi''(\omega) = (\chi_{T1} - \chi_S) \frac{(\omega\tau_1)^{(1-\alpha_1)} \cos(\pi\alpha_1/2)}{1 + 2(\omega\tau_1)^{(1-\alpha_1)} \sin(\pi\alpha_1/2) + (\omega\tau_1)^{(2-2\alpha_1)}} + (\chi_{T2} - \chi_{T1}) \frac{(\omega\tau_2)^{(1-\alpha_2)} \cos(\pi\alpha_2/2)}{1 + 2(\omega\tau_2)^{(1-\alpha_2)} \sin(\pi\alpha_2/2) + (\omega\tau_2)^{(2-2\alpha_2)}}. \quad (19)$$

The Argand (Cole–Cole) plot is commonly used for quantification of the distribution of the relaxation times width. The larger value of  $\alpha$  produces the flatter the Argand plot and if the range of  $\alpha$  is narrow and system displays only one relaxation channel, the Argand diagram is fitted combining equations of one-set Debye model very accurately.

The  $\chi''$  maximum of semicircle of one channel in the Cole–Cole plot occurs at

$$\chi' = \chi_s + \frac{1}{2(\chi_T - \chi_s)}, \quad (20)$$

and its value can be determined by Eq. (21):

$$\chi''_{\max} = \frac{1}{2(\chi_T - \chi_s) \tan\left(\frac{\pi}{4(1-\alpha)}\right)}. \quad (21)$$

## Tetracoordinate Co(II) complexes


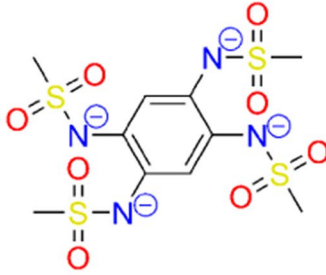
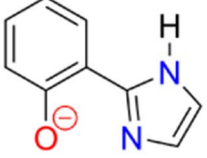

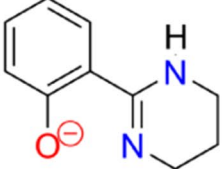
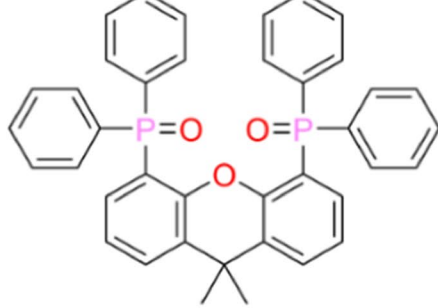
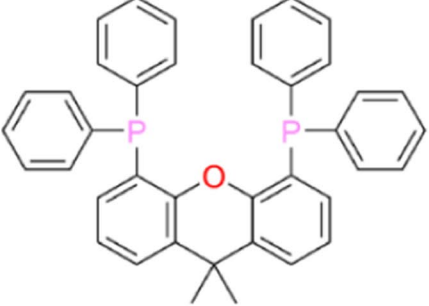
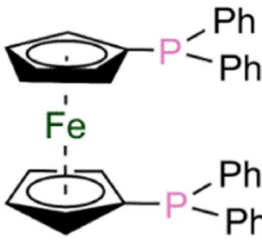
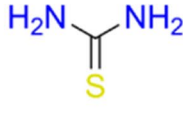
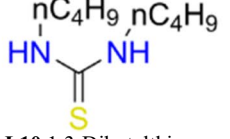
Rechkemmer et al. [22] have studied a Co(II) single-ion magnet with very high energy barrier of spin reversal and value of  $D$  parameter. The reaction of acetonitrile solutions of  $\text{Co}(\text{BF}_4)_2 \cdot 6\text{H}_2\text{O}$  and  $\text{H}_2\text{L1}$  (molecular structures of all mentioned ligands and their IUPAC names listed in Table 1) in the presence of base  $\text{NEt}_3$  resulted in formation of tetracoordinate Co(II) compound **1** ( $(\text{NHEt}_3)_2[\text{Co}(\text{L1})_2]$ ). The central ion is surrounded by four nitrogen atoms of two ligand anions  $\text{L1}^{2-}$  aligned perpendicularly to each other (Fig. 5a). The coordination geometry adopts a shape of distorted tetrahedron with the N–Co–N angles of the values  $80.59^\circ$  and  $80.70^\circ$  and the lengths of Co–N bonds acquire values from 2.00 to 2.01 Å. The variable temperature DC magnetic susceptibility data revealed the room temperature value of product function  $\chi T = 3.14 \text{ cm}^3 \text{ K mol}^{-1}$ , which is higher than the expected spin only value for a system with  $S = 3/2$ . With decreasing temperature,  $\chi T$  stays relatively constant down to 130 K, when begins to drop, suddenly reaching value near  $2.50 \text{ cm}^3 \text{ K mol}^{-1}$  at low temperatures, which is an indication of a large anisotropy (Fig. 5b). The magnetization at 1.8 K and high fields (up to 7 T) saturated to value of  $2.56 \mu_B$ , which is significantly lower than expected for this system ( $3.90 \mu_B$ ) and it also suggests the presence of pronounced ZFS. The obtained  $D$  value from fitting of the static magnetic data according to spin Hamiltonian was  $-115 \text{ cm}^{-1}$  and  $g = 2.20$ ,  $g_{\parallel} = 3.03$ , which is one of the largest published value for tetracoordinate Co(II) ion so far and it indicates a large uniaxial anisotropy of the compound **1** (all mentioned compounds, their general molecular formulas, ZFS and relaxation parameters are listed in Table 2). Investigation of the slow relaxation of magnetization was carried out via AC susceptibility measurements at several temperatures and frequencies. The compound **1** displays significant magnetic relaxation, which confirms an SMM behaviour, even in the absence of DC field (Fig. 5c). The relaxation times  $\tau$  at different temperatures obtained by fitting the Argand plots to a generalized one-set Debye model were used to construct Arrhenius plot of  $\ln \tau$  vs.  $T^{-1}$ . The linear regime observed in the high-temperature regions of the dependency refers to a temperature range, where the relaxation goes via an Orbach process. In contrast, the other—QTM, Raman and direct

processes created a curvature of the plot at the low temperatures. The fitting of the linear regime at high temperatures to the Arrhenius law gave values of  $U_{\text{eff}} = 170 \text{ K}$  and  $\tau_0 = 3.9 \times 10^{-8} \text{ s}$ , which authors reported as the highest value of effective energy barrier amongst previously reported tetra-coordinate Co(II) complexes, exhibiting SMM behaviour at the zero DC field [23–25]. Nevertheless, this value is still significantly lower as it would be obtained from calculation according to Eq. (8) with the experimental  $D$  value, obtained from static magnetic measurements. Therefore, the authors performed far-infrared transmission measurements at various static fields, and the data revealed an apparent field-dependent absorption near  $230 \text{ cm}^{-1}$  (Fig. 5d) allowed to determine the energy barrier of spin reversal  $U_{\text{eff}} = 230 \text{ K}$  experimentally. This value was fixed within the fitting procedure of Orbach and Raman processes and resulted in the best fitted values  $C = 0.09$ ,  $n = 3.65$  and  $\tau_0^{-1} = 9.1 \times 10^9 \text{ s}^{-1}$ .

Inspired by bidentate motive of  $\text{H}_2\text{L1}$ , the same research group prepared redox active tetrasulfonamido-benzene bis-bidentate bridging ligand, which allows strong exchange couplings between the neighbouring coordination centres. Albold et al. [26] have reported synthesis, structural and magnetic investigation of the dinuclear Co(II) radical-bridged compound **2** ( $(\text{K-18-c-6})_3[\{(\text{H}_2\text{L2}^{2-})\text{Co}^{\text{II}}\}_2(\mu\text{-L2}^{3-})]$ ), where  $\text{H}_4\text{L2}$  corresponds to tetrakis(methanesulfonamido)benzene. This compound is highly appealing due to pronounced hysteresis and unusually long relaxation times at low temperatures. The synthesis of mentioned coordination compound starts with the deprotonation of  $\text{H}_4\text{L2}$  with  $\text{KO}t\text{Bu}$  and following reaction with 18-crown-6 in acetonitrile. In the next, the complexation with  $\text{Co}(\text{BF}_4)_2 \cdot 6\text{H}_2\text{O}$  takes place and following oxidation with pure oxygen results in the formation of coordination polymer **2**. The single-crystal X-ray diffraction measurements displayed that compound crystallizes in the monoclinic space group  $P2_1/c$  and the supramolecular structure of the complex (Fig. 6a) contains two different couples of 18-crown-6-ethers encased potassium counterions incorporated in the crystal structure, two of them interconnect neighbouring complex anions into a polymeric chain and next two are connected to complex anions terminally. In addition, the compound contains two distorted tetrahedral coordinated Co(II) centres, surrounded by four nitrogen atoms from the ligand and one centre of inversion, which is placed at the middle of the molecule.

Authors reported complete magnetic characterization of **2**. The room temperature  $\chi T$  values of  $6.36 \text{ cm}^3 \text{ K mol}^{-1}$  is in accordance with the expected value for one Co(II) ion and one unpaired electron of radical ( $6.14 \text{ cm}^3 \text{ K mol}^{-1}$ ). The  $\chi T$  product increases gradually as the temperature is reduced to 100 K, reaching a maximum of  $7.60 \text{ cm}^3 \text{ K mol}^{-1}$ . Further cooling causes a slow downturn up to the temperature of 10 K when there is a rapid decline

**Table 1** List of reported ligands

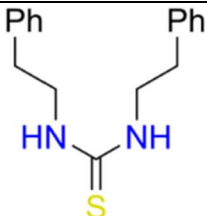
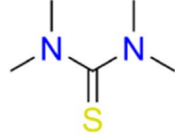
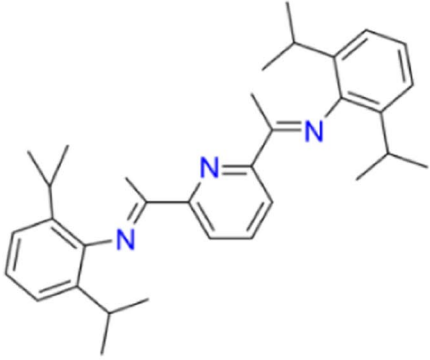
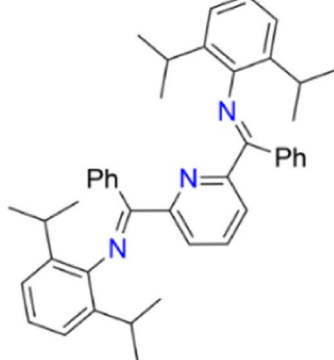
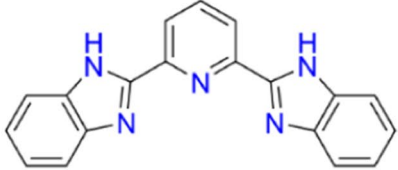
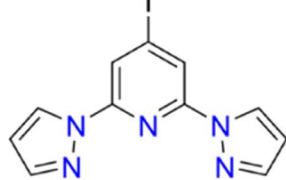
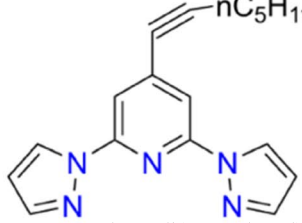
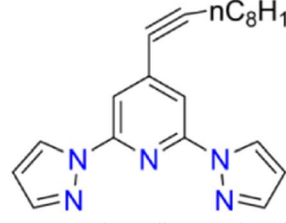
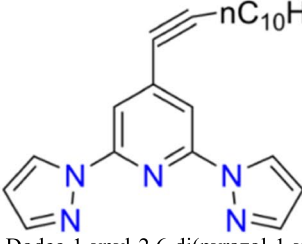
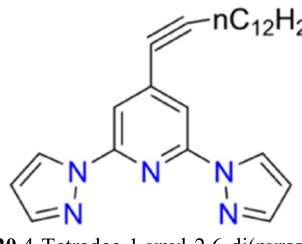
 <p><b>L1</b> Benzene-1,2-diylbis[(methylsulfonyl)azanide]</p>	 <p><b>L2</b> 1,2,4,5-Tetrakis(methanesulfonamido)benzene</p>
 <p><b>L3</b> 2-(1H-Imidazol-2-yl)phenolate</p>	 <p><b>L4</b> 2-(4,5-Dihydro-1H-imidazol-2-yl)phenolate</p>
 <p><b>L5</b> 2-(1,4,5,6-Tetrahydropyrimidin-2-yl)phenolate</p>	 <p><b>L6</b> 9,9-Dimethyl-4,5-bis(diphenylphosphinyl)xanthene</p>
 <p><b>L7</b> 9,9-Dimethyl-4,5-bis(diphenylphosphino)xanthene</p>	 <p><b>L8</b> 1,1'-Ferrocenediylbis(diphenylphosphine)</p>
 <p><b>L9</b> Thiourea</p>	 <p><b>L10</b> 1,3-Dibutylthiourea</p>

(Fig. 6b). This curve shape is explained by high magnetic anisotropy of Co(II) centres and the antiferromagnetic exchange interactions. The  $\chi T$  vs.  $T$  function was fitted according to spin Hamiltonian, which resulted in best fit values  $D = -115 \text{ cm}^{-1}$ ,  $g_{\parallel} = 2.85$  and  $g_{\perp} = 2.09$ , and they correspond to those obtained by theoretical calculations. The AC susceptibility measurements were performed on a powder sample of the complex to investigate the dynamic

magnetic behaviour. Under a zero external magnetic field, there was an apparent frequency-dependent out-of-phase signal up to 25 K (Fig. 6c). The frequency and temperature-dependent data can be reasonably fitted to the extended one-set Debye model to extract the relaxation times at different temperatures. The linear nature of the  $\ln(\tau)$  vs.  $T^{-1}$  plot at temperatures higher than 20 K displays an exponential temperature dependence of the relaxation time. The overall



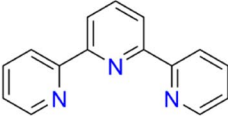
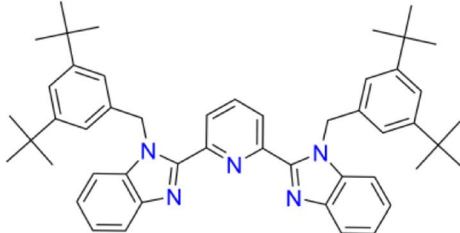
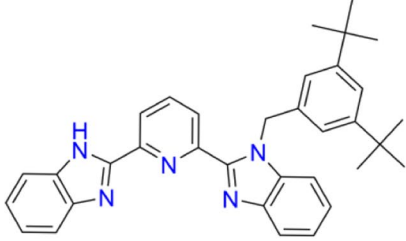
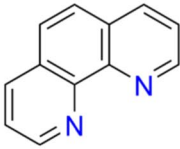
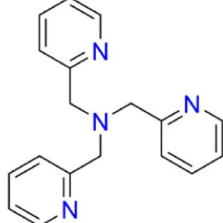
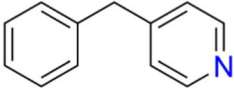
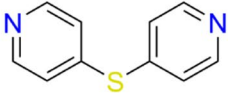
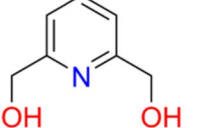
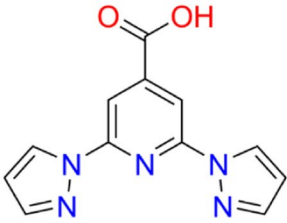
Table 1 (continued)

 <p><b>L11</b> 1,3-Bis(2-phenylethyl)thiourea</p>	 <p><b>L12</b> 1,1,3,3-Tetramethylthiourea</p>
 <p><b>L13</b> 2,6-Bis[1-[(2,6-diisopropylphenyl)imino]ethyl]pyridine</p>	 <p><b>L14</b> 2,6-Bis[1-[(2,6-diisopropylphenyl)imino]benzyl]pyridine</p>
 <p><b>L15</b> 2,6-bis(2-Benzimidazolyl)pyridine</p>	 <p><b>L16</b> 4-Iodo-2,6-di(pyrazol-1-yl)pyridine</p>
 <p><b>L17</b> 4-Hept-1-ynyl-2,6-di(pyrazol-1-yl)pyridine</p>	 <p><b>L18</b> 4-Dec-1-ynyl-2,6-di(pyrazol-1-yl)pyridine</p>
 <p><b>L19</b> 4-Dodec-1-ynyl-2,6-di(pyrazol-1-yl)pyridine</p>	 <p><b>L20</b> 4-Tetradec-1-ynyl-2,6-di(pyrazol-1-yl)pyridine</p>

non-linear nature of the  $\ln(\tau)$  vs.  $T^{-1}$  dependency (Fig. 6d) suggests that the relaxation pathway is governed not only via single Orbach process but also the Raman term must be involved in the fitting procedure, which resulted in values  $\tau_0 = 2.4 \times 10^{-10}$  s,  $U_{\text{eff}} = 267$  K,  $C = 0.9 \text{ s}^{-1} \text{ K}^{-1.20}$ , and  $n = 1.20$ . The obtained energy barrier is in perfect agreement with the value expected from the  $D$  parameter, which was found

by fitting the DC susceptibility. In addition, compound **2** exhibits an evident hysteresis at temperatures up to 15 K, which is relatively rare in Co(II) SMMs [27–30]. The hysteresis was the widest at fields between 100 Oe and 20,000 Oe, indicating that magnetisation's relaxation is slower at that region than under a zero field. Concerning this, authors also performed relaxation studies of saturated sample of **2** at

Table 1 (continued)

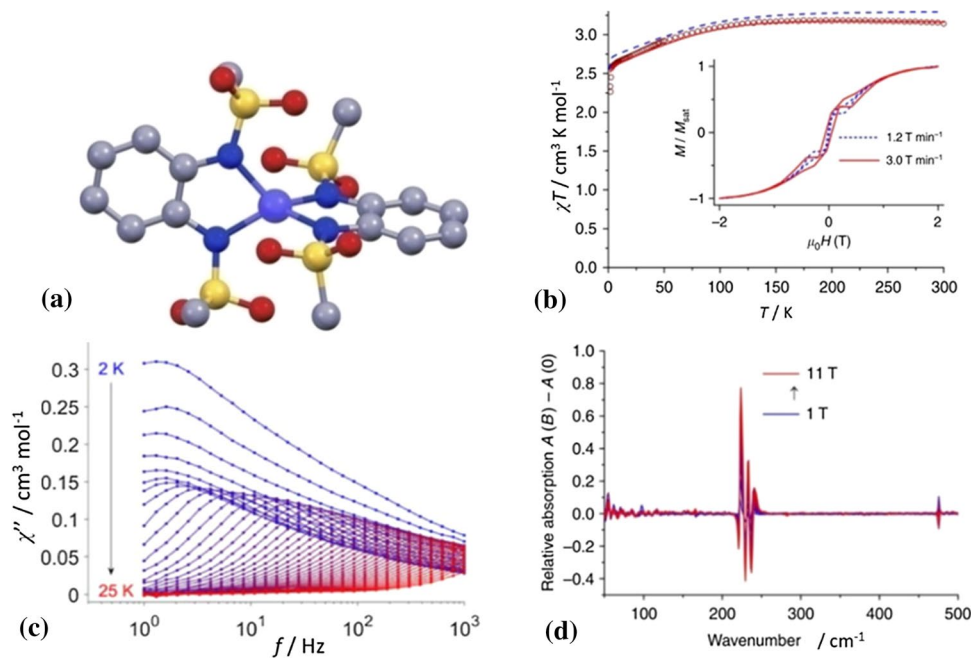
 <p><b>L21</b> 2,2':6',2''-Terpyridine (terpy)</p>	 <p><b>L22</b> 2,6-Bis(1-(3,5-di-<i>tert</i>-butylbenzyl)-1<i>H</i>-benzimidazol-2-yl)pyridine</p>
 <p><b>L23</b> 2-[6-(1<i>H</i>-Benzimidazol-2-yl)pyridin-2-yl]-1-(3,5-di-<i>tert</i>-butylbenzyl)-1<i>H</i>-benzimidazole</p>	 <p><b>L24</b> 1,10-Phenanthroline (phen)</p>
 <p><b>L25</b> Tris(2-pyridylmethyl)amine</p>	 <p><b>L26</b> 4-Benzylpyridine</p>
 <p><b>L27</b> 4,4'-Dipyridyl sulfide</p>	 <p><b>L28</b> 2,6-Dimethanolpyridine</p>
 <p><b>L29</b> 2,6-Di(1<i>H</i>-pyrazol-1-yl)pyridine-4-carboxylic acid</p>	

applied various DC fields that belong to the wider hysteresis region. At first, the compound was exposed to a high magnetic field to reach the saturation, and then the field was rapidly decreased down to desired end value from the range 500 Oe–10000 Oe and the decay of magnetization was measured in the progress of time. The data of magnetization decay fitting confirmed that the relaxation time values are growing notably with the strength of the external field. The longest relaxation time was reached at the external DC magnetic field 1500 Oe with an unusually high value of 32,000 s.

Mitsuhashi et al. [31] have studied hydrogen-bonding interactions and magnetic relaxation dynamics in tetra-coordinate Co(II) SIMs. Three tetra-coordinate Co(II)

complexes with a series of asymmetric (N and O-donor) bidentate ligands were synthesized and characterized. The authors reported that even though the static magnetic properties of the compounds are comparable, their dynamic magnetic properties are significantly different, and depend indirectly on intermolecular hydrogen-bonding interactions. The complexes **3** ([Co(**L3**)<sub>2</sub>]·CH<sub>3</sub>OH), **4** ([Co(**L4**)<sub>2</sub>]), and **5** ([Co(**L5**)<sub>2</sub>]), where **L3** = 2-(1*H*-imidazol-2-yl)phenolate, **L4** = 2-(4,5-dihydro-1*H*-imidazol-2-yl)phenolate, and **L5** = 2-(1,4,5,6-tetrahydropyrimidin-2-yl)phenolate were prepared via reaction of Co(II) salt and corresponding ligand in the 1:2 ratio in methanol (**3** and **4**) or ethanol (**5**). According to single crystal X-ray analysis, the Co(II) ion is

**Fig. 5** Molecular structure of the complex anion of **1**. Colour code: Co—blue, O—red, S—yellow, N—violet, C—grey. Hydrogen atoms have been omitted for the sake of clarity (a)  $\chi T$  vs.  $T$  plots of **1** at 1000 Oe ( $T < 50$  K) and 10,000 Oe ( $T > 40$  K). The red line = spin Hamiltonian fit ( $D = -115$  cm<sup>-1</sup>,  $g = 2.20$ ,  $g_{\parallel} = 3.03$ ). The dashed blue line = simulation according to the correlated calculations. The inset = magnetic hysteresis at  $T = 1.8$  K (b). The out-of-phase AC susceptibility at zero DC field for **1** as a function of the frequency. c Normalized far-infrared absorption spectra of **1** at  $T = 4$  K (d) [22] (colour figure online)



surrounded by two oxygen and two nitrogen atoms of bidentate ligands (Fig. 7a). The coordination geometry diverges from ideal tetrahedral geometry.

The careful investigation of supramolecular structures of **4** and **5** revealed the formation of 1D chains created by double hydrogen bonds between O and N(H) donor atoms of neighbouring complex molecules. On the other hand, the 2D network formed via hydrogen bonds of complex and methanol molecules was found in the crystal structure of **3**. The intersheet distances in the **3** (7.51 Å) are considerably shorter than those observed in the **4** and **5** (ca 9 Å), causing that each molecule of **3** is surrounded by more paramagnetic Co(II) ions in comparison with the complex molecules of **4** and **5**. Such paramagnetically rich neighbourhoods in **3** can propagate the noticeable dipolar interactions which support the QTM process. The temperature dependence of magnetic susceptibility displayed similar features for all three complexes. The values of  $\chi T$  product at temperature 300 K were near  $2.50$  cm<sup>3</sup> K mol<sup>-1</sup>, which is more than the expected value for the  $S = 3/2$  system ( $1.875$  cm<sup>3</sup> K mol<sup>-1</sup>). Nevertheless, these values are still within the conventional range for Co(II) ions with the orbital contribution. Upon lowering the temperature, the  $\chi T$  values remained constant until 70 K and then, the sudden drop was observed, which can be explained by large magnetic anisotropy of the Co(II) centre (Fig. 7b). The magnetization data do not saturate at high fields, which is an implication of the existence of ZFS. The  $g$ -factors and the axial ZFS parameters were evaluated by the simultaneous fitting of the temperature and field dependence of magnetization according to the spin Hamiltonian. The acquired parameters showed that  $D$  parameters

of all complexes are of negative value ( $-42$  cm<sup>-1</sup> for **3**,  $-38$  cm<sup>-1</sup> for **4**,  $-35$  cm<sup>-1</sup> for **5**) and the  $g_x$ ,  $g_y$  values lie in the range of 2.11–2.15, while the  $g_z$  values are near 2.50. The dynamic magnetic measurements confirmed the field induced SMM behaviour in all complexes **3**–**5**. For **3**, the temperature dependence of  $\tau$  was satisfactorily fitted with a combination of the phonon-bottleneck-limited direct and Raman processes ( $\tau^{-1} = BT^2 + CT^n$ ,  $C = 1.4 \times 10^{-3}$  s<sup>-1</sup> K<sup>-8</sup>,  $n = 8$  and  $B = 1.84$  s<sup>-1</sup> K<sup>-2</sup>). Contrarily, complexes **4** and **5** exhibited pronounced frequency dependence on both in-phase and out-of-phase susceptibilities in the presence and absence of an external DC field (Fig. 7c). This slow magnetic relaxation under the zero field is uncommon for tetrahedral Co(II) complexes; however, it is not rare, since it has been already reported for the few tetrahedral complexes [26, 32–35]. Analysis of dynamic magnetic behaviour of both complexes **4** and **5** at zero field revealed the dominant contribution of QTM mechanism to the SRM. However, this feature was suppressed by the exposure of optimal static magnetic field 400 Oe (**4**) and 800 Oe for (**5**). The temperature dependence of  $\tau$  was successfully fitted to Raman process (compound **4**,  $C = 1.2 \times 10^{-2}$  s<sup>-1</sup> K<sup>-6.6</sup>,  $n = 6.6$ ) and to combination of the Orbach and Raman processes (compound **5**,  $U_{\text{eff}} = 89$  K and  $\tau_0 = 6.4 \times 10^{-10}$  s,  $C = 6.18 \times 10^{-4}$  s<sup>-1</sup> K<sup>-6.3</sup>,  $n = 6.3$ , Fig. 7d). It is worth noting that the value of the effective energy barrier for **5** is in good agreement with expected values calculated from  $D$  parameter ( $U_{\text{eff}} = 101$  K). Since the static magnetic measurements confirmed similar magnetic anisotropy or the exchange interactions for complexes **3**–**5**, the significant differences in relaxation of magnetisation were brought the attention. Authors attributed such divergent

**Table 2** List of reported Co(II) compounds

Formula	Shape of coordination polyhedron	$D/\text{cm}^{-1}$ $E/D$ ; $E/\text{cm}^{-1}$	$U_{\text{eff}}/\text{K}$	$\tau_0/\text{s}$	Refs.
1. [Co(L1) <sub>2</sub> ](NHEt <sub>3</sub> ) <sub>2</sub>	Distorted tetrahedron	$D = -115^{\text{e}}, -112^{\text{c}}$ $E/D = 0.01^{\text{c}}$	170 331 <sup>FIRMS</sup>	$3.9 \times 10^{-8}$	[22]
2. ((K-18-c-6) <sub>3</sub> [{(H <sub>2</sub> L2 <sup>2-</sup> ) Co <sup>II</sup> ] <sub>2</sub> (μ-L2 <sup>3-</sup> )])	Distorted tetrahedron	$D = -115^{\text{e}}, -110^{\text{c}}$	267	$2.4 \times 10^{-10}$	[26]
3. [Co(L3) <sub>2</sub> ]-CH <sub>3</sub> OH	Distorted tetrahedron	$D = -42^{\text{e}}$	–	–	[31]
4. [Co(L4) <sub>2</sub> ]	Distorted tetrahedron	$D = -38^{\text{e}}$	–	–	[31]
5. [Co(L5) <sub>2</sub> ]	Distorted tetrahedron	$D = -35^{\text{e}}$	89	$6.4 \times 10^{-10}$	[31]
6. [Co(L6)(NCS) <sub>2</sub> ]	Distorted tetrahedron	$D = -7.11^{\text{e}}, -9.61^{\text{c}}$ $E = 2.23^{\text{e}}, 2.9^{\text{c}}$	31 <sup>c</sup>	–	[36]
7. [Co(L6)(NCO) <sub>2</sub> ]	Distorted tetrahedron	$D = 12.6^{\text{e}}, 13.69^{\text{c}}$ $E = 0.8^{\text{e}}, -2.99^{\text{c}}$	42 <sup>e</sup> , 39 <sup>c</sup>	$6.4 \times 10^{-11}$	[36]
8. [Co(L7)(NCS) <sub>2</sub> ]	Distorted tetrahedron	$D = -16.2^{\text{e}}, 15.9^{\text{c}}$ $E = 1.1^{\text{e}}, 1.1^{\text{c}}$	30	$6.2 \times 10^{-6}$	[37]
9. [Co(L8)Cl <sub>2</sub> ]	Distorted tetrahedron	$D = -12.0^{\text{e,HF-EPR}}, -11.0^{\text{e}} -$ $13.2^{\text{c}}, -15^{\text{c}}$ $E/D = 0.106^{\text{e,HF-EPR}}, 0.00^{\text{e}}, 0.13^{\text{c}},$ $0.116^{\text{c}}$	33	$5.2 \times 10^{-9}$	[45]
10. [Co(L8)Br <sub>2</sub> ]	Distorted tetrahedron	$D = -11.2^{\text{e,HF-EPR}}, -8.7^{\text{e}}, -$ $10.1^{\text{c}}, -12.1^{\text{c}}$ $E/D = 0.09^{\text{e,HF-EPR}}, 0.24^{\text{e}}, 0.106^{\text{c}},$ $0.102^{\text{c}}$	29	$1.8 \times 10^{-9}$	[45]
11. [Co(L9) <sub>4</sub> ](NO <sub>3</sub> ) <sub>2</sub>	Distorted tetrahedron	$D = -61.7^{\text{e}}, -62.8^{\text{c}}, -55.5^{\text{c}}$ $E/D = 0.05^{\text{c}}, 0.04^{\text{c}}$	28	$7.6 \times 10^{-7}$	[48]
12. [Co(L10) <sub>4</sub> ](ClO <sub>4</sub> ) <sub>2</sub>	Distorted tetrahedron	$D = -80.7^{\text{e}}, -84.0^{\text{c}}, -69.7^{\text{c}}$ $E/D = 0.02^{\text{c}}, 0.01^{\text{c}}$	46	$2.2 \times 10^{-6}$	[48]
13. [Co(L11) <sub>4</sub> ](ClO <sub>4</sub> ) <sub>2</sub>	Distorted tetrahedron	$D = -70.8^{\text{e}}, -63.8^{\text{c}}, -48.2^{\text{c}}$ $E/D = 0.03^{\text{c}}, 0.02^{\text{c}}$	27	$1.6 \times 10^{-6}$	[48]
14. [Co(L12) <sub>4</sub> ](ClO <sub>4</sub> ) <sub>2</sub>	Distorted tetrahedron	$D = -21.3^{\text{e}}, -21.5^{\text{c}}, -15.2^{\text{c}}$ $E/D = 0.14^{\text{c}}, 0.12^{\text{c}}$	19	$3.2 \times 10^{-8}$	[48]
15. [Co(L13)(NCS) <sub>2</sub> ]	Distorted SPY	$D = -28.1^{\text{e}}$	16	$3.6 \times 10^{-6}$	[50]
16. [Co(L14)(NCS) <sub>2</sub> ]	Distorted SPY	$D = -28.2^{\text{e}}$	24 25 (16–S)	$5.1 \times 10^{-7}$ $6.6 \times 10^{-6}$ (16–S)	[50]
17. [Co(L15)Cl <sub>2</sub> ](MeOH)	Distorted SPY	$D = 14.5^{\text{e}}, 11.09^{\text{c}}$ $E/D = 0^{\text{e}}$	20	$5.8 \times 10^{-5}$	[44]
18. [Co(L15)(NCS) <sub>2</sub> ]	Distorted TBPY	$D = 10.7^{\text{e}}, 8.44^{\text{c}}$ $E/D = 0^{\text{e}}$	10	$4.6 \times 10^{-5}$	[44]
19. [Co(L15)Br <sub>2</sub> ](MeOH)	Distorted SPY	$D = 8.4^{\text{e}}, 7.79^{\text{c}}$ $E/D = 0^{\text{e}}$	8	$3.1 \times 10^{-5}$	[44]
20. [Co(L15)Cl <sub>2</sub> ]-DMF	SPY	$D = 58.4^{\text{e}}, -87.4^{\text{c}}$ $E/D = 0.21^{\text{c}}$	33 <sup>(0.2 T)</sup> 37 <sup>(0.4 T)</sup>	$13.4 \times 10^{-8}$ <sup>(0.2 T)</sup> $4.7 \times 10^{-8}$ <sup>(0.4 T)</sup>	[54]
21. [Co(L15)Br <sub>2</sub> ]-DMF	SPY	$D = 47.0^{\text{e}}, 63.7^{\text{c}}$ $E/D = 0.24^{\text{c}}$	21 <sup>(0.2 T)</sup> 33 <sup>(0.4 T)</sup>	$5.7 \times 10^{-7}$ <sup>(0.2 T)</sup> $3.3 \times 10^{-8}$ <sup>(0.4 T)</sup>	[54]
22. [Co <sub>0.37</sub> Zn <sub>0.63</sub> (L15)Cl <sub>2</sub> ]-DMF	–	–	–	–	[54]
23. [Co(L16)Cl <sub>2</sub> ]	Distorted SPY	$D = 61.9^{\text{e}}, -61.6^{\text{c}}$ $E/D = 0.28^{\text{c}}$	31	$1.7 \times 10^{-7}$	[58]
24. [Co(L17)Cl <sub>2</sub> ]-CH <sub>3</sub> CN	Distorted SPY	$D = 153^{\text{e}}, -119^{\text{c}}$ $E/D = 0.11^{\text{c}}$	15	$1.1 \times 10^{-7}$	[58]
25. [Co(L18)Cl <sub>2</sub> ]-3CH <sub>3</sub> CN	Distorted TBPY	$D = 70.1^{\text{e}}, 44.2^{\text{c}}$ $E/D = 0.14^{\text{c}}$	–	–	[58]
26. [Co(L19)Cl <sub>2</sub> ]-2CH <sub>3</sub> CN	Distorted TBPY	$D = 46.8^{\text{e}}, 43.4^{\text{c}}$ $E/D = 0.1^{\text{c}}$	41	$6.0 \times 10^{-8}$	[58]
27. [Co(L20)Cl <sub>2</sub> ]	Distorted SPY	$D = 87.5^{\text{e}}, -58.1^{\text{c}}$ $E/D = 0.17^{\text{c}}$	–	–	[58]
28. [Co(L21)Cl <sub>2</sub> ]	Distorted SPY	–	28	$1.1 \times 10^{-6}$	[61]

**Table 2** (continued)

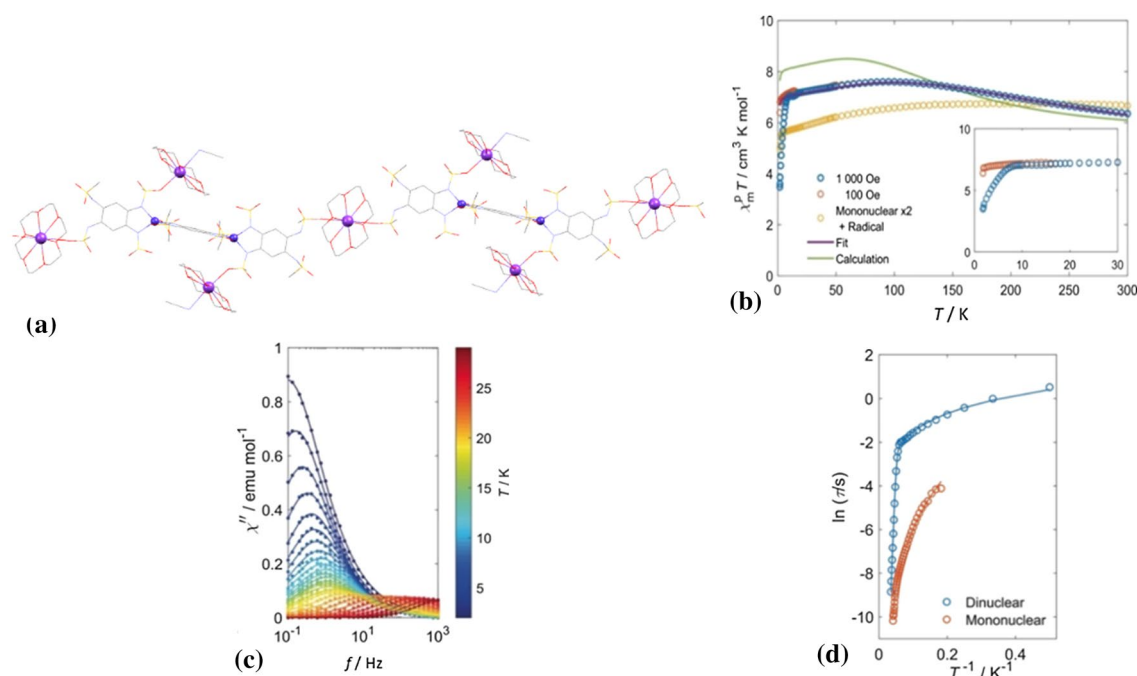
Formula	Shape of coordination polyhedron	$D/\text{cm}^{-1}$ $E/D; E/\text{cm}^{-1}$	$U_{\text{eff}}/\text{K}$	$\tau_0/\text{s}$	Refs.
29. [Co(L21)(NCS) <sub>2</sub> ]	TBPY	–	17	$5.9 \times 10^{-6}$	[61]
30. [Co(L21) <sub>2</sub> ](NCS) <sub>2</sub> ·1.5H <sub>2</sub> O	Distorted octahedron	–	–	–	[61]
31. [Co(L22)NCS <sub>2</sub> ]	Distorted SPY	$D=24.7^{\text{e}}; 30.0^{\text{c}}$ $E/D=0.333^{\text{e}}; 0.309^{\text{c}}$	25	$5.9 \times 10^{-7}$	[63]
32. [Co(L22)Cl <sub>2</sub> ]	Distorted TBPY	$D=26.0^{\text{e}}; 50.1^{\text{c}}$ $E/D=0.333^{\text{e}}; 0.125^{\text{c}}$	19	$2.9 \times 10^{-7}$	[63]
33. [Co(L22)Br <sub>2</sub> ]	Distorted TBPY	$D=39.2^{\text{e}}; 55.0^{\text{c}}$ $E/D=0.333^{\text{e}}; 0.235^{\text{c}}$	19 <sup>(0.05 T)</sup> 21 <sup>(0.3 T)</sup>	$9.2 \times 10^{-8}$ <sup>(0.05 T)</sup> $4.8 \times 10^{-6}$ <sup>(0.3 T)</sup>	[63]
34. [Co(L22) <sub>2</sub> ]Br <sub>2</sub> ·2CH <sub>3</sub> OH·H <sub>2</sub> O	Distorted octahedron	$D=64.3^{\text{c}}$ $E/D=0.12^{\text{c}}$	10	$6.7 \times 10^{-7}$	[63]
35. [Co(L24)(DMSO)Cl <sub>2</sub> ]	Distorted TBPY	$D=-17^{\text{e}}; -17.7^{\text{c}}$ $E/D=0.24^{\text{e}}; 0.313^{\text{c}}$	10	$5.7 \times 10^{-9}$	[66]
36. [Co(L25)(CH <sub>3</sub> CN) <sub>6</sub> ](BF <sub>4</sub> ) <sub>2</sub>	Distorted TBPY	$D=9.66^{\text{e}}; 8.86^{\text{c}}$ $E=0.26^{\text{e}}; 0.98^{\text{c}}$	23	$1.7 \times 10^{-8}$	[68]
37. <i>c</i> [Co(L25)Cl]Cl	Distorted TBPY	$D=-8.49^{\text{e}}; -8.63^{\text{c}}$ $E=0.0^{\text{e}}; 0.0^{\text{c}}$	23 <sup>(0.04 T)</sup>	$3.0 \times 10^{-8}$ <sup>(0.04 T)</sup>	[68]
38. <i>c</i> [Co(L25)Br]Br	Distorted TBPY	$D=-7.18^{\text{e}}; -5.3^{\text{c}}$ $E=0.0^{\text{e}}; 0.0^{\text{c}}$	17	$8.1 \times 10^{-8}$	[68]
39. [Co(L25)I]I	Distorted TBPY	$D=-7.53^{\text{e}}; -2.97^{\text{c}}$ $E=1.00^{\text{e}}; 0.66^{\text{c}}$	–	–	[68]
40. [Co(L26) <sub>4</sub> Cl <sub>2</sub> ]	Distorted TBPY	$D=106^{\text{e}}; 88.6^{\text{c}}$	–	–	[71]
41. [Co(L26) <sub>4</sub> (NCS) <sub>2</sub> ]	Distorted TBPY	$D=90.5^{\text{e}}; 88.6^{\text{c}}$	23 <sup>(0.2 T)</sup> 28 <sup>(0.4 T)</sup>	$1.2 \times 10^{-6}$ <sup>(0.2 T)</sup> $0.3 \times 10^{-5}$ <sup>(0.4 T)</sup>	[71]
42. [Co(L27) <sub>2</sub> Cl <sub>2</sub> ] <sub>n</sub>	Distorted octahedron	$D=27.2^{\text{e}}$	16.5	$2.4 \times 10^{-5}$	[73]
43. [Co(L27) <sub>2</sub> Br <sub>2</sub> ] <sub>n</sub>	Distorted octahedron	$D=28.0^{\text{e}}$	42	$7.4 \times 10^{-7}$	[73]
44. [Co(L27) <sub>2</sub> (H <sub>2</sub> O) <sub>2</sub> (H <sub>2</sub> O) <sub>4</sub> ] <sub>n</sub>	Distorted octahedron	$D=9.5^{\text{e}}$	36	$5.5 \times 10^{-7}$	[73]
45. [Co(L28) <sub>2</sub> ](mdnbz) <sub>2</sub>	Distorted square bipyramid	$D=50^{\text{e}}; -69^{\text{c}}$ $E/D=0.2^{\text{e}}; 0.19^{\text{c}}$	–	–	[74]
46. [Co(L28) <sub>2</sub> ](dnbz) <sub>2</sub>	Distorted square bipyramid	$D=44^{\text{e}}; -94.8^{\text{c}}$ $E/D=0.56^{\text{e}}; 0.12^{\text{c}}$	44	$2.8 \times 10^{-9}$	[75]
47. [Co(L29) <sub>2</sub> ](ClO <sub>4</sub> ) <sub>2</sub> ·2Me <sub>2</sub> CO	Distorted octahedron	$D=51.6^{\text{e}}$ $E/D=0.28^{\text{e}}$	16	$2.7 \times 10^{-6}$	[76]

*e* experimental values, *c* calculated values

dynamic magnetic properties at zero and non-zero static magnetic fields to the different intermolecular interactions forming the above mentioned 1D and 2D hydrogen bonded networks. Such different supramolecular architecture has a strong influence on the mechanisms of the SRM in structurally similar SIMs **3–5**.

Yang et al. [36] have studied the field induced slow magnetic relaxation behaviour in the phosphine oxide ligand-based tetrahedral Co(II) complexes modified by terminal ligands. The authors synthesized two isostructural mononuclear Co(II) complexes **6** and **7** of the formula [Co(L6)(NCS)<sub>2</sub>] and [Co(L6)(NCO)<sub>2</sub>], respectively, where **L6** = 9,9-dimethyl-4,5-bis(diphenylphosphinyl)xanthene. The number of tetrahedral Co(II) SMMs based on ligand **L6** or similar phosphine ligands have been already reported [37, 38], although this kind of ligands is more commonly used in the field of lanthanide luminescence complexes [39–41].

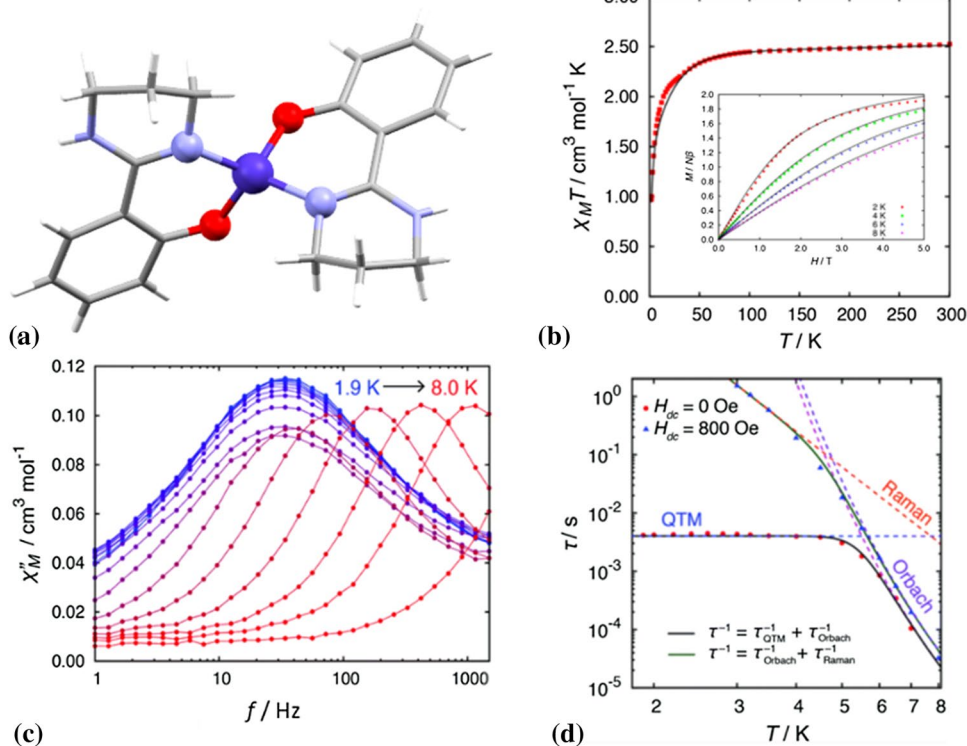
Complexes **6** and **7** were prepared by the complexation of ligand **L6** with Co(ClO<sub>4</sub>)<sub>2</sub>·6H<sub>2</sub>O and KNCS or KNCO, respectively, in a mixture of acetonitrile and THF (1:2). Both complexes contain distorted tetrahedral coordination environments, where the central ion is coordinated by two oxygen atoms of bidentate ligand **L6** and two nitrogen atoms from terminal NCS<sup>–</sup> or NCO<sup>–</sup> ligands (Fig. 8a). In addition, no significant intermolecular H-bonds and  $\pi$ – $\pi$  interactions were found in the crystal structures of complexes. The DC magnetic measurements were performed and the temperature dependence of magnetic susceptibility under an external magnetic field of 0.1 T showed the room temperature  $\chi T$  values of 2.62 and 2.75 cm<sup>3</sup> K mol<sup>–1</sup> for **6** and **7**, respectively. These values are considered to be larger than the spin-only values for a high-spin Co(II) ion with  $S=3/2$  and  $g=2$ , which can be explained by the notable spin-orbit coupling of the tetrahedral Co(II) centres. The curve



**Fig. 6** Scheme of **2** (a).  $\chi T$  vs.  $T$  plot for **2** in an applied field of 1000 Oe (blue), red line—the fit, green line—the ab initio calculation of susceptibility, yellow symbols—twice the  $\chi T$  value of **1** with the addition of a  $0.375 \text{ cm}^3 \text{ K mol}^{-1}$  as a contribution for the radical. The

inset—low-temperature region (b). The out-of-phase AC susceptibility for **2** as a function of frequency (c).  $\ln(1/\tau)$  vs.  $1/T$  plot for **1** (red) and **2** (blue) (d). Taken with permission from Ref. [26] (colour figure online)

**Fig. 7** Molecular structure of **5**. Colour code: Co—blue, O—red, N—violet, C—grey (a). Temperature dependence of the  $\chi T$  product for **5** in an applied DC field of 5000 Oe (red circles). The inset—field dependence of the magnetization for **5** at 2, 4, 6, and 8 K. The solid points—the experimental data, solid line—fit (b). Temperature dependence of out-of-phase AC susceptibility at 1.9–8.0 K **5** in the absence of the DC field. Lines—guide to the eye (c). Temperature dependence of the relaxation time  $\tau$  in the absence and presence of the DC field for **5**. The dashed lines—fitted lines for a single relaxation process of Raman, Orbach, and QTM. The solid black line—the sum of the relaxation processes (d). Taken with permission from Ref. [31] (colour figure online)

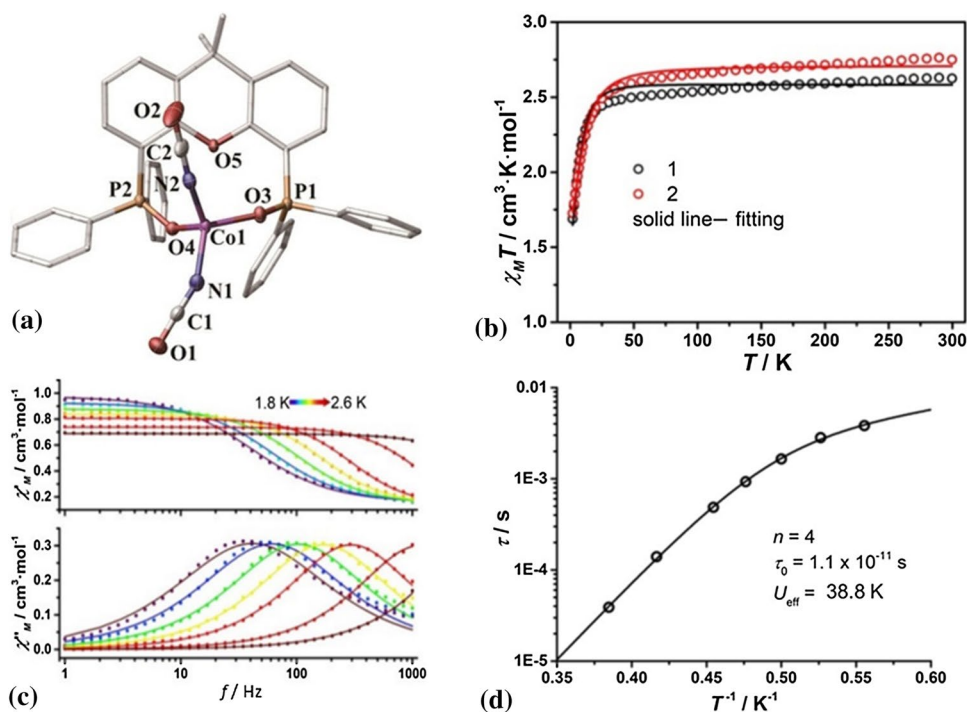


of  $\chi T$  product constantly declines upon cooling to 40 K, where is observed a sudden drop down to values of 1.69 and 1.72 cm<sup>3</sup> K mol<sup>-1</sup> for **6** and **7**, respectively (Fig. 8b). Isothermal field-dependent magnetization measurements were collected at temperatures of 2, 3, and 5 K. The magnetization does not show the saturation at high fields, the largest values of magnetization at the lowest temperature are 2.65 and 2.56  $\mu_B$  for **6** and **7**, respectively. The static magnetic data are similar for both complexes and indicate significant magnetic anisotropies. The data were fitted to spin Hamiltonian and the best fits revealed values  $g=2.29$  and  $D=-7.1$  cm<sup>-1</sup> for **6** and  $g=2.39$  for and  $D=12.6$  cm<sup>-1</sup> for **7**. Therefore, the axial magnetic anisotropy for **6** and transverse magnetic anisotropy for **7** was suggested. The calculated ab initio values of  $D$  and  $g$  are in good agreement with experimental data. Although the AC magnetic data confirmed field induced SMM behaviour in the case of both complexes (Fig. 8c), the field induced SRM displays different anisotropies for the complexes. The temperature and frequency AC susceptibility data were fitted to the modified one-set Debye model, since only one peak of the out-of-phase AC susceptibility was observed. Authors claim that relaxation features of **6** are comparable with the slow relaxation of already reported similar similar SIMs **8** [37] of the structure [Co(L7)(NCS)<sub>2</sub>] (L7 = 9,9-dimethyl-4,5-bis(diphenylphosphino)xanthene), for which were obtained ZFS parameters  $g=2.27$ ,  $D=-16.2$  cm<sup>-1</sup> and parameters of Orbach process  $U_{\text{eff}}=30$  K and  $\tau_0=6.2 \times 10^{-6}$  s. In the next, the authors report that temperature dependence of  $\tau$  of **7** can be fitted with the combination of Raman and Orbach processes with

the values of  $U_{\text{eff}}=39$  K,  $n=4$ ,  $C=24$  and  $\tau_0=1.1 \times 10^{-11}$  s (Fig. 8d). It is worth mentioning that the experimental energy barrier against the magnetization switch corresponds with the calculated value ( $U_{\text{eff}}=42$  K). The study was investigating the reason why dynamic magnetic data were so different for the structurally similar complexes **6** and **7** and the authors explained that although the complexes are isostructural, there are some minor differences present. For instance, while the Co–O and Co–N distances of **6** and **7** (1.95 Å) are similar, the angles between N–Co–O bonds differ significantly for the complexes. Therefore, the geometry of complex **7** is closer to a tetrahedral symmetry compared to **6**. As it has been already reported [24, 25, 42–44], the magnetic anisotropy of tetrahedral Co(II) complexes is highly responsive to the strength of the ligand field and, thus, the ZFS parameters can be easily modified by substituting terminal ligands. In the case of the reported work, the substitution from NCS<sup>-</sup> to NCO<sup>-</sup> changes the sign of  $D$  parameter from negative to positive. Therefore, those findings demonstrate attempts for the rational strategy to modify the magnetic anisotropies of Co(II) SIMs.

Hrubý et al. [45] were investigating Co(II) based SIMs with organometallic ligand **L8** (1,1'-ferrocenediylbis(diphenylphosphine)). The authors were focusing on the preparation, spectral and magnetic characterization of two heterobimetallic Fe(II)–Co(II) coordination compounds **9** and **10** of the formulas [Co(L8)Cl<sub>2</sub>], [Co(L8)Br<sub>2</sub>]. The complexes were synthesized by the reaction of the ferrocene ligand **L8** and corresponding Co(II) salt. Although the structure of complex **10** is new, the synthesis and structure

**Fig. 8** Structure of complex **7** with hydrogen atoms omitted for clarity (a). Temperature-dependent  $\chi T$  of **6** (black) and **7** (red) under a 1000 Oe applied DC field. Open circles = experimental data, solid lines = fit (b). Frequency-dependent in-phase and out-of-phase AC susceptibility plots for **7** under a DC field of 800 Oe. Solid lines = fit (c). Temperature-dependent relaxation time of complex **7** (solid line = fit) (d). Taken with permission from Ref. [36] (colour figure online)



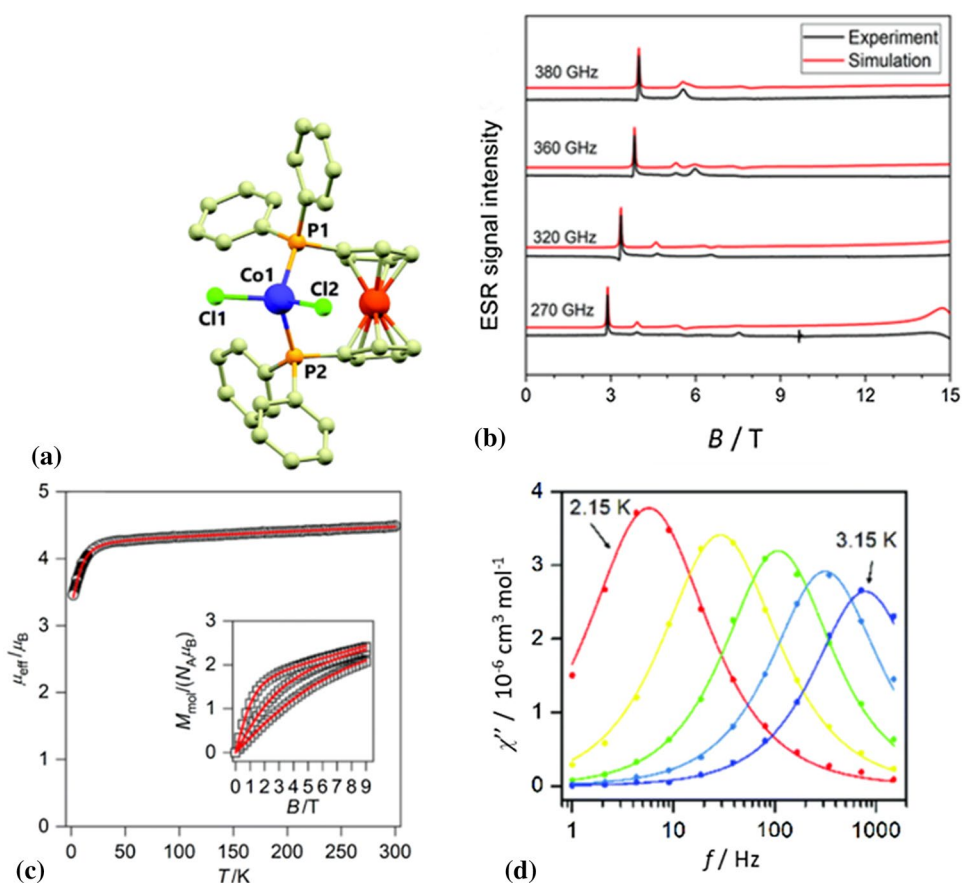
of **9** have been reported previously [46, 47]. In all three compounds, the central Co(II) ion is surrounded by two P atoms from diphenylphosphine groups of ligand **L8** and two halide terminal ligands (Fig. 9a). The compounds **9** and **10** crystallize in the triclinic space group  $P\bar{1}$  and they are both isostructural with each other with the distorted tetrahedral coordination geometry of complexes. Since both structures lack significant non-covalent interactions and the closest Co...Co distances are 9.61 and 9.68 Å in **9** and **10**, respectively, the presence of magnetic exchange coupling or the dipolar interactions are not likely present. The high-frequency electron paramagnetic resonance (HF-EPR) spectroscopy data were collected (Fig. 9b) and after the ab initio simulations procedure revealed the values of zero-field splitting parameters and  $g$ -tensor are  $D = -12.0 \text{ cm}^{-1}$ ,  $E/D = 0.10$ , and  $g_x = 2.20$ ,  $g_y = 2.20$ ,  $g_z = 2.28$  for the complex **9** and  $D = -11.2 \text{ cm}^{-1}$ ,  $E/D = 0.09$ , and  $g_x = 2.22$ ,  $g_y = 2.22$ ,  $g_z = 2.31$  for **10**. DC magnetic measurements revealed similar magnetic behaviour for both complexes **9** and **10**. At room temperature, the values of the effective magnetic moment (4.4–4.5  $\mu_B$ ) are larger than spin only value for this system (3.87  $\mu_B$ ). Upon cooling, the values remain constant until 20 K and then they exhibit a rapid drop to a minimal value of 3.5 and 3.7  $\mu_B$  for **9** and **10**, respectively. Such a sudden decrease can be explained by the large magnetic anisotropy of the Co(II) ion (Fig. 9c). The magnetic data were fitted to spin Hamiltonian, which confirmed the axial magnetic anisotropy in compounds **9** and **10**, and the values of  $D$  and  $g$  parameters were following calculated values as well as those obtained from HF-EPR measurements. Dynamic magnetic measurements revealed field-induced SMM behaviour for both complexes **9** and **10** and thus, the AC susceptibility was measured at  $B_{DC} = 0.1 \text{ T}$  (Fig. 9d). Then, the data were fitted by the one-component Debye model, because there was only one frequency-dependent peak of the out-of-phase magnetic susceptibility. The temperature dependency of relaxation times was successfully analysed with the single Orbach process in both cases with the parameters  $\tau_0 = 5.2 \times 10^{-9} \text{ s}$ ,  $U_{\text{eff}} = 33 \text{ K}$  for **9**, and  $\tau_0 = 1.8 \times 10^{-9} \text{ s}$ ,  $U_{\text{eff}} = 29 \text{ K}$  for **10**. It is worth noting that the values of  $U_{\text{eff}}$  are in very good agreement with the calculated from the HF-EPR analysis as well as with the experimental magnetic data. What is further interesting about this publication, the authors performed deposition of the **10** on surfaces, such as Au(111), glass, and acetate. This deposition is important from the technological point of view in the further development of devices based on SMMs. They used two techniques: a thermal sublimation in high-vacuum and a drop-casting under an inert nitrogen atmosphere. While they deposited the complex by drop-casting under inert nitrogen atmosphere successfully, the technique of thermal sublimation was not fully successful due to partial decomposition of the complex, which was moisture sensitive. Therefore,

the authors suggested that *the nano-structuration of these systems should be operated by introducing functional groups allowing the chemisorption from diluted solution and promoting the formation of monolayers on surfaces* [45].

Vaidya et al. [48] studied structural characterization and magnetic properties in the series of mononuclear four-coordinate thiourea Co(II) complexes. Four complexes **11** ([Co(**L9**)<sub>4</sub>](NO<sub>3</sub>)<sub>2</sub>), **12** ([Co(**L10**)<sub>4</sub>](ClO<sub>4</sub>)<sub>2</sub>), **13** ([Co(**L11**)<sub>4</sub>](ClO<sub>4</sub>)<sub>2</sub>), and **14** ([Co(**L12**)<sub>4</sub>](ClO<sub>4</sub>)<sub>2</sub>), where **L9** = thiourea, **L10** = 1,3-dibutylthiourea, **L11** = 1,3-phenylethylthiourea, and **L12** = 1,1,3,3-tetramethylthiourea, were prepared by the reaction of Co(NO<sub>3</sub>)<sub>2</sub>·6H<sub>2</sub>O or Co(ClO<sub>4</sub>)<sub>2</sub>·6H<sub>2</sub>O and corresponding ligand in ethyl acetate or alcoholic solution. Single crystal X-ray diffraction measurements revealed that complexes **11** and **14** crystallise in the monoclinic space groups  $Pc$  and  $P2_1/c$ , respectively, whereas the remaining complexes **12** and **13** crystallize in the triclinic space group  $P\bar{1}$ . Furthermore, all complexes adopt a distorted tetrahedral geometry with the central ion surrounded by four sulphur atoms of monovalent ligands (Fig. 10a), where the Co–S distances range from 2.30 to 2.31 Å for the series. DC magnetic susceptibility measurements at room temperature give values of  $\chi T = 3.10$ , 3.03, 3.08, and 2.60 cm<sup>3</sup> K mol<sup>-1</sup> for compounds **11–14**, respectively, which are clearly higher than the expected spin-only value for mononuclear Co(II) system.  $\chi T$  data for all complexes display a downturn at low temperature, suggesting the presence of significant magnetic anisotropy. The low-temperature magnetization measurements at various applied DC fields were performed at 2, 4, and 8 K, saturating to values of 2.25, 1.99, 1.95, and 2.07  $\mu_B$  for **11–14**, respectively, at the lowest temperature and high fields, which also suggest the significant ZFS (Fig. 10b). The values of  $D$  extracted from fitting of magnetic data were found to be negative in the range from  $-21.3 \text{ cm}^{-1}$  for **14** to  $-80.7 \text{ cm}^{-1}$  for **12**. Temperature- and frequency-dependent AC susceptibility data were collected to confirm SMM behaviour of all four compounds. The  $\chi''$  signal for **11–13** was observed even in the absence of an applied DC field, while **14** was proved to be a field-induced SIM. The data of **11** show two relaxations processes, a fast one is operative below 3 K and slow one in the temperature range 3.5 and 10 K (Fig. 10c). The authors attributed the fast process to QTM, whereas the slower one is identified as a thermally activated process in which the relaxation is governed via Orbach process with parameters  $U_{\text{eff}} = 28 \text{ K}$  and  $\tau_0 = 7.6 \times 10^{-7} \text{ s}$  of comparable values to already reported values for tetracoordinated Co(II) complexes [24, 25, 49]. Compound **12** also exhibits two relaxation processes at the zero DC field, although the values of an effective energy barrier and relaxation time estimated from the Arrhenius plot are larger ( $U_{\text{eff}} = 46 \text{ K}$  and  $\tau_0 = 2.2 \times 10^{-6} \text{ s}$ ). Since both compounds **11** and **12** show some intermolecular hydrogen bonding networks, which may affect the relaxation features, the



**Fig. 9** Molecular structure of **9** (a). HF-EPR spectra of **9** (b). DC magnetic data of **9** (c). AC susceptibility data for **9** (d) [45]

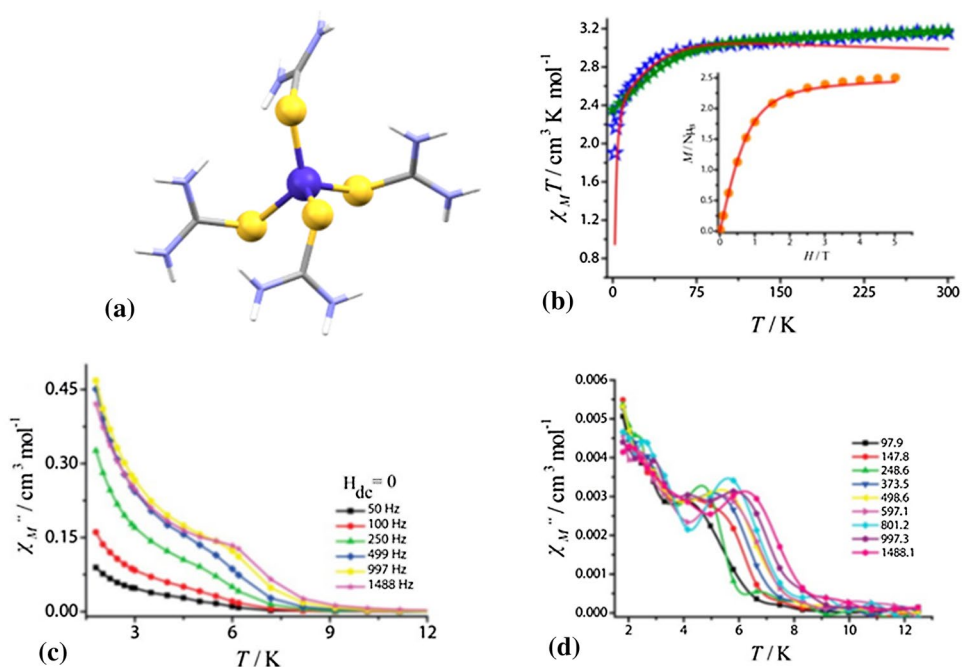


diluted samples (solid solutions of 10% Co(II) samples with 90% of the corresponding Zn(II) analogues) were prepared to suppress fast QTM and bring more light to the relaxation dynamics. In both cases, the analysis showed that intermolecular interactions effectively contribute to quenching the QTM in the absence of DC field (Fig. 10d). The peaks of the thermally activated processes were better resolved and the increase of the energy barrier values to 47 K and of 89 K for **11** and **12**, respectively, was observed. The AC data for compound **13** differ considerably from the other reported complexes and they reveal more out-of-phase susceptibility peaks in the absence of DC field, which are not resolved and this led to collecting data at 2000 Oe DC field to find more resolved peaks. After extraction from the Arrhenius plot, the effective energy barrier and the relaxation time were detected to be  $U_{\text{eff}} = 27$  K and  $\tau_0 = 1.6 \times 10^{-6}$  s. Unlike the compounds **11**–**13**, the AC measurements of **14** did not show out-of-phase susceptibility without the presence of DC field. After analysis of the AC data collected at 0.2 T field, effective energy barrier and relaxation time were found to be of the values 19 K and  $3.2 \times 10^{-8}$  s. Since there are more relaxation mechanisms, such as Raman and QTM, the experimental energy barriers are lower than theoretically expected values for all four complexes.

### Pentacoordinate and hexacoordinate Co(II) complexes

The group of Richeson [50] studied SMM behaviour enhanced through peripheral ligand modification. They used tridentate bis(imino)pyridine pincer ligands in conjunction with two isothiocyanate ligands to prepare two mononuclear Co(II) complexes. The rigid and planar pincer ligands favour a square pyramidal geometry rather than trigonal bipyramid. That would induce a larger zero-field splitting  $D$  parameter. Furthermore, the scientists introduced phenyl substituents in the imine positions expecting that this step can affect the geometry of the coordination environment by inducing of higher degree of distortion and pulling of the Co(II) ion out of the basal plane. According to authors, the  $\text{Co}(\text{NCS})_2$  reacted directly with ligands **L13** (2,6-bis[1-[(2,6-diisopropylphenyl)imino]ethyl]pyridine) or **L14** (2,6-bis[1-[(2,6-diisopropylphenyl)imino]benzyl]pyridine). Nearly quantitative yields of green compound **15** of formula  $[\text{Co}(\text{L13})(\text{NCS})_2]$  and brown–green compound **16** of formula  $[\text{Co}(\text{L14})(\text{NCS})_2]$  were prepared. The pentacoordinate Co(II) ion adopts distorted square pyramidal geometries (Fig. 11a) in both compounds. In **15**, the central atom sits above the basal plane by 0.39 Å. Introduction of phenyl substituents in **16** caused more visible distortion

**Fig. 10** Molecular structure of complex cation of **11**. Colour code: Co—blue, S—yellow, N—violet, C—grey (a). DC magnetic data for **11** (b). Frequency-dependent out-of-phase susceptibility data for **11** in the absence DC field (c). Frequency-dependent out-of-phase susceptibility data for 10% diluted sample of **11** in the absence of DC field (d). Taken with permission from Ref. [48] (colour figure online)

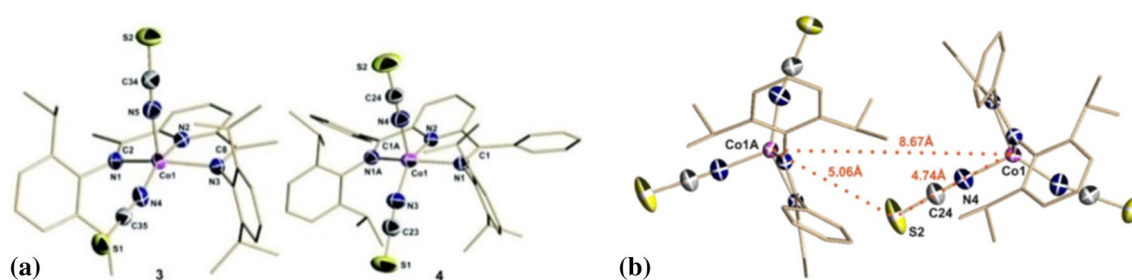


with the metal centre lying out of the basal plane by 0.52 Å. Neither of the prepared complexes shows relevant intermolecular contacts; however, compound **16** displays an interesting packing arrangement. Although Co(II) ions are separated by 8.67 Å, the S2 atom of apical isothiocyanate is oriented towards the open face of the adjacent metal centre along the *C*-axis (Fig. 11b). The methyl analogue does not show that kind of long-distance interaction, and the shortest metal–metal distances were found to be 9.90 Å.

The variable temperature DC susceptibility for both compounds was measured at a field of 1000 Oe and over the temperature range 2–300 K (Fig. 12a). According to expectations, the  $\chi T$  value remained constant up to 100 K, and then started to decrease with decreasing temperature. Such continual decrease up to 2 K was observed for **15** and is related with ZFS. However, the  $\chi T$  value of complex **16** reaches the lowest value 2.48 cm<sup>3</sup> K mol<sup>-1</sup> at 12 K, then starts to increase up to 3.21 cm<sup>3</sup> K mol<sup>-1</sup> at 3 K and again drops down to 3.03 cm<sup>3</sup> K mol<sup>-1</sup> at 2.5 K. Such magnetic behaviour is attributed to ferromagnetic exchange coupling mediated through intermolecular interactions, which can be suppressed by dilution of sample. Thus, compound **16** was dissolved in THF and further DC susceptibility measurements were performed on a frozen solution below 50 K (Fig. 12a, red dots). The **16-S** curve is in accordance with expectations, it shows a smooth decrease in  $\chi T$  with decreasing temperature reaching 2.1 cm<sup>3</sup> K mol<sup>-1</sup> at 2.5 K. The absence of increase of  $\chi T$  in the measurement of dissolved sample proves that observed behaviour in the solid state sample of **16** has origin in the intermolecular interactions between the highly anisotropic spin carriers. The

field dependence of the magnetization of **15**, **16**, and **16-S** shows no apparent saturation, which can be caused by the presence of magnetic anisotropy. Unfortunately, the authors report that several attempts to fit the reduced magnetization data were unsuccessful, and more sophisticated software needs to be employed to achieve proper fits. On the other hand, the susceptibility data can be fitted assuming a simple zero-field splitting effect [51, 52], which leads to *D* values of -28.1 cm<sup>-1</sup> for **15** and -28.2 cm<sup>-1</sup> for **16**, suggesting a considerable uniaxial anisotropy. To confirm SMM behaviour, temperature and frequency dependence of the AC susceptibility were measured in the temperature range from 2 to 10 K for both compounds. The optimum fields of 700 and 2000 Oe for **15** and **16**, respectively, were found. However, to bring more light in comparison of energy barriers of both complexes, further AC measurements were performed under the same 2000 Oe field for all samples (Fig. 12b–d). The fitting procedure according to a thermally activated Orbach process resulted in following parameters:  $U_{\text{eff}} = 16$  K,  $\tau_0 = 3.6 \times 10^{-6}$  s for **15**,  $U_{\text{eff}} = 24$  K,  $\tau_0 = 5.1 \times 10^{-7}$  s for **16**, and  $U_{\text{eff}} = 25$  K,  $\tau_0 = 6.6 \times 10^{-6}$  s for **16-S**. Similar data obtained from solid **16** and frozen solution **16-S** confirmed that SRM has a molecular origin.

The group of Konar [44] also published an article dealing with the impact of the ligand field and coordination geometry on the magnetic anisotropy of pentacoordinate Co(II) based SIMs. The idea was to tune the magnetic anisotropy and dynamics of relaxation processes by variation of terminal ligand anions around the metal centre. Complexes **17**, **18**, and **19** of formulas [Co(L15)Cl<sub>2</sub>](MeOH), [Co(L15)(NCS)<sub>2</sub>], and [Co(L15)Br<sub>2</sub>](MeOH), respectively, were

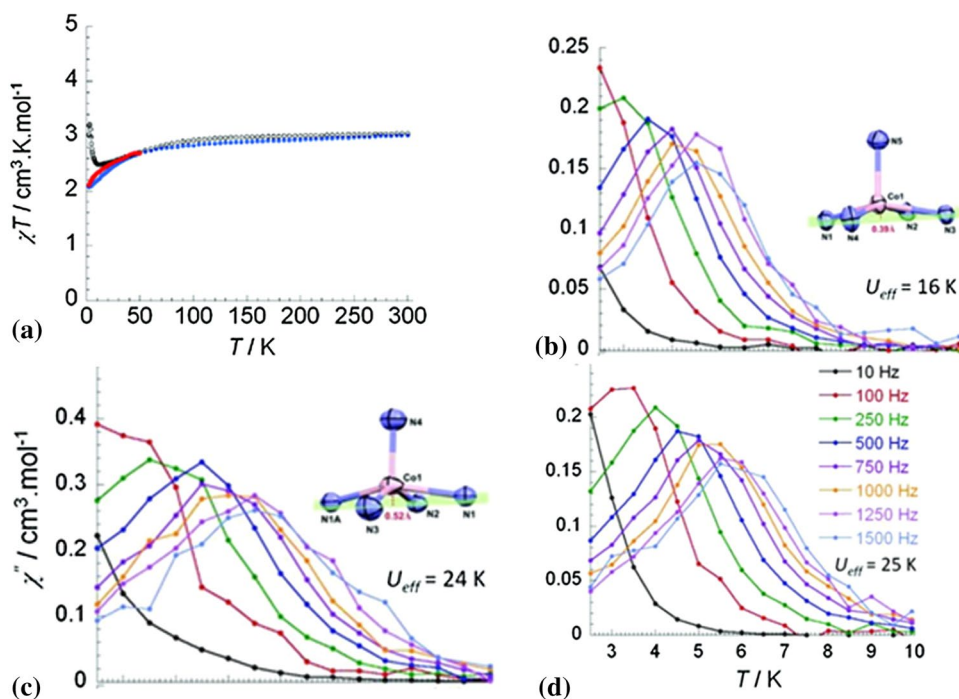


**Fig. 11** Structure and selected atom numbering scheme of compounds **15** (a—left) and **16** (b—right). Hydrogen atoms and co-crystallized solvents omitted for clarity (a). The intermolecular interactions for compound **16** (b). Taken with permission from Ref. [50] (colour figure online)

synthesized via complexation of ligand **L15** (2,6-bis(2-benzimidazol-1-yl)pyridine) with corresponding Co(II) salts and all reactions yielded green crystals after slow evaporation of the solvent. The structural analysis shows that the five-coordinate Co(II) centres adopt geometries which are best defined as distorted square pyramid for **17** and **19** and as trigonal bipyramid for **18**. Both complexes **17** and **19** are isostructural with each other, the crystal structure of **18** presents Fig. 13a. Magnetic susceptibility studies (Fig. 13b) were carried out for all complexes under a 1000 Oe field. At 300 K, the  $\chi T$  values of 2.57, 2.39, and 2.28  $\text{cm}^3 \text{K mol}^{-1}$  were observed for **17**, **18**, and **19**, respectively, which are higher than the expected spin-only value for the HS Co(II) centres. The typical values for anisotropic Co(II) complexes are in the range of 2.1–3.4  $\text{cm}^3 \text{K mol}^{-1}$  [53]. Upon the cooling, the  $\chi T$  values are stable up to 60 K, below which there is a sudden drop caused by ZFS, reaching values of 1.69, 1.52,

and 1.46  $\text{cm}^3 \text{K mol}^{-1}$ , for **17**, **18**, and **19**, respectively, at 2 K. Reduced magnetization data values are lower than the theoretical saturation for an  $S=3/2$  system and do not saturate at high fields. Density functional theory (DFT) calculations give positive  $D$  parameters (11.1  $\text{cm}^{-1}$ , 8.4  $\text{cm}^{-1}$ , and 7.8  $\text{cm}^{-1}$  for **17**, **18**, and **19**, respectively), which are matching with the experimental ones (14.5  $\text{cm}^{-1}$ , 10.7  $\text{cm}^{-1}$ , and 8.4  $\text{cm}^{-1}$  for **17**, **18**, and **19**, respectively). According to authors, those values differ from the most of to date reported SMM, where  $D$  parameter is negative. The AC susceptibility data (Fig. 13c) of all complexes revealed the SMM behaviour, although the signal was not detected at a zero DC field. The data were fitted by one-set Debye model. The effective energy barrier and relaxation times were calculated using the Arrhenius equation for thermally activated process and give  $U_{\text{eff}}$  of **17**, **18**, and **19** of 20 K, 10 K, and 8 K, respectively. The relaxation times  $\tau_0$  are on the order of  $10^{-5}$  s, which

**Fig. 12** Temperature dependence of the  $\chi T$  product at 1000 Oe for complexes **15** (blue) and **16** (black), red dots **16-S** are for a THF solution sample of **16** (a). Variable-frequency out-of-phase AC susceptibility data collected over the temperature range 2–10 K under an applied field of 2000 Oe for **15** (b), **16** (c), **16-S** (d). Taken with permission from Ref. [50] (colour figure online)



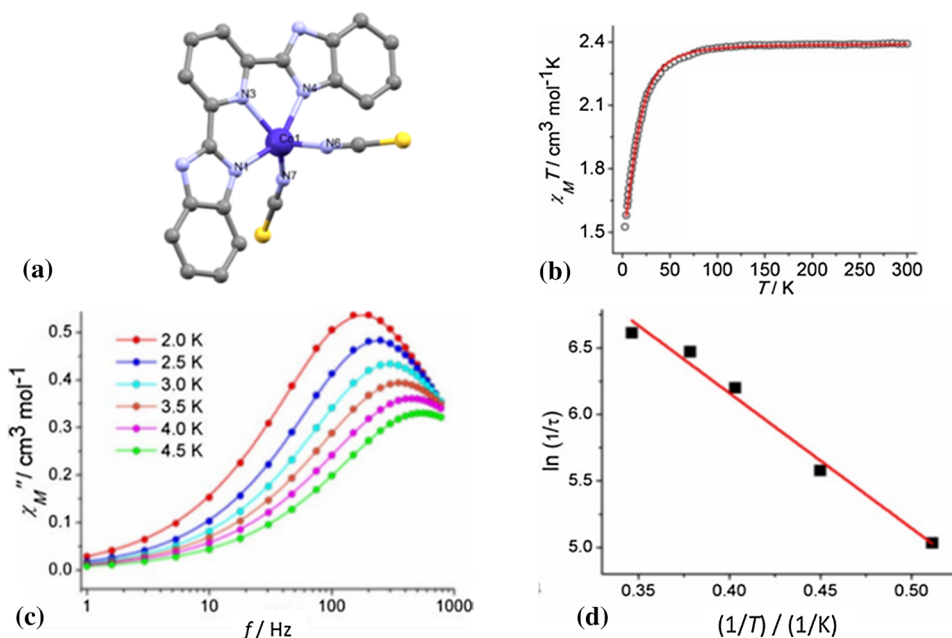
are typical for Co(II) HS complexes.  $\ln(1/\tau)$  vs.  $1/T$  plot for complex **18** as well as best fits of the Arrhenius equation is in Fig. 13d.

Similarly, the group of Boča [54] has prepared, structurally and magnetically characterized two complexes of  $[\text{Co}(\text{L15})\text{X}_2]\cdot\text{DMF}$  type. Tridentate N-donor ligand **L15** has been synthesized via reaction of pyridine-2,6-dicarboxylic acid and *o*-phenylenediamine in phosphoric acid. Reported complexes in polycrystalline form were prepared by the complexation of **L15** with corresponding anhydrous Co(II) salt in THF and the single crystals of both complexes were grown from DMF solvent. Both complexes are isostructural and isomorphous with each other and crystallize in monoclinic crystal  $P2_1/n$  space group. In the crystal structures, the  $\pi$ - $\pi$  stacking with centroid distances ca. 3.6 Å between the pyridine rings can be found. The  $\tau_5$  parameter equals 0.02, which means that the coordination chromophore adopts shape close to square pyramid. The molecular structure of  $[\text{Co}(\text{L15})\text{Cl}_2]\cdot\text{DMF}$  (**20**) is shown on Fig. 14. Although the structure and static magnetic properties of **20** were already reported before [55, 56], the authors measured it again for the sake of better comparison with the data of **21**. Two effects are visible in the temperature dependency of  $\mu_{\text{eff}}$  for complex **21**. Upon the cooling from room temperature,  $\mu_{\text{eff}}$  slightly decreases due to the presence of temperature-independent paramagnetism. Such decrease becomes more pronounced in the low temperature region (< 50 K), where the ZFS effect becomes visible. The field-dependent magnetization was measured at constant temperature of 2.0 and 4.6 K, respectively. The magnetization per formula unit at  $T=2.0$  K and high fields saturates to the value of  $2.26 \mu_{\text{B}}$ . This is lower than expected value of  $3 \mu_{\text{B}}$  which can be addressed again

to zero-field-splitting. The values of calculated  $D$  parameter by ZFS fitting model are  $58.4 \text{ cm}^{-1}$  and  $+47.0 \text{ cm}^{-1}$  for **20** and **21**, respectively.

Interesting findings concerning the SRM of **20** were reported. Since the highest response of out-of-phase component  $\chi''$  of AC susceptibility varies with the applied static magnetic field, the frequency- and temperature-dependent AC susceptibility measurement was investigated at two different static fields – 2000 and 4000 Oe (Fig. 15). Furthermore, the  $\chi''$  component of AC susceptibility as function of frequency displays two maxima, which means that magnetization relaxes via two low-frequency (LF) and high-frequency (HF) relaxation channels. Therefore, dynamic magnetic data were analysed using two-set Debye model, which allowed to evaluate two different relaxation times  $\tau(\text{LF})$  and  $\tau(\text{HF})$ . The observed two relaxation processes behave differently while increasing temperature. Although the faster HF branch of relaxation time diminishes with temperature, the  $\tau(\text{LF})$  of slower LF channel retains almost constant with the temperature. To bring more light into the relaxation processes, the doped complex **22** ( $[\text{Co}_{0.37}\text{Zn}_{0.63}(\text{L15})\text{Cl}_2]\cdot\text{DMF}$ ) containing the solid solution of **20** with Zn(II) diamagnetic analogue has been prepared. Such dilution with diamagnetic matrix causes the isolation of Co(II) complex molecules from each other and it abrogates the intermolecular interactions between the paramagnetic centers in that way. Surprisingly, the appearance of the LF relaxation channel in **22** was significantly suppressed which proves that its origin is conditioned by the intermolecular interactions and it does not have a molecular origin. Authors reported that both studied complexes **20** and **21** exhibit field-supported single-molecule magnet behaviour with values of effective barrier  $U_{\text{eff}}$  around

**Fig. 13** Molecular structure of complex **18** (a)  $\chi T$  vs.  $T$  plots measured at 1000 Oe for **18** (b). The out-of-phase AC susceptibility for **18** as a function of the frequency (c).  $\ln(1/\tau)$  vs.  $1/T$  plot for complex **18**. The red line is the best fit of the Arrhenius relationship (d). Taken with permission from Ref. [44] (colour figure online)



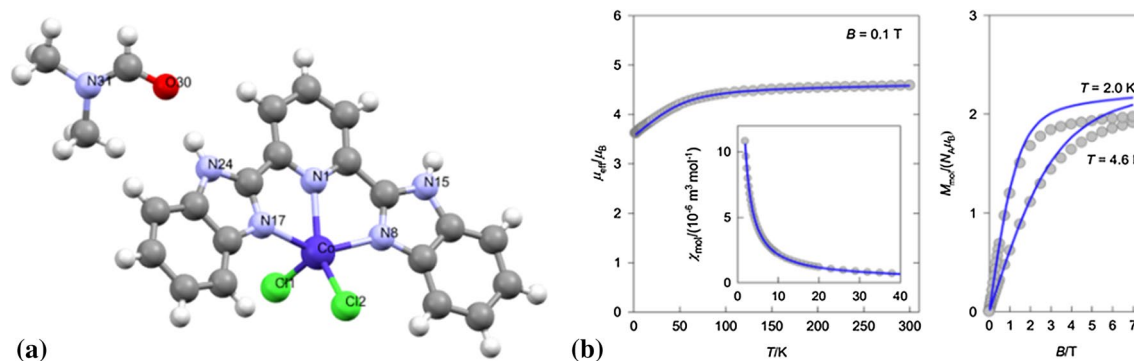
30 K and relaxation time  $\tau_0$  of the order of  $10^{-8}$  s, which is in agreement of characteristic values for HS Co(II) complexes.

The previously mentioned papers [44, 54–56] have been investigating structure and magnetic properties of pentacoordinate Co(II) complexes with the same tridentate N donor ligand **L15** and two halido or pseudohalido terminal ligands. The complexes **17** together with **20** and **19** together with **21** have the same molecular structure, the only difference is the presence or absence of solvent molecule in the crystal structure. Furthermore, the complexes **17**, **20**, **19**, and **21** are isostructural with each other. The calculated Addison parameters  $\tau_5$  [57] are in the range from 0.02 to 0.27 and suggest that coordination polyhedra adopt the shape of distorted square pyramid. The experimental values of  $D$  parameter are positive for all complexes, although the  $D$  for complex **20** and **21** were found to be significantly higher ( $58.4$  and  $47.0$   $\text{cm}^{-1}$ ) than for complexes **17** and **18** ( $14.5$  and  $10.7$   $\text{cm}^{-1}$ , respectively). Nevertheless, the relaxation properties reported in those papers differ significantly. The authors agreed that the Orbach process is not enough for describing of their dynamic magnetic behaviours and other processes should be taken into the consideration. Moreover, Rajnák et al. [54] found two relaxation channels in the complexes **20** and **21**, where the slow LF relaxation channel has been connected with the presence of intermolecular interactions.

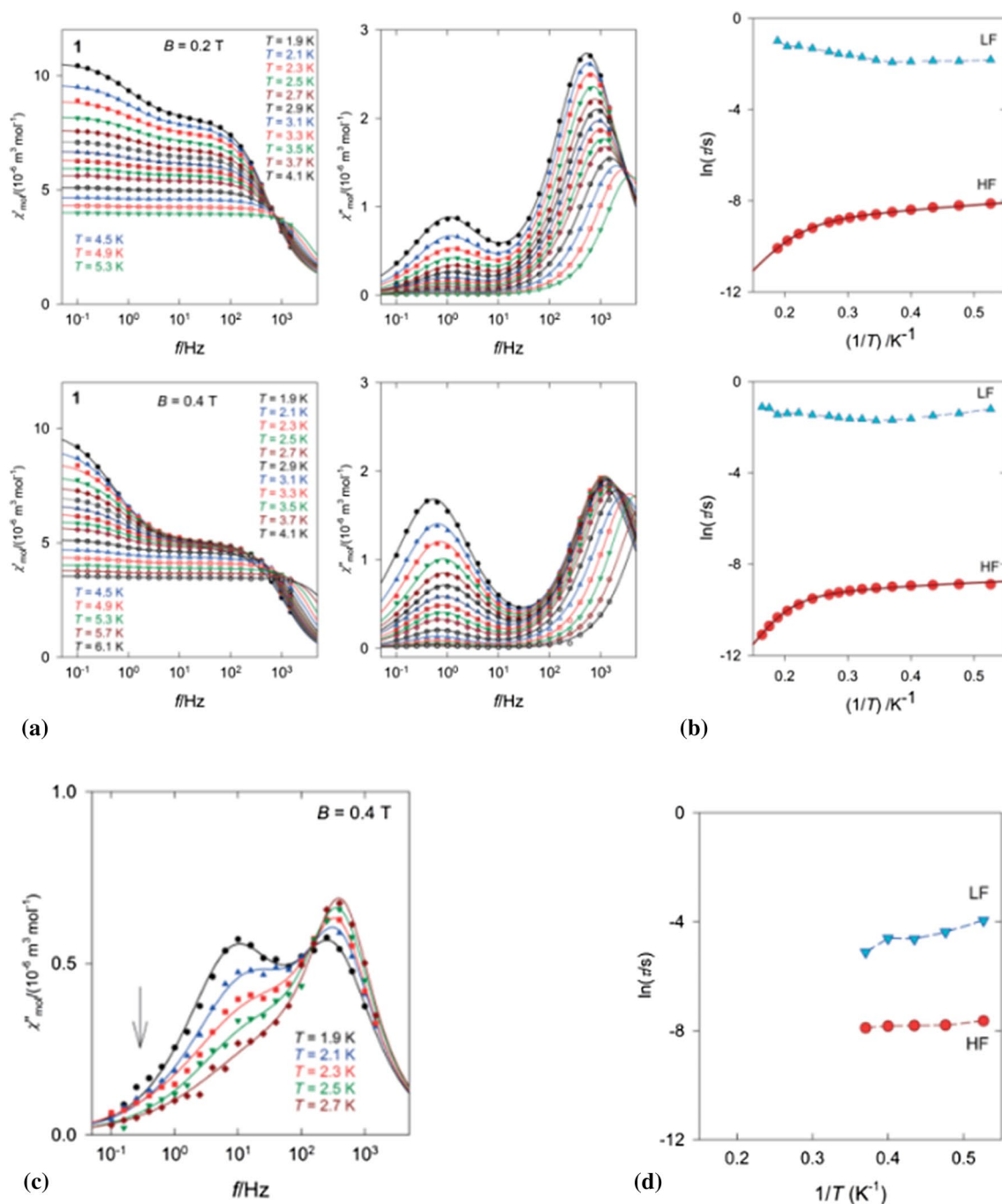
The same group has studied structural and magnetic properties of five pentacoordinate 2,6-bis(pyrazol-1-yl)pyridine–cobalt(II) complexes exhibiting field-induced slow magnetic relaxation [58–60]. The halogenated tridentate ligand 4-iodo-2,6-bis(pyrazol-1-yl)pyridine (**L16**) has been employed for the Sonogashira cross-coupling reaction which allowed to form ligands **L16**–**L20** bearing the *n*-pentylacetylene, *n*-octylacetylene, *n*-decylacetylene, and *n*-dodecylacetylene substituents on 2,6-bis(pyrazol-1-yl)pyridine moiety. Then complexes were prepared via following procedure: the corresponding ligand and  $\text{CoCl}_2 \cdot 6\text{H}_2\text{O}$  were stirred and heated in acetonitrile solution and the blue crystals were

grown by slow evaporation. Structural analysis revealed solvent-free structures of complexes **23** ( $[\text{Co}(\text{L16})\text{Cl}_2]$ ) and **27** ( $[\text{Co}(\text{L20})\text{Cl}_2]$ ), although complexes **24** ( $[\text{Co}(\text{L17})\text{Cl}_2]$ ), **26** ( $[\text{Co}(\text{L19})\text{Cl}_2]$ ), and **25** ( $[\text{Co}(\text{L18})\text{Cl}_2]$ ) consist of the neutral complex molecules together with one, two and three  $\text{CH}_3\text{CN}$  solvent molecules, respectively. All complexes crystallize in monoclinic space group  $P2_1/c$  except **26**, which belongs to the orthorhombic crystal system ( $Pbca$ ). The supramolecular properties of these compounds are also worth mentioning. **23**, **24**, and **27** form supramolecular dimers through short  $\pi$ – $\pi$  contacts, while remaining two form infinite chains that are held by  $\pi$ – $\pi$  stacking. There is no clear correlation of supramolecular interactions with the length of the alkyl tail of the antenna-like ligand. These pentacoordinate complexes adopt the shape of a square pyramid and the  $\tau_5$  parameter ranges from 0.01 to 0.15 in terms of complexes **23**, **24**, **27** and from 0.35 to 0.45 relating to **25** and **26**. The crystal packing of some complexes is viewed on Fig. 16. The value of effective magnetic moment for **25** and **27** remained steady while decreasing temperature. However, below 100 K the curve drops due to the ZFS of Co(II) centers and then it arises again because of ferromagnetic interactions. This kind of behaviour is similar to complex **24**, although opposite to the magnetic data observed for **23** and **26**. The DC magnetic data were fitted using an isotropic exchange model with single-ion anisotropy. The calculated  $D$  parameters for these complexes range from  $-119$  to  $44.2$   $\text{cm}^{-1}$ . The AC susceptibility measurements confirm that the SMM behaviour of reported complexes is observed. Two relaxation channels were observed for all compounds.

The Fig. 17a, c shows AC data of complexes **23** and **24**, respectively. An extended one-set Debye model was used in to fit the frequency dependence of the AC magnetic susceptibility. As it can be seen from Fig. 17, the observed two relaxation processes are behaving differently while increasing temperature. According to expectations, the peak of faster branch of relaxation time decreases with temperature. However, the slower relaxation channel initially tends



**Fig. 14** Molecular structure of complex **20** (a). DC magnetic data for **20**. The lines are fitted by ZFS model (b). Taken with permission from Ref. [54]



**Fig. 15** AC susceptibility and as function of the frequency at  $B_{DC} = 0.2$  T (top **a**) and  $B_{DC} = 0.4$  T (bottom **a**) and  $\ln \tau$  as a function of  $1/T$  (**b**) for **20**. The out-of-phase susceptibility component (**c**) and

the Arrhenius-like plot (**d**) for **22**. Solid lines are fitted using a two-set Debye model. Taken with permission from Ref. [54]

to reduce its value with the temperature and then sudden recovery occurs. The faster relaxation time was characterized using Orbach, direct and Raman processes. In opposite to slower relaxation time, it exhibits typical features of SRM for related complexes. The effective barriers  $U_{\text{eff}}$  range from 15 to 41 K and the relaxation times  $\tau_0$  for the Orbach processed are of the order of  $10^{-7}$  s.

Murugesu and co-workers [61] investigated influence of the ligand field on the SRM along with spin crossover (SCO) effect in mononuclear Co(II) complexes. They were mostly interested in the systems, with the possibility of performing fine-tuning of the ligand field by controlling of the number of coordinated terpyridine ligands (**L21**) and remaining terminal ligands to induce SIM or SCO behaviour. The authors

prepared two pentacoordinated complexes  $[\text{Co}(\mathbf{L21})\text{Cl}_2]$  (**28**),  $[\text{Co}(\mathbf{L21})(\text{NCS})_2]$  (**29**) and one hexacoordinated compound  $[\text{Co}(\mathbf{L21})_2](\text{NCS})_2 \cdot 1.5\text{H}_2\text{O}$  (**30**). This offered a great opportunity to compare magnetic properties in penta- and hexacoordinated Co(II) compounds. The complex **28** was prepared by direct reaction of anhydrous  $\text{CoCl}_2$  and **L21** in THF solution and the green prisms suitable for X-ray measurements were obtained by recrystallization from dichloromethane solution. Compounds **29** and **30** were prepared by reaction of  $\text{Co}(\text{NCS})_2$  and **L21** in dichloromethane and this reaction resulted in green precipitate and brown solution. The green powder was dissolved in DMF/acetone mixture and the slow diffusion of ether allowed the formation of single crystals of **29**. The remaining brown solution was used for slow diffusion of cyclohexane, which resulted in the formation of single crystals of **30**.

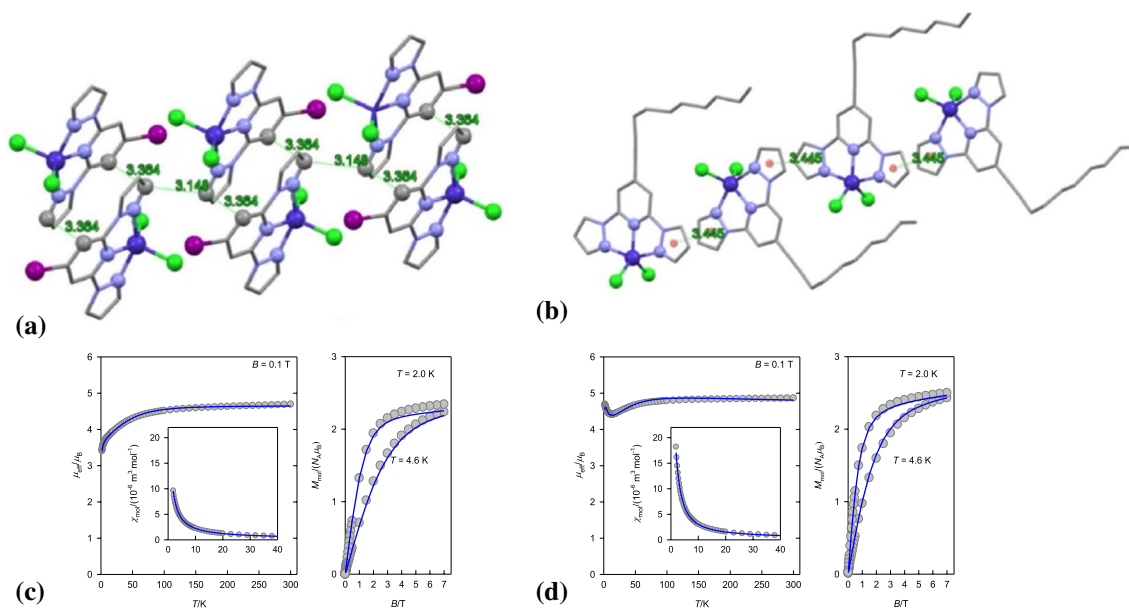
In complex **28**, the Co(II) ion is elevated with respect to the plane formed by three N atoms of ligands **L21** and coordination polyhedron forms distorted square based pyramid. On the other side, the metal centre in **29** is placed within the plane of **L21** causing trigonal bipyramidal shape. The six-coordinate compound **30** adopts distorted octahedral geometry (Fig. 18).

In compounds **28** and **30**, the intermolecular  $\pi$ - $\pi$  stacking of distance between aromatic rings 3.79 Å and 3.70 Å, respectively, is observed. Complex **29** shows a parallel alignment of Co(II) centres with a length of 3.66 Å between terpyridine ligands centroids. DFT calculations revealed HS ground state for complexes **28** and **29**. On the other hand, coordination compound **30** containing the complex cation

$[\text{Co}(\mathbf{L21})_2]^{2+}$  with two tridentated ligands is stabilized in the low-spin state at low temperatures and above 100 K exhibits the gradual SCO, which does not reach the high-spin plateau at high temperatures (Fig. 19). The  $\chi T$  reaches  $1.39 \text{ cm}^3 \text{ K mol}^{-1}$  at 350 K corresponding to 68% of Co(II) metal centres in HS state. Thus, the SRM in **30** is not expectable.

$\chi T$  vs.  $T$  plot proves the high-spin state behaviour of pentacoordinate complexes **28** and **29** (Fig. 19), where the low temperature decrease of  $\chi T$  function is attributed to the presence of high magnetic anisotropy [53, 62]. The values at 300 K are  $3.34 \text{ cm}^3 \text{ K mol}^{-1}$  and  $2.66 \text{ cm}^3 \text{ K mol}^{-1}$  for **28** and **29**, respectively. The  $M$  vs.  $H$  and  $M$  vs.  $HT^{-1}$  plots shows no saturation for **28** and **29**, which can be explained by the presence of high magnetic anisotropy (Fig. 20). In addition, high-frequency EPR measurements were performed on **28** and **30** (Fig. 19b). While the spectra obtained for **28** span a broad field range indicating high magnetic anisotropy, the spectrum of **30** does not indicate anisotropic metal centre. Values of  $g$  for **30** are 2.03–2.19 for  $S=1/2$ , which agrees with results of the magnetic measurements. Moreover,  $g$  values for **28** are associated with HS  $S=3/2$  Co(II) ions.

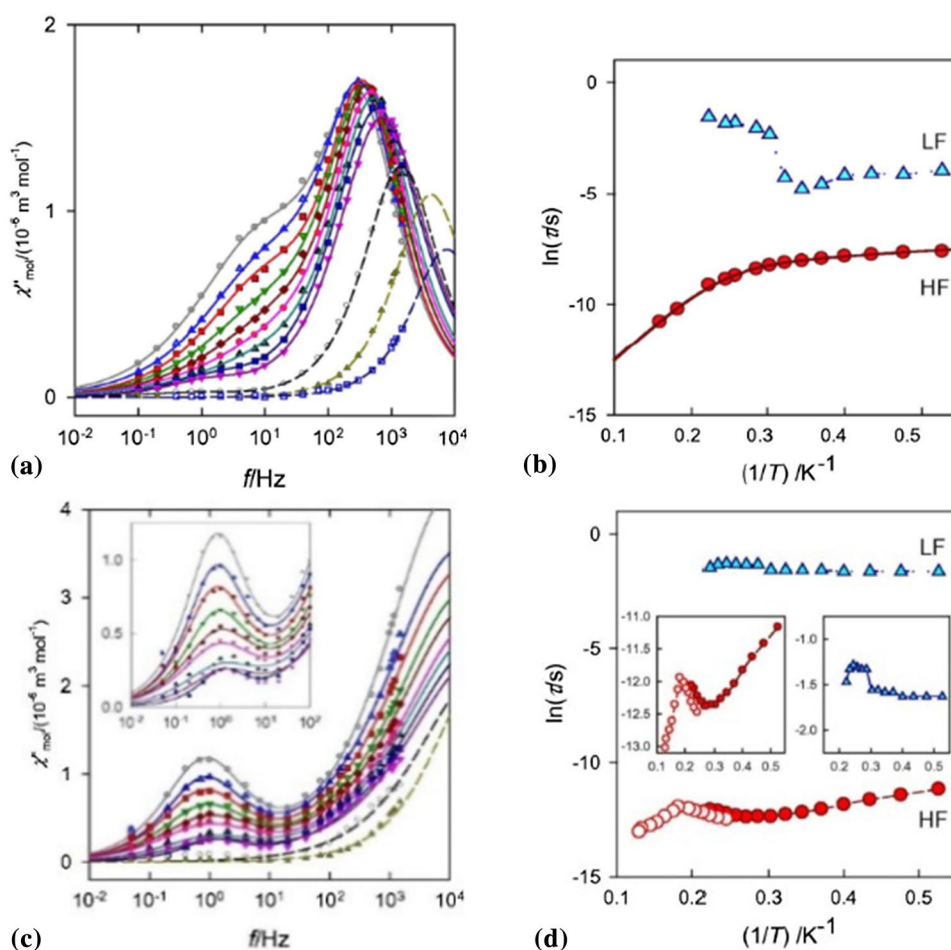
The AC magnetic measurements confirmed SMM behaviour of **28** and **29** (Fig. 21), while according to expectations, no slow relaxation dynamics were observed for **30**. Furthermore, complexes **28** and **29** exhibit the relaxation of magnetization through two pathways—fast and slow relaxation channels. The relaxation parameters  $U_{\text{eff}}$  and  $\tau_0$  of the following values were extracted:  $U_{\text{eff}}=28 \text{ K}$ ,  $\tau_0=1.1 \times 10^{-6} \text{ s}$  (**28**) and  $U_{\text{eff}}=17 \text{ K}$ ,  $\tau_0=5.9 \times 10^{-6} \text{ s}$  (**29**) for fast relaxation



**Fig. 16** Crystal packing of complex **23**—linked dimers (a) and **25**—infinity network through  $\pi$ - $\pi$  stacking (b). Colour code: Co—blue, I—purple, N—violet, C—grey, Cl—green. DC magnetic data of

complex **23** (c) and complex **25** (d). Taken with permission from Ref. [58] (colour figure online)

**Fig. 17** AC susceptibility data for **23** (a, b) and **25** (c, d) at  $B_{DC}=0.2$  T. Taken with permission from Ref. [58]



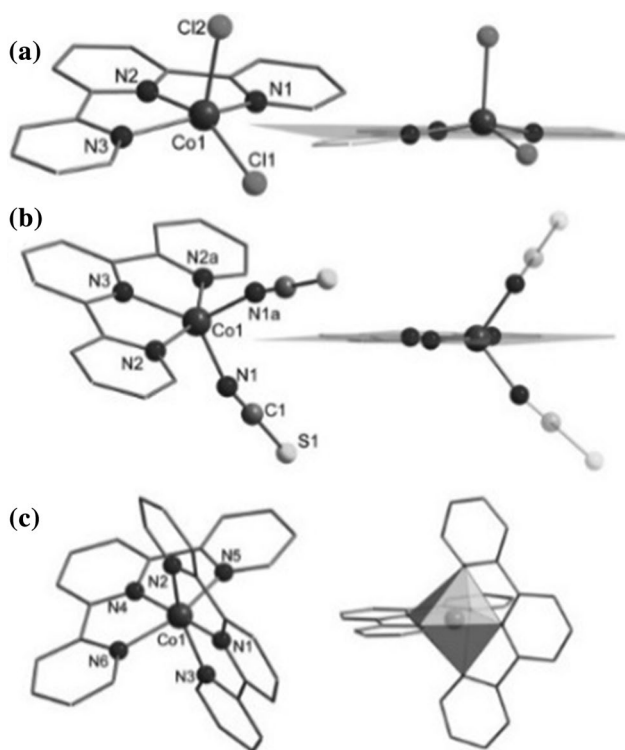
processes and  $U_{\text{eff}}=4$  K,  $\tau_0=7.4\times 10^{-2}$  s (**28**) and  $U_{\text{eff}}=3$  K,  $\tau_0=0.1$  s (**29**) for slow relaxation processes. As it appears from AC data, the change of  $\text{Cl}^-$  ligands for  $\text{NCS}^-$  ligands causes a significant decrease in the energy barrier.

The output of this study revealed that it is possible to control physical and magnetic properties, such as effective anisotropy barrier by tuning ligand field strength around the metal centre as well as its geometry.

The paper of Brachňakov et al. [63] deals with the stereochemistry of coordination polyhedra and its influence on SRM in penta- and hexacoordinate complexes with tridentate N-donor rigid ligands. Authors have prepared a ligand **L22** and used it for the synthesis of three neutral pentacoordinate Co(II) complexes and one hexacoordinate Co(II) ionic compound. The **L22** was synthesized by the following procedure: **L15** (bzimpy) reacted with 3,5-di-*tert*-butylbenzyl bromide in DMSO solution to form two products (**L22** and the minor product **L23**), which were separated using column chromatography. Complexes **31–33** were prepared by complexation of **L22** with corresponding Co(II) salt in acetonitrile solution, whereas **34** was prepared in MeOH solution. Moreover, the authors used small excess of **L22** to prevent formation of pentacoordinate complex in the

synthesis of hexacoordinate complex compound **34**. Single crystal X-ray analysis confirmed the structure of compounds **31–34**. The structure of complex **33** is shown in Fig. 22a. The asymmetric unit of structures **31–33** consists of complex represented by the general formula  $[\text{Co}(\text{L22})\text{X}_2]$ , where  $\text{X}=\text{NCS}^-$ ,  $\text{Cl}^-$ , and  $\text{Br}^-$  for **31**, **32**, and **33**, respectively. The complexes **32** and **33** are isomorphous and isostructural with each other. The asymmetric unit of **34** is expressed by the formula of  $[\text{Co}(\text{L22})_2]\text{Br}_2\cdot 2\text{CH}_3\text{OH}\cdot \text{H}_2\text{O}$ . The authors studied the geometry of coordination polyhedra of compounds by the continuous symmetry measure methodology. The square pyramidal or vacant octahedral geometries were found to be the closest one for **31**. On the other hand, **32** and **33** adopt geometry close to trigonal bipyramid. Moreover, values of  $\tau_5$  distortion parameter were calculated ( $\tau_5=0.3$  for **31**,  $\tau_5=0.46$  for **32**,  $\tau_5=0.41$  for **33**) to indicate intermediate geometry between the square pyramidal and trigonal bipyramidal, slightly closer to square pyramidal ( $\tau_5=0$ ). Compound **34** exhibits a notable distortion from a perfect octahedral geometry that was determined by angular distortion parameter  $\Sigma=136.4^\circ$  [64, 65], calculated from 12 *cis* angles of the hexacoordinate polyhedron acquiring zero values if ideal octahedral geometry is present. The obtained





**Fig. 18** Molecular structures of  $[\text{Co}(\text{L21})\text{Cl}_2]$  (**28**) (a);  $[\text{Co}(\text{L21})(\text{NCS})_2]$  (**29**) (b);  $[\text{Co}(\text{L21})_2]^{2+}$  (**30**) (c). Hydrogen atoms, counterions, and solvent molecules are omitted for the sake of clarity. The plane, which is composed of the three N atoms of **L21** (**28** and **29**) along with the polyhedron around the Co(II) ion (**30**), is displayed shaded (right). Taken with permission from Ref. [61]

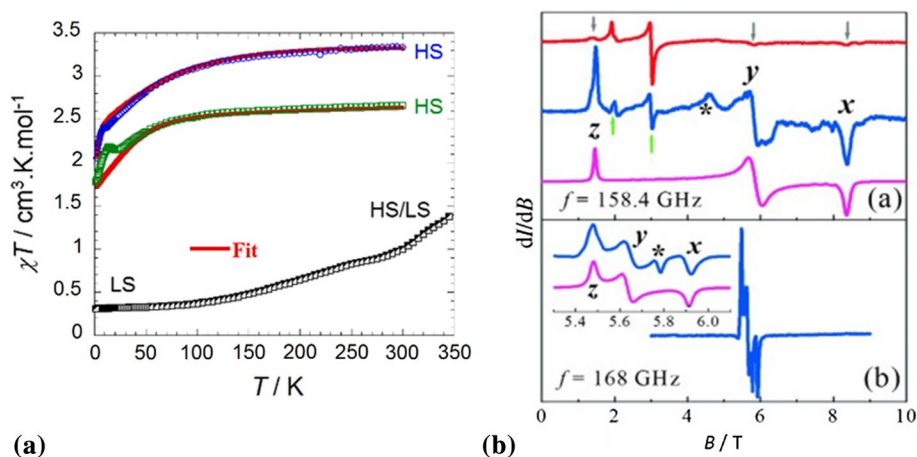
value is typical for HS hexacoordinate Co(II) complexes with terpy-like N-donor ligands. Authors also reported that crystal structures of **31–33** contain several  $\pi$ – $\pi$  interactions between aromatic moieties of neighbouring molecules forming the pseudodimeric couples.

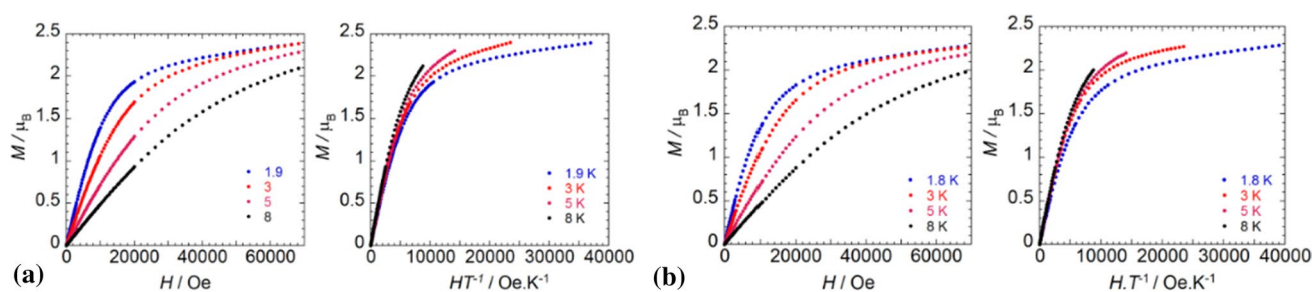
Magnetic characterization at static magnetic field allowed to evaluate ZFS parameters for all three pentacoordinate

complexes. The obtained temperature and field-dependent magnetization data were analysed with respect to spin Hamiltonian and parameters  $D$  and  $E$  were determined (Fig. 22b). The best fits for pentacoordinate complexes **31–33** were acquired with  $D$  in the range from 25 to 39  $\text{cm}^{-1}$  and large rhombicity. Although the positive  $D$  parameter usually suggests easy-plane magnetic anisotropy, the large value of  $E/D$  indicates that the easy-axis magnetic anisotropy can be present. Indeed, this indication was confirmed by CAS-SCF/NEVPT2 calculations, which showed axial character of magnetic anisotropy. On the other hand, the ZFS parameters of hexacoordinate Co(II) compound **34** was not possible to determine from the static magnetic measurements. Authors claim that spin Hamiltonian approach is not operative for this system.

The dynamic magnetic measurements confirmed that **31–34** exhibit field-induced slow magnetic relaxation. The collected sets of  $\chi'$  and  $\chi''$  susceptibilities for complexes **31**, **32**, and **34** were fitted using one-set Debye model, since frequency-dependent susceptibility measurements revealed single-relaxation process. In **31** and **32**, however, the low frequency out-of-phase signal suggests the presence of poorly resolved second relaxation channel. The extracted temperature dependencies of relaxation time were fitted to relaxation Eq. (13) aiming the combination of Orbach and direct processes. The best fit parameters  $U_{\text{eff}} = 24.6$  K,  $\tau_0 = 5.9 \times 10^{-7}$  s for **31** and  $U_{\text{eff}} = 18.9$  K,  $\tau_0 = 2.9 \times 10^{-7}$  s for **32**, respectively, are typical for pentacoordinated Co(II) SIMs. The dynamic magnetic data of **33** show the presence of two relaxation channels (Fig. 22c) and they were analysed using the two-set Debye model. The AC susceptibility of complex **33** was measured at four different static magnetic fields to better understand both low-frequency (LF) and high-frequency (HF) channels. In addition, the single HF process obtained at lower fields was analysed using one-set Debye model. The appearance of LF relaxation channel in compound **33** was diminished in the sample dispersed with

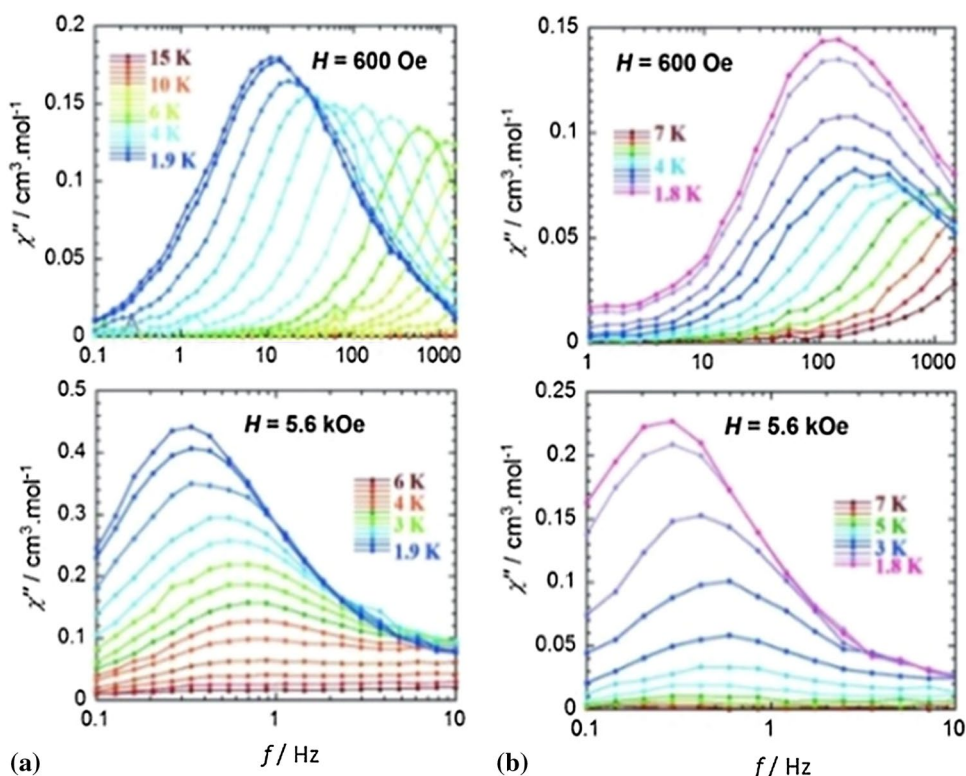
**Fig. 19** **a** Temperature dependence of the magnetic susceptibility for complexes **28** (blue), **29** (green), and **30** (black). Fitted lines are red. **b** Powder EPR spectra and simulations for complexes **28** (a) and **30** (b); Exp. 1 (blue) was performed at 2.5 K; Exp. 2 (red) was completed several months later on the same powder pellet, at 20 K. Inset: Expanded view of the spectra. Taken with permission from Ref. [61] (colour figure online)





**Fig. 20** Magnetization ( $M$ ) as a function of field ( $H$ ) plotted as  $M$  vs.  $H$  and  $M$  vs.  $HT^{-1}$  for complex **28** (a) and **29** (b). Taken with permission from Ref. [61]

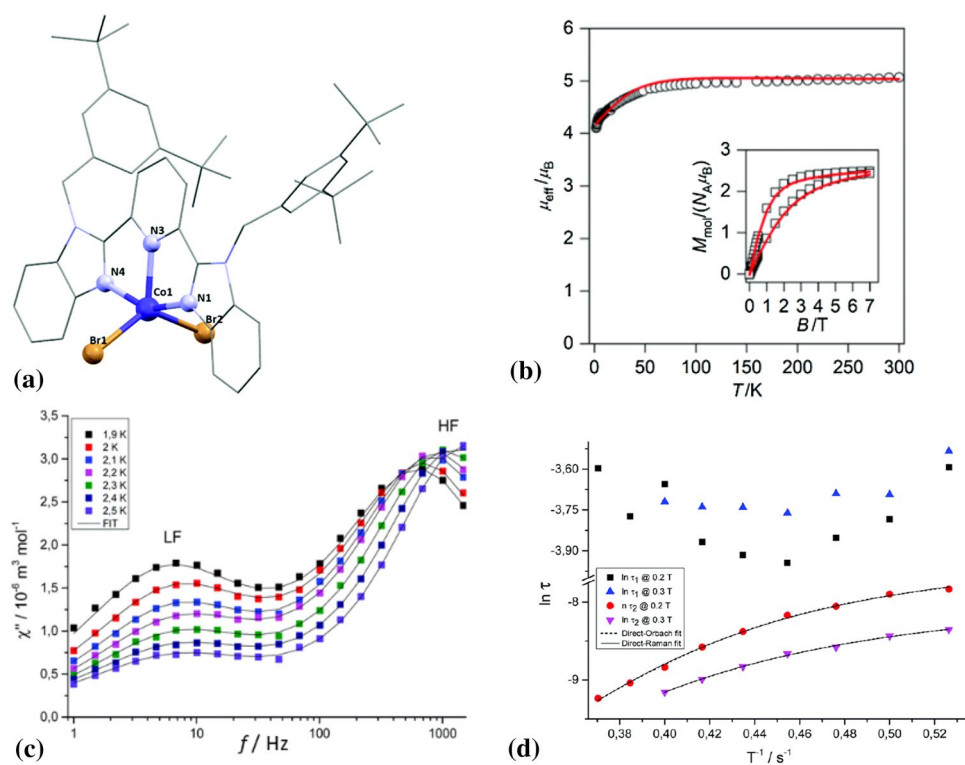
**Fig. 21** Frequency ( $f$ ) dependence of the out-of-phase magnetic susceptibility,  $\chi''$ , at the indicated applied fields ( $H$ ) and temperature ranges for **28** (a) and **29** (b). Taken with permission from Ref. [61]



diamagnetic eicosane and thus, its origin can be connected with the presence of intermolecular interactions. The values of effective barrier and extrapolated relaxation times for **33** were found to be  $U_{\text{eff}} = 19.1$  K,  $\tau_0 = 9.2 \times 10^{-8}$  s at 0.05 T and  $U_{\text{eff}} = 21.22$  K,  $\tau_0 = 4.8 \times 10^{-6}$  s at 0.3 T (Fig. 22d). They are highly comparable with those obtained for the isostructural chlorido complex **32**. The AC susceptibility data for **34** revealed single channel relaxation, which was possible to analyse with the single Orbach process with the values of  $U_{\text{eff}}$  and  $\tau_0$  are 9.5 K and  $6.7 \times 10^{-7}$  s, respectively. The authors also mentioned that to bring more light to relaxation processes, they attempted to prepare Zn(II) doped compounds **31–34**. Unfortunately, in all four cases

the suspension of dissolved Co(II) complex and precipitated hexacoordinated Zn(II) complex was found.

In general, according to previously mentioned papers, the pentacoordinate Co(II) complexes with tridentate N-donor ligands adopt coordination geometry of distorted square pyramid or close to trigonal bipyramid. The  $D$  parameters usually lie in the range of  $-100$  to  $+100$   $\text{cm}^{-1}$ . The effective anisotropy barriers adopt values near 50 K and relaxation times  $\tau_0$  are generally of the order of  $10^{-7}$  s. Overall, there are several relaxation processes (Orbach, Raman, and direct) usually found in Co(II) SMMs and this makes the magnetic measurements and data extracting very complex. So far, no relations between the coordination geometry, ZFS parameters and AC parameters data were found, although it is clear



**Fig. 22** Molecular structure of **33**. Hydrogen atoms, uncoordinated anions and lattice solvent molecules are omitted for the sake of clarity. Colour code: C—grey; N—blue; Cl—green; Br—brown; S—yellow (a). Magnetic data for **33** are shown as the temperature dependence of the effective magnetic moment and as the isothermal magnetizations in the insets. The empty symbols represent the experimental data and red solid lines represent the fitted data (b). Frequency-dependent out-of-phase  $\chi''$  components of AC susceptibil-

ity for compound **33** recorded at an applied static magnetic field 3000 Oe. Solid lines represent the fits using the two-component Debye model (c). Temperature dependency of the resulting relaxation times  $\tau_1$  of the LF channel and  $\tau_2$  of the HF channel recorded at fields 2000 and 3000 Oe. The fits of the resulting relaxation times  $\tau_2$  with the combination of the direct and Orbach processes using are viewed as dashed lines and the combination of the Raman and direct processes are viewed as solid lines (d) [63] (colour figure online)

that even a tiny change of geometry causes the change in dynamic magnetic properties.

Nemec et al. [66] studied field-induced SRM in a mononuclear pentacoordinate Co(II) compound. Although the most pentacoordinate Co(II) SIMs consist of tridentate heterocyclic N-donor ligand and two halido or pseudo-halido ligands [60, 61], in this work, the authors reported SMM behaviour of Co(II) complex consisting of bidentate N-donor ligand **L24** and three monodentate ligands. The crystal structure and synthesis of compound **35** with the formula  $[\text{Co}(\text{L24})(\text{DMSO})\text{Cl}_2]$  was already published and well described [67]. The authors obtained X-ray quality crystals after dissolving of compound  $[\text{Co}(\text{L24})\text{Cl}_2]$  in DMSO and by slow diffusion of diethylether. In the structure, bond lengths of coordination polyhedron are notably dependent on the nature of the coordinated ligand and vary from 2.052 to 2.356 Å for C–N and C–Cl. Based on the value of Addison parameter  $\tau_5=0.54$ , the shape of coordination polyhedron was found to be somewhere in the middle of the Berry pseudorotation pathway, which describes the transformation square pyramid to trigonal bipyramid. The

crystal structure contains weak non-covalent intermolecular interactions, such as  $\pi$ – $\pi$  stacking and hydrogen bonds. The compound was first characterized at static magnetic field and results of experimental fits were supported by ab initio calculations. The effective magnetic moment adopts significantly higher values ( $4.84 \mu_B$ ) than the expected spin only value for HS Co(II) ( $3.87 \mu_B$ ), which can be explained by the strong contribution of spin–orbit coupling to the ground state magnetic moment. There is a continuous drop of  $\mu_{\text{eff}}$  below 50 K due to ZFS and both temperature- and field-dependent magnetic data were successfully fitted with negative  $D$  parameter ( $-17 \text{ cm}^{-1}$ ) and large rhombicity ( $E/D=0.24$ ). The calculated parameters ( $D=-17.7 \text{ cm}^{-1}$ ,  $E/D=0.31$ ) are in very good agreement with experimental parameters. Moreover, the  $g$ -tensor values were obtained as  $g_1=2.18$ ,  $g_2=2.32$ ,  $g_3=2.46$  ( $g_{\text{iso}}=2.32$ ). To bring a better estimation of  $g$  tensors and  $D$  parameter, the HF EPR spectra were recorded although; the authors could not have determined the value of  $D$ . The best fits were for  $E/D=0.33$ ,  $g_x=2.6$ ,  $g_y=2.4$ ,  $g_z=2.3$ . The AC susceptibility investigation revealed field-induced SRM with a single relaxation

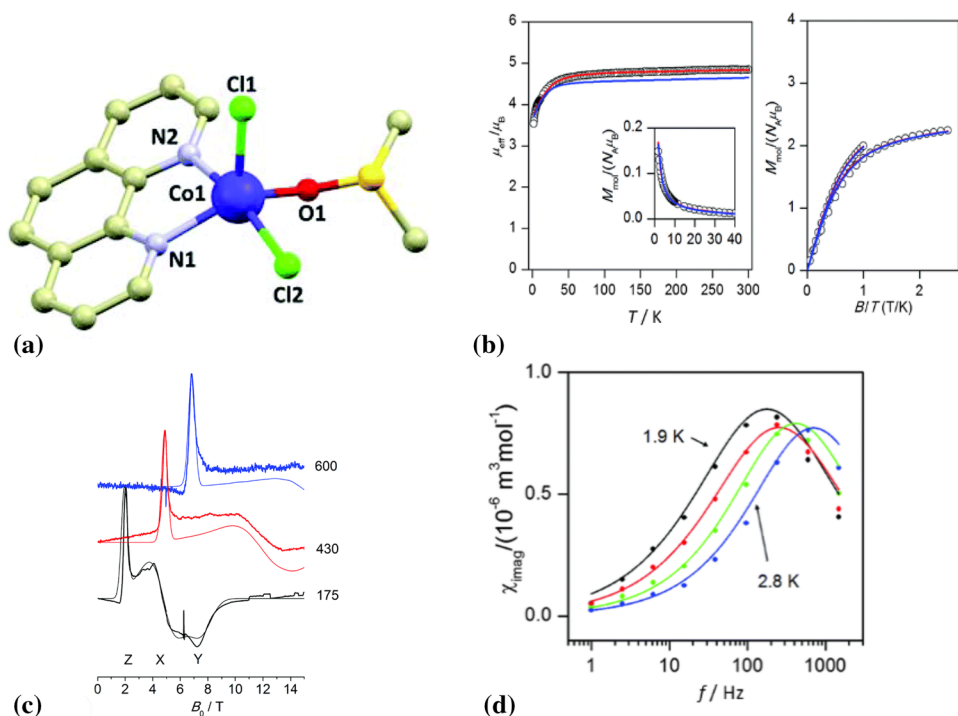
channel. Temperature dependency of relaxation time was successfully analysed by Orbach process with parameters  $U_{\text{eff}} = 10.4$  K,  $\tau_0 = 5.69 \times 10^{-9}$  s. The value of the effective anisotropy barrier was found to be much lower than theoretical predictions ( $U_{\text{eff}} \approx 55$  K), which is considered as common disagreement and it was also observed in a plethora of other reported pentacoordinate Co(II) SIMs [31, 60, 61]. A possible explanation is that lowering  $U_{\text{eff}}$  is affected by QTM, which is connected to large rhombicity. In summary, several relaxation processes (Orbach, Raman and direct) are usually found in Co(II) SIMs, making them very complex (Fig. 23).

Woods et al. [68] studied relaxation dynamics of identical bipyramidal Co(II) compounds with different local symmetries and packing arrangements. They reported a family of isostructural, mononuclear Co(II) compounds with trigonal bipyramidal coordination geometry. Tetradentate ligand **L25** tris(2-pyridylmethyl)amine was chosen to provide a rigid backbone for Co(II) centres as well as leave one free coordination place. The complexes of formula  $[\text{Co}(\text{L25})(\text{CH}_3\text{CN})_6](\text{BF}_4)_2$  (**36**),  $[\text{Co}(\text{L25})\text{Cl}]\text{Cl}$  (**37**),  $[\text{Co}(\text{L25})\text{Br}]\text{Br}$  (**38**), and  $[\text{Co}(\text{L25})\text{I}]\text{I}$  (**39**) were reported in the mentioned work, while the ligand **L25** and complex **36** were published earlier [69, 70]. Furthermore, by different synthetic approaches was possible to prepare cubic (marked with “c”) and triclinic (marked with “t”) polymorphic phases of **37** and **38**. Synthesis of compounds was performed under the dry and inert conditions, where one equivalent of **L25** and corresponding Co(II) salt were dissolved in acetonitrile (**36**, **37c**, **38c**, and **39**) or methanol (**37t** and **38t**). Then, X-ray quality single crystals were obtained by slow diffusion of diethyl ether vapours into the filtrate (**36**) or by layering with diethylether (**37t**, **38t**, **38c**, and **39**) with over toluene (**37c**). Compound **36** crystallizes in the monoclinic space group  $P2_1/c$ , **37c** and **38c** crystallize in cubic space group  $P2_13$  and **37t**, **38t**, and **39** crystallize in triclinic space group  $P\bar{1}$ . The shapes of coordination polyhedra are distorted trigonal bipyramids and consist of four nitrogen atoms from ligand **L25** and the remaining coordination place is occupied either with one nitrogen atom of acetonitrile molecule or corresponding halido donor atom. All reported compounds show similar magnetic properties recorded at the static magnetic field (Fig. 24b). The room temperature  $\chi T$  values are higher than expected for  $S = 3/2$  system with  $g = 2$ , which is an indication of orbital momentum contribution to the overall magnetization of compounds. The decrease of  $\chi T$  values is apparent in the low temperature region, which is the fingerprint of ZFS.  $M$  vs.  $H$  measurements at 1.8 K did not saturate at the highest available field, which is another indication of the high anisotropy of the systems. The fitting procedures along with ab initio calculations resulted in a positive  $D$  and small rhombicity for **36** and negative  $D$  values for compounds **37–39** (see Table 2). Dynamic

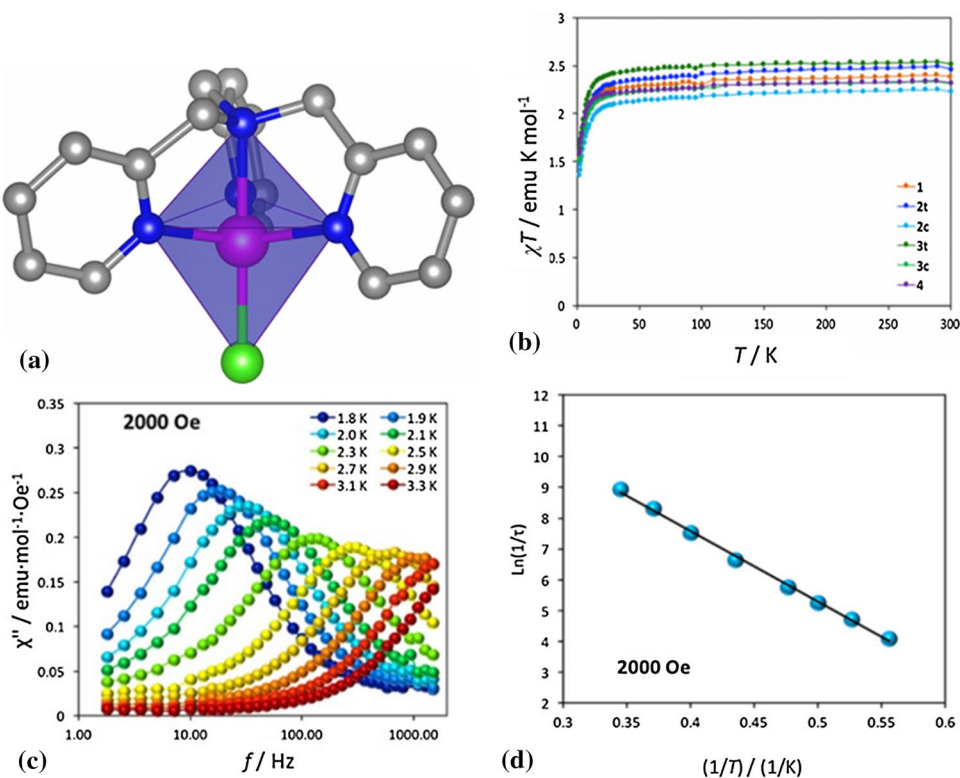
magnetic measurements revealed obvious SMM behaviour in the compounds **36**, **37c**, and **38c** in the presence of applied DC field. Moreover, the compound **37c** shows a weak out-of-phase signal at zero DC field, which does not reach the maximum at the highest measured frequency of AC field. The one-set Debye model was used to analyse magnetic data for **36**, **37c**, and **38c** and two-set Debye model for data of **37c**. From the Arrhenius plot, the relaxation parameters  $U_{\text{eff}}$  and  $\tau_0$  of the following values were extracted.  $U_{\text{eff}} = 21.6$  K,  $\tau_0 = 1.7 \times 10^{-8}$  s (at 1000 Oe),  $U_{\text{eff}} = 21.6$  K,  $\tau_0 = 2.98 \times 10^{-8}$  s (at 400 Oe), and  $U_{\text{eff}} = 17.7$  K,  $\tau_0 = 8.06 \times 10^{-8}$  s (at 1600 Oe) for **36**, **37c**, and **38c**, respectively. At the applied field, the triclinic polymorphs **37t**, **38t**, and **39** show some signal in  $\chi''$  at high frequencies, but no maximum was observed at the highest measured frequency. Such behaviour of AC susceptibility can be explained by the presence of shorter intermolecular Co...Co separations allowing strong dipolar interactions and, therefore, fast spin relaxation.

Rajnák et al. [71] studied field-supported slow magnetic relaxation in two mononuclear hexacoordinate Co(II) complexes containing four equatorial 4-benzylpyridine (**L26**) and two axial chlorido or thiocyanato ligands. The coordination polyhedron of **40**  $[\text{Co}(\text{L26})_4\text{Cl}_2]$  corresponds to elongated tetragonal bipyramid because of long Co–Cl axial distances (2.44 Å) relative to equatorial Co–N distances (average distance 2.21 Å). On the other hand, the axial thiocyanato terminal ligands in complex **41**  $[\text{Co}(\text{L26})_4(\text{NCS})_2]$  form shorter bonds which resulted in the compressed tetragonal bipyramidal shape of coordination polyhedron. DC magnetic measurements revealed that effective magnetic moment for **40** adopts room-temperature value of  $4.97 \mu_B$ , which gradually decreases upon cooling until it reaches  $\mu_{\text{eff}} = 3.6 \mu_B$  at  $T = 1.9$  K. The molar magnetization saturates at  $2.16 N_A/\mu_B$  at  $T = 2$  K and  $B = 7$  T. This is lower value than expected one for  $S = 3/2$  system and it indicates a substantial ZFS. The magnetic functions for **41** show similar behaviour. Field dependence of the molar magnetization and temperature dependence of the molar magnetic susceptibility were fitted simultaneously to the model of spin Hamiltonian, which yielded  $D$  of  $+106$  and  $+90.5 \text{ cm}^{-1}$  for **40** and **41**, respectively. These values are in good agreement with the averaged ZFS parameters predicted by ab initio calculations. The AC magnetic data confirmed a fast magnetic relaxation in the absence of the magnetic field; however, reported complexes show a field-induced slow magnetic relaxation mediated through multiple relaxation channels. For both compounds, there is a dominant relaxation process in the high-frequency region (around  $\tau(\text{HF}) = 0.8$  ms) of AC magnetic susceptibility recorded at  $T = 1.9$  K and 2000 Oe. The second channel appears as a satellite peak at the low-frequency region of out-of-phase component with  $\tau(\text{LF}) \approx 40$  ms. In addition, this peak splits at  $H_{\text{DC}} = 4000$  Oe, and therefore, the increase of static field causes appearance of the third relaxation

**Fig. 23** Molecular structure of **35** (a). Temperature dependence of the effective magnetic moment and molar magnetization measured at  $B=0.1$  T in the inset, and isothermal reduced magnetizations measured at  $T=2$  and 5 K. Empty circles: experimental data. Red and full blue lines: calculated data (b). HFEPR spectra of **1** at 5 K and different frequencies (in GHz) (c). Out-of-phase molar susceptibilities for **35** at  $B_{DC}=0.1$  T. Full points—experimental data, full lines—fitted data (d). Taken with permission from Ref. [66] (colour figure online)



**Fig. 24** Molecular structure of compound **37c** emphasizing the trigonal bipyramidal geometry (purple polyhedron) with the equatorial plane defined by the three pyridine N atoms of **L25**. Colour code: Co—pink, Cl—green, N—blue, C—grey. Hydrogen atoms have been omitted for clarity (a). The plot of  $\chi T$  vs.  $T$  under a 1000 Oe applied field for compounds **36–39** (b). Magnetic data (AC) for **37c**, and at different temperatures (c). Arrhenius plots for **37c**. The black line is the fit to the Arrhenius equation (d). Taken with permission from Ref. [68] (colour figure online)



channel. Both compounds show similar evolution of the in-phase and out-of-phase magnetic susceptibility data, which were fitted by three-set Debye model and temperature dependency of  $\tau(\text{HF})$  relaxation times were analysed concerning the extended relaxation equation. For complex

**40**, the authors obtained the best fits by considering a single Raman process with parameter  $C=4.16 \text{ T}^{-5} \text{ K}^{-1} \text{ s}^{-1}$  at  $H_{DC}=4000$  Oe. However, the unusual feature was observed at low temperatures for **41**. Upon the heating,  $\tau(\text{HF})$  relaxation time increases with the temperature, passes through

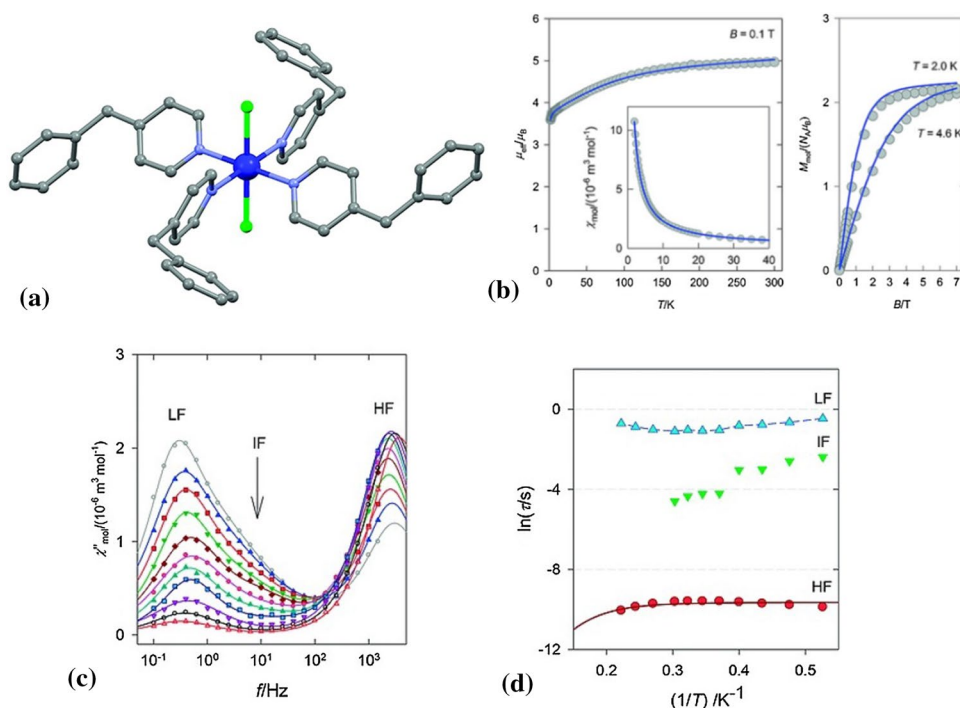
a round maximum around 3 K and then decreases. Such unexpected behaviour did not allow successful analysis of Arrhenius-like plot at the low temperature region. The quantitative parameters resulting from the data fitting of the high temperature region of  $\tau(\text{HF})$  are not comparable with **40**. At 4000 Oe, the  $\ln\tau$  vs.  $1/T$  function was analysed with Orbach process, which resulted in parameters  $U_{\text{eff}} = 27.7$  K and  $\tau_0 = 0.3 \times 10^{-6}$  s. According to the authors, the existence of the LF branch is conditioned by intermolecular interactions. Those interactions are disrupted by increasing temperature and the LF branch disappears progressively with increasing temperature. This is probably the origin of a higher separation of LF and HF components with an increasing magnetic field (Fig. 25).

Shi et al. [73] studied syntheses, structures and magnetic properties of three two-dimensional Co(II) SMMs with octahedral geometry. Although each compounds crystallize in different space groups, they all have similar 2D structures, where the two Co(II) centres are bridged by the ligand 4,4'-dipyridyl sulfide (**L27**). The coordination geometry of the Co(II) centres adopts a general  $\text{CoN}_4\text{X}_2$  octahedral environment formed by four equatorial N atoms from four ligands **L27** and two axial  $\text{X}^-$  atoms ( $\text{X} = \text{Cl}^-$ ,  $\text{Br}^-$ , or O). This work aimed to synthesize 2D coordination polymers with different axial coordination atoms and to study structural and magnetic changes caused by these differences. The flexible organic spacer **L27** that they used is capable of forming 2D frameworks and preventing magnetic interactions between Co(II) ions. The compound of formula  $[\text{Co}(\text{L27})_2\text{Cl}_2]_n$  (**42**),  $[\text{Co}(\text{L27})_2\text{Br}_2]_n$  (**43**), and  $[[\text{Co}(\text{L27})_2(\text{H}_2\text{O})_2]_2 \cdot (\text{H}_2\text{O})_4]_n$  (**44**) were synthesized as follows: a mixture of **L27** and corresponding Co(II) salt were dissolved in methanol (**42**) or methanol/acetonitrile (**43**, **44**), stirred and then kept still for slow evaporation to form pink (**42**, **43**) or orange (**44**) crystals suitable for X-ray diffraction. The structure of compound **42** (Fig. 26a) was already reported previously [72], yet the authors measured it for the sake of consistency. The crystal systems and space groups are monoclinic  $P2_1/c$  for **42**, orthorhombic  $Pccn$  for **43** and  $Pbca$  for **44**. All compounds **42–44** have similar 2D framework structures, where the Co(II) centres are placed in distorted octahedra and bridged by long spacer ligands **L27**. The  $\text{Co}-\text{N}_{\text{eq}}$  bond lengths vary from 2.13 to 2.28 Å. The  $\text{N}_{\text{eq}}-\text{Co}-\text{N}_{\text{eq}}$  bond angles for **42–44** are very close to each other, while  $\text{X}_{\text{axial}}-\text{Co}-\text{X}_{\text{axial}}$  ( $\text{X} = \text{Cl}$ ,  $\text{Br}$ , O) bond angles are very close to  $180^\circ$ . The  $\text{Co}-\text{O}_{\text{axial}}$  lengths in **44** (2.09 Å) are significantly shorter than  $\text{Co}-\text{Cl}_{\text{axial}}$  in **42** and  $\text{Co}-\text{Br}_{\text{axial}}$  in **43**, which are of lengths 2.42 Å and 2.57 Å for **42** and **43**, respectively. As far as magnetic properties are going, the  $\chi T$  values at room temperature for **42–44** vary from 3.08 to 3.41  $\text{cm}^3 \text{mol}^{-1} \text{K}$  and they are higher than expected values for an isolated HS  $d^7$  Co(II) cation ( $S = 3/2$ ). By lowering the temperature, the values decrease smoothly and then it is a

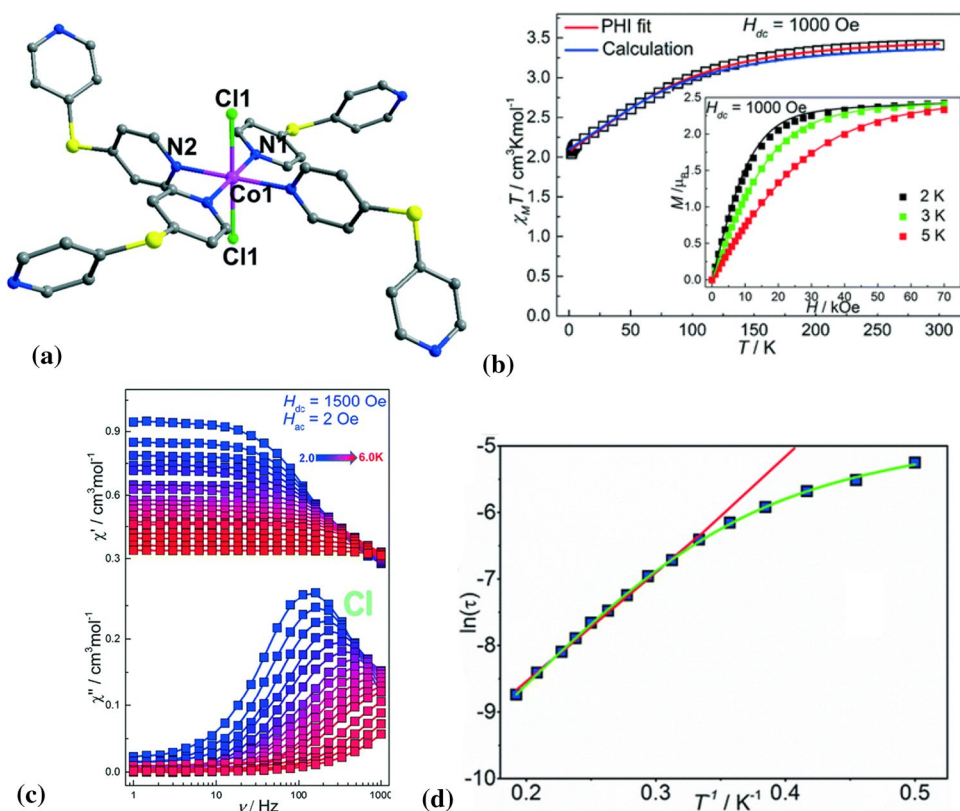
sudden drop below 100 K to reach values of range 1.76–2.05  $\text{cm}^3 \text{mol}^{-1} \text{K}$  at 2 K (Fig. 26b). This drop is mainly caused by the magnetic anisotropy of Co(II) ions and ZFS. In addition, the field-dependent magnetization data for **42–44** were measured at 2 K, 3 K, and 5 K. At 2 K, the magnetization saturates at the high magnetic field to value 2.31–2.42  $\mu_{\text{B}}$ , which is below the expected saturation value for the single HS Co(II) centre. Nevertheless, all these data support the presence of significant magnetic anisotropy originating from the spin–orbit coupling and orbital contribution. The magnetic data were further analysed and experimental values of  $D$  were obtained as  $D = 27.2$ , 28.0, and 9.5  $\text{cm}^{-1}$  for **42–44**. However, the calculation results suggest very strong spin–orbit coupling, and therefore, the description of their magnetic properties using the spin Hamiltonian seems meaningless. There was no out-of-phase susceptibility signal observed under a zero DC field, which indicates fast relaxation of magnetization due to the quantum tunnelling of magnetization (QTM) that is observed in the majority of Co(II) based SIMs. However, all compounds displayed  $\chi''$  a peak in the presence of a small DC field (Fig. 26c), which makes them field induced SIMs. The AC magnetic data were fitted using a generalized one-set Debye model and the temperature-dependent relaxation time was then analysed to extract the effective energy barrier  $U_{\text{eff}}$ . The high temperature linear regime of the Arrhenius plot ( $\ln(\tau)$  vs.  $T^{-1}$ ) was fitted using the Arrhenius equation (Orbach process; Fig. 26d) giving the energy barrier  $U_{\text{eff}} = 12.43$ , 27.0, and 28.8 K with relaxation times  $\tau_0 = 2.4 \times 10^{-5}$ ,  $4.8 \times 10^{-6}$ , and  $1.4 \times 10^{-6}$  s for **42–44**, respectively. The deviation from Arrhenius behaviour at low-temperature region is often connected to multiple relaxation pathways, such as QTM, direct, Raman, and Orbach relaxation processes. The best fit parameters considering these processes gave the energy barriers  $U_{\text{eff}} = 15.8$ , 41.6, and 36.4 K for **42–44**, respectively, and they are more significant than barriers considering only the thermally activated relaxation process. To sum it up, the authors report that although the axial coordination atoms have an obvious influence on their structures and thus the magnetic properties, there is still no clear conclusion on the relations between the magnetic anisotropy and axial ligands based on the results obtained in this work.

Rajnák et al. [74] studied an effect of the distant substituent on the slow magnetic relaxation in the mononuclear Co(II) complex with pincer-type ligands. A hexacoordinated complex **45** of formula  $[\text{Co}(\text{L28})_2](\text{mdnbz})_2$  ( $\text{mdnbz} = 4\text{-methyl-3,5-dinitrobenzoate}$ , Fig. 27a) was prepared by mixing of stoichiometric amounts of  $\text{Co}(\text{OAc})_2 \cdot 4\text{H}_2\text{O}$ , 2,6-dimethanolpyridine (**L28**), and 4-methyl-3,5-dinitrobenzene acid in hot water. Then, light pink X-ray quality crystals were grown and collected after slow evaporation. Authors compared properties of **45** with already reported analogous complex **46**  $[\text{Co}(\text{L28})_2](\text{dnbz})_2$ ,

**Fig. 25** Molecular structure of compound **40**. Colour code: Co—blue, Cl—green, N—violet, C—grey. Hydrogen atoms have been omitted for clarity (a). DC magnetic data for **40**. Lines indicate the fits with the ZFS model (b). Out-of-phase AC susceptibility component for **40** (c). Arrhenius-like plot for **40**. The solid lines are fitted (d). Taken with permission from Ref. [71] (colour figure online)



**Fig. 26** Molecular structure of **42**. Hydrogen atoms are omitted for the sake of clarity. Colour code: Co—pink, S—yellow, N—blue, C—grey (a). Magnetic data for **42** Insets: Field-dependent magnetization  $M(H)$  plots at different temperatures. The red lines in the  $\chi T$  curves and the lines in all the  $M(H)$  curves are fits, while the blue lines in the  $\chi T$  curves correspond to the ab initio calculations. b Frequency-dependent in-phase and out-of-phase  $\chi''$  components of AC susceptibility for compound **42** recorded at an applied static magnetic field 1500 Oe. c Arrhenius plot for **42**. The red lines show the fits of the data to the Arrhenius law assuming the Orbach relaxation mechanism; green lines are fits assuming multiple relaxation pathways (d). Taken with permission from Ref. [73] (colour figure online)



where  $\text{dnbz} = 3,5\text{-dinitrobenzoate anion}$  [75], which possesses a non-methylated counter anion and identical complex cation. Compound **45** crystallizes in the monoclinic space group  $C2/c$  and molecular structure consists of one

complex dication which charge is balanced by two uncoordinated  $\text{mdnzbz}$  anions. Hexacoordinate coordination polyhedron of compressed tetragonal bipyramidal shape consists of two pyridine N axial and four hydroxyl O equatorial

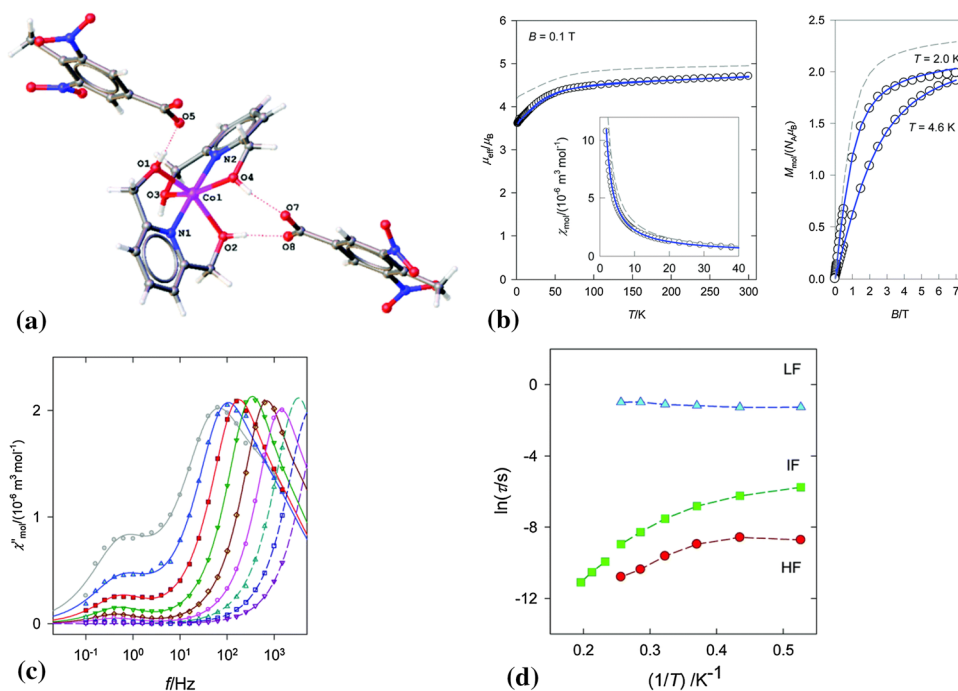
atoms from each of two neutral tridentate **L28** ligands. The one complex cation  $[\text{Co}(\mathbf{L28})_2]^{2+}$  and two *mdnbz* anions are connected through (O–H...O) hydrogen bonds into a 1D supramolecular chain (Fig. 27a). Furthermore, the supramolecular structure is extended into the 3D network via another O–H...O hydrogen bond formed between neighbouring molecules' carboxylic and alcohol groups. On the other hand, the complex **46** crystallizes in space group  $P\bar{1}$ , and it does not form any supramolecular chains.

Compound **45** was characterized by static and dynamic magnetic measurements. At  $T=300$  K, the effective magnetic moment adopts a value of  $\mu_{\text{eff}}=4.70 \mu_{\text{B}}$ , which slightly decreases with decreasing temperature down to  $4.48 \mu_{\text{B}}$  at  $T=100$  K (Fig. 27b). Upon further cooling, the decrease of  $\mu_{\text{eff}}$  is more pronounced, which is related to ZFS phenomenon always present in hexacoordinated Co(II) complexes. The effect of ZFS is also confirmed by the value of magnetization per formula unit, which saturates to  $2 N_{\text{A}}\mu_{\text{B}}$  at  $T=2$  K and high magnetic fields. The magnetic susceptibility and magnetization data fitting resulted in the  $D=50 \text{ cm}^{-1}$  and  $E=10.2 \text{ cm}^{-1}$ . Contrary to this, the ZFS parameters obtained from *ab initio* show significantly different values  $D=-69.0 \text{ cm}^{-1}$ ,  $E=0.19$  and the average  $g_{\text{iso}}=2.38$ . The experimental value of  $D$  parameter is positive and the authors report that it is more realistic than the calculated one, as it can be seen from a comparison of fitted and calculated magnetic functions in Fig. 27b. AC magnetic measurements confirmed at least two peaks visible at frequency dependence of the out-of-phase magnetic susceptibility, indicating that slow magnetic relaxation has a multi-channel

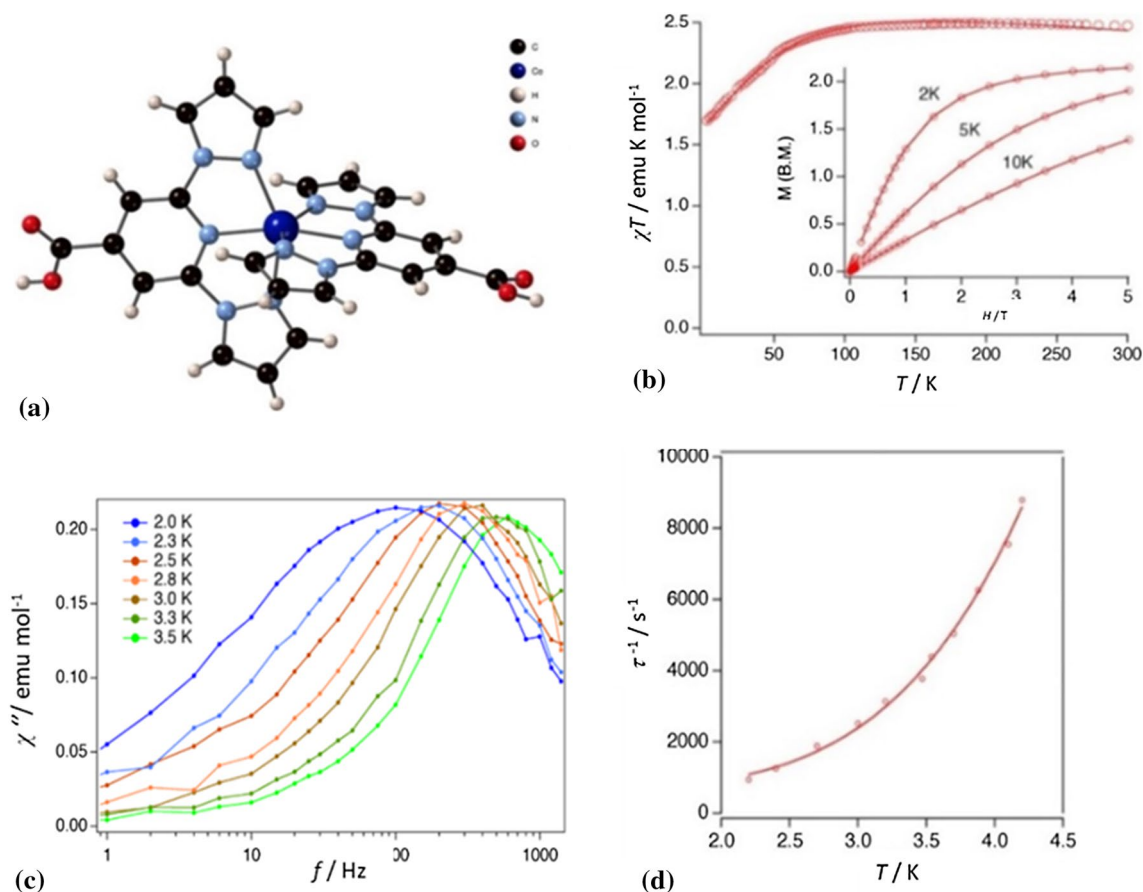
nature (Fig. 27c). Therefore, the dynamic magnetic properties were analysed by the extended three-set Debye model. By help of extracted isothermal susceptibilities was possible to determine the mole fractions of corresponding relaxation channels  $x(\text{LF})=0.19$ ,  $x(\text{IF})=0.45$ , and  $x(\text{HF})=0.37$ . The Arrhenius-like plot  $\ln\tau$  vs.  $T^{-1}$  visualizes the thermal development of the individual relaxation times (Fig. 27d). Interestingly, the low frequency relaxation time at  $T=1.9$  K is by order of magnitude higher for **45** relative to **46** ( $\tau_{\text{LF}}=282$  vs.  $29$  ms for **45** and **46**, respectively) at a similar external field. This is an indication that even small modifications of the SIMs are important for the slow magnetic relaxation.

García López et al. [76] conducted research dealing with field-induced SRM in a mononuclear Co(II) complex with 2,6-bis(pyrazol-1-yl)pyridine ligands functionalized with a carboxylic group (**L29**). The bis-chelated Co(II) complex **47** (Fig. 28a) of the tridentate ligand **L29** of formula  $[\text{Co}(\mathbf{L29})_2](\text{ClO}_4)_2 \cdot 2\text{Me}_2\text{CO}$  was prepared by mixing acetone solutions of **L29** (which was previously prepared according to literature method [77]) and corresponding Co(II) salt. The red–orange prismatic crystals of compound **47** suitable for X-ray diffraction measurements were obtained by slow diffusion of diethyl ether into this solution. The compound **47** crystallizes in the monoclinic space group  $P2_1/c$ . The central Co(II) ion is coordinated by six N atoms from the two tridentate ligand **L29**. The distorted octahedron consists of two shorter Co–N axial bonds formed with the central pyridine rings (2.07 and 2.08 Å) and four longer equatorial Co–N bonds of pyrazole moieties (from 2.11 to 2.15 Å). These distances are typical for hexacoordinated Co(II) HS complexes.

**Fig. 27** Molecular structure of **45** with unsymmetrical hydrogen bonds between anionic part of carboxylic acids and a complex cationic unit (a). DC magnetic data for **45**. The solid lines denote fitting by the ZFS model. The dashed lines resemble *ab initio* calculation (b) frequency-dependent in-phase and out-of-phase  $\chi''$  components of AC susceptibility for compound **45** recorded at an applied static magnetic field 2500 Oe (c). Arrhenius-like plot for **45**. The dashed lines are a guide to the eye (d). Taken with permission from Ref. [74]







**Fig. 28** Molecular structure of cationic complex in **47**. Colour code: Co—dark blue, O—red, N—light blue, C—black (**a**). Temperature dependence of the product of the magnetic susceptibility times the temperature at 0.1 T. Inset: isothermal magnetizations measured at  $T=2, 5,$  and  $10$  K. Empty circles: experimental data. Full lines: simu-

lated curves using best simultaneous fit (**b**). Frequency dependence of out-of-phase molar susceptibilities for **47** at 3000 Oe (**c**). Thermal dependence of the relaxation time and best fit (**d**). Taken with permission from Ref. [76] (colour figure online)

The pyrazol rings of two neighbouring complex cations  $[\text{Co}(\text{L29})_2]^{2+}$  create face-to-face  $\pi$ - $\pi$  and edge-to-face  $\text{CH}-\pi$  interactions which are responsible for the formation of 1D supramolecular chain along the  $a$  axis. Moreover, those chains are linked through C-O, CH-O, and CH- $\pi$  intermolecular contacts into the second direction leading to the formation of layers of complexes in the  $a$ - $c$  plane alternating with a layer of perchlorate counter ions and acetone solvent molecules. This kind of weak intermolecular interactions is responsible for the loss of solvent molecules after extracting the crystals from the mother liquor. The thermal dependence of the product of the molar magnetic susceptibility times the temperature ( $\chi T$ ) shows a value of  $2.47 \text{ cm}^3 \text{ K mol}^{-1}$  at 300 K, which is in accordance with expected values for HS Co(II) with some orbital momentum contribution. While cooling, this value decreases continuously with a sudden drop below 100 K due to single-ion anisotropy and reaches value of  $1.70 \text{ cm}^3 \text{ K mol}^{-1}$  at 2 K. The magnetization at 5 T and 2 K saturates to value of  $2.14 \mu_{\text{B}}$  and it is significantly

lower than the expected saturation for a system with  $S=3/2$  and  $g>2$  (Fig. 28b). Fitting of DC magnetic data results in the values of  $D=51.6 \text{ cm}^{-1}$ ,  $g=2.41$ , and  $E/D=0.28$ , which are similar to values found in related compounds [78, 79]. The AC measurements revealed no signal in out-of-phase magnetic susceptibility in the absence of DC field, which is common behaviour in mononuclear Co(II) SMMs and it is usually attributed to QTM, dipolar interactions or hyperfine interactions [80]. The AC data under small applied static field show single relaxation channel (Fig. 28c) and analysed with one-set Debye model. The highest temperature relaxation times were fitted to the Arrhenius expression for a thermally activated Orbach process (Fig. 28d) leading to parameters  $U_{\text{eff}}=16 \text{ K}$  and  $\tau_0=2.7 \times 10^{-6} \text{ s}$ . This effective barrier is lower than experimental energy gap between both Kramer doublets, which indicates the contribution of other relaxation mechanisms.

## Conclusions

Although the field of Ln-SMMs has been catching attention in recent years heavily, from this review, it is apparent that there is still a lot to explore in the topic of Co(II) SIMs. Numerous recent works have studied the correlation between magnetic properties and structural parameters. By understanding this correlation, the controlled tuning of the magnetic anisotropy simply by choice of the ligand could be available.

Nevertheless, the situation in Co(II) complexes is more complicated than in other transition metals, such as Ni(II), since the structural distortions from the ideal shapes of coordination polyhedra are more complex. As Titiš et al. [81] reported in 2013, “*The only steps forward are representing by synthesising a more numerous set of coordination compounds and subject them to a magnetochemical investigation by contemporary hardware and software.*” [81]. Nowadays, in this review, we sum up some of the most significant studies, which have been committed to the design and synthesis of novel Co(II) SIMs via several synthetic strategies and investigations of magnetic properties.

In the case of tetracoordinate Co(II) complexes, the highest value of parameters  $D$ , as well as  $U_{\text{eff}}$ , was acquired by compound **2** [26], where Albold et al. used the strategy of creating a strongly coupled multispin system to suppress the existence of undesirable relaxation parameters that are not influenced by  $U_{\text{eff}}$ , such as QTM and Raman process. They took as inspiration the multispin metal radical complex **1**. It can be said that their approach was successful by the means that also the value of relaxation time at low temperatures and the field of 1500 Oe reached 32,000 s, which is undoubtedly the highest reported one in this review. Furthermore, so far, these values are the highest reported overall.

The largest  $U_{\text{eff}}$  in the case of penta- and hexacoordinate compounds was reported in the hexacoordinate compound **46** (44 K) [75]. In contrast, the highest experimental as well as calculated parameter  $D$  was reported in the pentacoordinate Co(II) complex **24** ( $D > 100 \text{ cm}^{-1}$ ) [58]. Although it is generally established that since the positive value of the  $D$  parameter has a ground state of  $M = 0$ , and therefore, there should be no  $U_{\text{eff}}$  found, the SMM behaviour can still be observed in those systems. In addition, indeed, complex **24** was proven to be field-induced SMM with the characteristics of SRM typical for pentacoordinate Co(II) complexes.

Although there is still not a complete understanding of tuning the SRM in Co(II) complexes, the most recent results suggest that the approach of the incorporation the strong exchange couplings in the transition–metal–radical systems could be particularly fruitful in terms of increasing the magnetic anisotropy as well as the values of effective barrier  $U_{\text{eff}}$  and relaxation time  $\tau$ .

**Acknowledgements** This research has been financially supported by the Ministry of Education, Youth and Sports of the Czech Republic under the project CEITEC 2020 (LQ1601) and by the MSM under the project LTAUSA19060 in the INTER-EXCELLENCE programme. We acknowledge financial support from the Grant Agency of the Czech Republic (GAČR 22-23760S). In addition, funding from the ERC under the European Union's Horizon 2020 program (GA No. 714850) is acknowledged. Slovak grant agencies (APVV-18-0197, APVV-18-0016, APVV-19-0087, VEGA 1/0029/22, KEGA 018-STU-4) are acknowledged for the financial support. This article was written thanks to the generous support under the Operational Program Integrated Infrastructure for the project: "Strategic research in the field of SMART monitoring, treatment and preventive protection against coronavirus (SARS-CoV-2)", Project no. 313011ASS8, co-financed by the European Regional Development Fund. I.Š. acknowledges the financial support from institutional sources of the Department of Inorganic Chemistry, Palacký University Olomouc, Czech Republic.

## References

- Sessoli R, Gatteschi D, Caneschi A, Novak MA (1993) *Nature* 365:141
- Gatteschi D, Sessoli R, Villain J (2006) *Molecular nanomagnets*. Oxford University Press, Oxford
- Goodwin CAP, Ortu F, Reta D, Chilton NF, Mills DP (2017) *Nature* 548:439
- Guo FS, Day BM, Chen YC, Tong ML, Mansikkamäki A, Layfield RA (2018) *Science* 362:1400
- Guo FS, Day BM, Chen YC, Tong ML, Mansikkamäki A, Layfield RA (2017) *Angew Chem Int Ed* 56:11445
- Slageren J. Introduction to Molecular Magnetism. <http://obelix.physik.uni-bielefeld.de/~schnack/molmag/material/123.pdf>
- Magnani N, Caciuffo R (2018) *Inorganics* 6:26
- Zabala-Lekuona A, Seco JM, Colacio E (2021) *Coord Chem Rev* 441:213984
- Liu JL, Chen YC, Tong ML (2018) *Chem Soc Rev* 47:2431
- Ruiz-Molina D, Christou G, Hendrickson DN (2000) *Mol Cryst Liq Cryst Sci Technol Sect A* 343:17
- Layfield RA, Murugesu M (2015) *Lanthanides and actinides in molecular magnetism*. Wiley, New York
- Tang J, Zhang P (2015) *Lanthanide single molecule magnets*. Springer, New York
- Juráková J, Dubnická Midlřková J, Hrubý J, Kliuikov A, Santana VT, Pavlik J, Moncol J, Čiřmár E, Orlita M, Mohelský I, Neugebauer P, Gentili D, Cavallini M, Šalitroš I (2022) *Inorg Chem Front* 9:1179
- Christou G, Gatteschi D, Hendrickson D, Sessoli R (2000) *MRS Bull* 25:66
- Murrie M (2010) *Chem Soc Rev* 39:1986
- Herchel R. Molekulární magnety “molecule-based magnets.” <http://nanosystemy.upol.cz/upload/1/herchel.pdf>
- Sessoli R, Gatteschi D (2003) *Angew Chem Int Ed* 42:268
- Hubner W, Bennemann KH (1996) *Phys Rev B* 53:3422
- Ding M, Hickey AK, Pink M, Telser J, Tierney DL, Amoza M, Rouzières M, Ozumerzifon TJ, Hoffert WA, Shores MP, Ruiz E, Clérac R, Smith JM (2019) *Chem Eur J* 25:10625
- Shrivastava KN (1983) *Phys Status Solidi B* 117:437
- Zahradníková E, Herchel R, Šalitroš I, Čiřarová I, Drahoř B (2020) *Dalton Trans* 49:9057
- Rechkemmer Y, Breitgoff F, van der Meer M, Atanasov M, Haki M, Orlita M, Neugebauer P, Neese F, Sarkar B, van Slageren J (2016) *Nat Commun* 7:10467
- Fataftah MS, Zdrozny JM, Rogers DM, Freedman DE (2014) *Inorg Chem* 53:10716

24. Zadrozny JM, Telser J, Long JR (2013) *Polyhedron* 64:209
25. Saber MR, Dunbar KR (2014) *Chem Commun* 50:12266
26. Albold U, Bamberger H, Hallmen PP, van Slageren J, Sarkar B (2019) *Angew Chem Int Ed* 58:9802
27. Yao XN, Du JZ, Zhang YQ, Leng XB, Yang MW, Jiang SD, Wang ZX, Ouyang ZW, Deng L, Bing-Wu W, Song G (2017) *J Am Chem Soc* 139:373
28. Ferguson A, Parkin A, Sanchez-Benitez J, Kamenev K, Wernsdorfer W, Murrie M (2007) *Chem Commun* 3473
29. Dayu Wu, Guo D, Song Y, Huang W, Duan C, Meng Q, Sato O (2009) *Inorg Chem* 48:854
30. Bunting PC, Atanasov M, Damgaard-Møller E, Perfetti M, Crassee I, Orlita M, Overgaard J, van Slageren J, Neese F, Long JR (2018) *Science* 362:6421
31. Mitsuhashi R, Hosoya S, Suzuki T, Sunatsuki Y, Sakiyama H, Masahiro M (2019) *Dalton Trans* 48:395
32. Peng G, Chen Y, Li B, Zhang YQ, Ren XM (2020) *Dalton Trans* 49:5798
33. Ishizaki T, Fukuda T, Akaki M, Fuyuhiko A, Hagiwara M, Ishikawa N (2019) *Inorg Chem* 58:5211
34. Cui HH, Lu F, Chen XT, Zhang YQ, Tong W, Xue ZL (2019) *Inorg Chem* 58:12555
35. Carl E, Demeshko S, Meyer F, Stalke D (2015) *Chem Eur J* 21:10109
36. Yang RC, Wang DR, Liu JL, Wang YF, Lin WQ, Leng JD, Zhou AJ (2019) *Chem Asian J* 14:1467
37. Mondal AK, Sundararajan M, Konar S (2018) *Dalton Trans* 47:3745
38. Grutters MMP, Müller C, Vogt D (2006) *J Am Chem Soc* 128:7414
39. Fondo M, Corredoira-Vázquez J, García-Deibe AM, Sanmartín-Matalobos J, Herrera JM, Colacio E (2018) *Front Chem* 6:420
40. Chen YC, Huang XS, Liu JL, Tong ML (2018) *Inorg Chem* 57:11782
41. Fawcett J, Platt AWG, Vickers S, Ward MD (2004) *Polyhedron* 23:2561
42. Vaidya S, Upadhyay A, Singh SK, Gupta T, Tewary S, Langley SK, Walsh JPS, Murray KS, Rajaraman G, Shanmugam M (2015) *Chem Commun* 51:3739
43. Shao D, Zhang SL, Shi L, Zhang YQ (2016) *Inorg Chem* 55:10859
44. Mondal AK, Goswami T, Misra A, Konar S (2017) *Inorg Chem* 56:6870
45. Hrubý J, Dvořák D, Squillantini L, Mannini M, van Slageren J, Herchel R, Nemeč I, Neugebauer P (2020) *Dalton Trans* 49:11697
46. Park TJ, Huh S, Kim Y, Jun MJ (1999) *Acta Cryst C* 55:848
47. Corain B, Longato B, Favero G, Ajò D, Pilloni G, Russo U, Kreissl FR (1989) *Inorg Chim Acta* 157:259
48. Vaidya S, Tewary S, Singh SK, Langley SK, Murray KS, Lan Y, Wernsdorfer W, Rajaraman G, Shanmugam M (2016) *Inorg Chem* 55:9564
49. Zadrozny JM, Long JR (2011) *J Am Chem Soc* 133:20732
50. Jurca T, Farghal A, Lin PH, Korobkov I, Murugesu M, Richeson DS (2011) *J Am Chem Soc* 133:15814
51. Chirico RD, Carlin RL (1980) *Inorg Chem* 19:3031
52. Hung SW, Yang FA, Chen JH, Wang SS, Tung JY (2008) *Inorg Chem* 47:7202
53. Mabbs FE, Machin DJ (2008) *Magnetism and Transition Metal Complexes*. Dover Publications, Mineola
54. Rajnák C, Varga F, Titiš J, Moncol J, Boča R (2017) *Eur J Inorg Chem* 2017:1915
55. Cariou R, Chirinos JJ, Gibson VC, Jacobsen G, Tomov AK, Britovsek GJP, White AJP (2010) *Dalton Trans* 39:9039
56. Gong D, Jia X, Wang B, Zhang X, Jiang L (2012) *J Organomet Chem* 702:10
57. Addison AW, Nageswara RT, Reedijk J, van Rijn J, Verschoor CV (1984) *J Chem Soc Dalton Trans* 1349
58. Rajnák C, Titiš J, Miklovič J, Kostakis GE, Fuhr O, Ruben M, Boča R (2017) *Polyhedron* 126:174
59. Rajnák C, Titiš J, Šalitraš I, Boča R, Fuhr O, Ruben M (2013) *Polyhedron* 65:122
60. Rajnák C, Titiš J, Fuhr O, Ruben M, Boča R (2014) *Inorg Chem* 53:8200
61. Habib F, Luca OR, Vieru V, Shiddiq M, Korobkov I, Gorelsky SI, Takase MK, Chibotaru LF, Hill S, Crabtree RH, Murugesu M (2013) *Angew Chem Int Ed* 52:11290
62. Lin HP, Korobkov I, Burchell TJ, Murugesu M (2012) *Inorg Chim Acta* 380:378
63. Brachňáková B, Matejová S, Moncol J, Herchel R, Pavlik J, Moreno-Pineda E, Ruben M, Šalitraš I (2020) *Dalton Trans* 49:1249
64. Guionneau P, Marchivie M, Bravic G, Létard JF, Chasseau D (2004) *Top Curr Chem* 234:97
65. Halcrow MA (2009) *Coord Chem Rev* 253:2493
66. Nemeč I, Marx R, Herchel R, Neugebauer P, van Slageren J, Trávníček Z (2015) *Dalton Trans* 44:15014
67. Brewer B, Brooks N, Abdul-Halim S, Sykes A (2003) *J Chem Crystallogr* 33:651
68. Woods TJ, Ballesteros-Rivas MF, Gómez-Coca S, Ruiz E, Dunbar KR (2016) *J Am Chem Soc* 138:16407
69. Tyeklar Z, Jacobson RR, Wei N, Murthy NN, Zubieta J, Karlin KD (1993) *J Am Chem Soc* 115:2677
70. Heintz RA, Smith JA, Szalay PS, Weisgerber A, Dunbar KR (2002) *Inorg Synth* 33:75
71. Rajnák C, Titiš J, Moncol J, Renz F, Boča R (2017) *Eur J Inorg Chem* 2017:1520
72. Wang JG, Qin JH, Zhang GY (2009) *Acta Cryst E* 65:m247
73. Shi L, Shen FX, Shao D, Zhang YQ, Wang XY (2019) *CrystEng-Comm* 21:3176
74. Rajnák C, Titiš J, Moncol J, Boča R (2020) *Dalton Trans* 49:4206
75. Valigura D, Rajnák C, Moncol J, Titiš J, Boča R (2017) *Dalton Trans* 46:10950
76. García-López V, Orts-Mula FJ, Palacios-Corella M, Clemente-Juan JM, Clemente-León M, Coronado E (2018) *Polyhedron* 150:54
77. Vermonden T, Branowska D, Marcellis ATM, Sudhölter EJR (2003) *Tetrahedron* 59:5039
78. Gómez-Coca S, Urtizberea A, Cremades E, Alonso PJ, Camón A, Ruiz E, Luis F (2014) *Nat Commun* 5:4300
79. Sertphon D, Murray KS, Phonsri W, Jover J, Ruiz E, Telfer SG, Alkas A, Harding P, Harding DJ (2018) *Dalton Trans* 47:859
80. Zhang YZ, Gómez-Coca S, Brown AJ, Saber MR, Zhang X, Dunbar KR (2016) *Chem Sci* 7:6519
81. Titiš J, Miklovič J, Boča R (2013) *Inorg Chem Comm* 35:72

**Publisher's Note** Springer Nature remains neutral with regard to jurisdictional claims in published maps and institutional affiliations.

## Authors and Affiliations

Jana Juráková<sup>1</sup>  · Ivan Šalitrš<sup>1,2,3</sup>

<sup>1</sup> Central European Institute of Technology, Brno University of Technology, Purkyňova 123, 61200 Brno, Czech Republic

<sup>2</sup> Department of Inorganic Chemistry, Faculty of Chemical and Food Technology, Slovak University of Technology in Bratislava, Bratislava 81237, Slovakia

<sup>3</sup> Department of Inorganic Chemistry, Faculty of Science, Palacký University, 17. listopadu 12, 771 46, Olomouc, Czech Republic